

UNIVERSITY OF SÃO PAULO – USP
SÃO CARLOS SCHOOL OF ENGINEERING – EESC
HEAT TRANSFER RESEARCH GROUP

Gustavo Matana Aguiar

**An experimental study on flow boiling in single
microchannels subjected to localized cyclical heating loads**

São Carlos – SP

2017

Gustavo Matana Aguiar

**Estudo Experimental da Ebulição Convectiva no Interior de
Microcanais Únicos Sujeitos a Aquecimento Localizado com
Variações Cíclicas do Fluxo de Calor**

Dissertação apresentada ao Programa de Pós-Graduação em Engenharia Mecânica da Escola de Engenharia de São Carlos, Universidade de São Paulo como requisito necessário para a obtenção do título de Mestre em Engenharia Mecânica

Área de Concentração: Termociências e Mecânica dos Fluidos

Orientador: Professor Gherhardt Ribatski

**ESTE EXEMPLAR TRATA-SE DA VERSÃO
CORRIGIDA.
A VERSÃO ORIGINAL ENCONTRA-SE
DISPONÍVEL JUNTO AO
DEPARTAMENTO DE ENGENHARIA
MECANICA DA EESC-USP.**

São Carlos – SP

2017

Class.	TESE
Cutt.	10.345
Tombo	T169/19
Sysno	2946944

31 Lev 213192

11.06 19

AUTORIZO A REPRODUÇÃO E DIVULGAÇÃO TOTAL OU PARCIAL DESTA TRABALHO, POR QUALQUER MEIO CONVENCIONAL OU ELETRÔNICO, PARA FINS DE ESTUDO E PESQUISA, DESDE QUE CITADA A FONTE.

A282

Aguiar, Gustavo Matana

An experimental study on flow boiling in single microchannels subjected to localized cyclical heating loads / Gustavo Matana Aguiar; orientador Gherhardt Ribatski. São Carlos, 2017.

Dissertação (Mestrado) - Programa de Pós-Graduação em Engenharia Mecânica e Área de Concentração em Térmica e Fluidos -- Escola de Engenharia de São Carlos da Universidade de São Paulo, 2017.

1. Flow Boiling. 2. Microchannels. 3. Transient Heating. 4. Heat Transfer Coefficient. I. Título.

FOLHA DE JULGAMENTO

Candidato: Engenheiro **GUSTAVO MATANA AGUIAR**.

Título da dissertação: "Estudo experimental da ebulição convectiva no interior de microcanais únicos sujeitos a aquecimento localizado com variações cíclicas do fluxo de calor".

Data da defesa: 15/12/2017.

Comissão Julgadora:

Resultado:

Prof. Associado **Gherhardt Ribatski**
(Orientador)
(Escola de Engenharia de São Carlos/EESC)

APROVADO

Profa. Dra. **Marcia Barbosa Henriques Mantelli**
(Universidade Federal de Santa Carlos/UFSC)

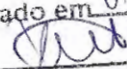
aprovado

Prof. Dr. **Matteo Bucci**
(Instituto de Tecnologia de Massachusetts/MIT-USA)

APROVADO

Coordenador do Programa de Pós-Graduação em Engenharia Mecânica:
Prof. Associado **Gherhardt Ribatski**

Presidente da Comissão de Pós-Graduação:
Prof. Associado **Luís Fernando Costa Alberto**

EESC/USP
Serviço de Pós Graduação
Protocolado em 07/06/2019


ACKNOWLEDGEMENTS

I would like to acknowledge the financial support provided by CAPES (Coordination for the Improvement of Higher Education Personnel) and the infrastructure and personnel provided by the University of Sao Paulo. Also, I would like to express my gratitude for being part of the Heat Transfer Research Group at EESC/USP over these two years. I thank my lab fellows Daiane, Daniel, Douglas, Erivelto, Francisco, Hugo, Jaqueline, Karime and Tiago for the fruitful discussions and for all the fun we have had in this period. The technical support given to this investigation by Mr. Jose Roberto Bogni for the construction of the experimental bench and by Eng. Jorge Nicolau for the instrumentation and automation of the experimental bench is also appreciated and deeply recognized. Foremost, I shall thank my advisor Prof. Gherhardt Ribatski for encouraging me to pursue graduate studies when I was finishing my bachelor degree as well as for his guidance and the opportunities provided to me during this period.

Behind everything, throughout the entire journey, I have benefitted immensely from the support of friends and family. My parents Paulo Hugo and Maria José provided me to all sorts of opportunities and experiences as I grew up, and they were incredibly encouraging of all I wanted to do. I can just as easily summarize their meaning to me in a single sentence: a kid couldn't ask for a better Mom and Dad. I also want to express my profound gratitude for my beloved girlfriend Ana Claudia for the care and support during this period. Final thanks go to all my friends, not previously mentioned, who supported me or influenced me along the way.

ABSTRACT

Aguiar, G. M. (2017). **An experimental study on flow boiling in single microchannels subjected to localized cyclical heating loads.** Dissertation (Master) – Department of Mechanical Engineering, São Carlos School of Engineering, University of São Paulo. 155p.

Flow boiling in microchannels is a promising technique for the thermal management of devices that dissipate extremely high heat flux rates. As additional constraints, these devices operate under temporal variations of the heat load and the presence of hotspots (region of higher heat dissipation), e.g. CPUs and high-concentration photovoltaics (HCPV) systems. Up to present date, a limited but increasing number of studies have explored the outcomes of hotspots presence in the heat removal efficiency during flow boiling in micro-scale channels. The number of studies covering transient heating conditions during flow boiling in microchannels is even more scarce. Within this context, this study presents an experimental investigation of the transient behavior of the local wall superheat temperature and heat transfer coefficient in a hotspot region undergoing through cyclical heating pulses during flow boiling of R134a at a saturation temperature of 31°C in 0.5 and 1.1 mm diameter circular channels made from stainless steel. A parametric analysis of the effects of mass velocity, local vapor quality, average heat flux and the heating pulses waveform, amplitude, frequency on the heat transfer behavior was performed. From this analysis, it was concluded that the wall superheat temperature fluctuations are affected by the superposition of thermal inertia effects, related to the heat conduction at the tube wall, and flow boiling effects. The level of wall superheat temperature fluctuations increased with decreasing heating pulses frequency and the time-averaged heat flux and increasing mass velocity, vapor quality and heating pulses amplitude. The results indicated that the wall temperature oscillations were diminished when the nucleate boiling effects became more pronounced. Eight well-known methods from literature for predicting the flow boiling heat transfer coefficient in small diameter channels, developed for steady heating, were extrapolated to the transient heating conditions of this study and their accuracy were verified. The methods of Kanizawa et al. (2016) and Kim and Mudawar (2013) lead to the most satisfactory predictions of the average heat transfer coefficient and the amplitude of the wall superheat temperature

fluctuations. At the end, a methodology for predicting the transient behavior of wall superheat temperature under cyclical heat loads is presented. This methodology is shown to reproduce the main trends of the experimental data.

Keywords: *Flow Boiling, Microchannels, Transient Heating, Hotspot, Heat Transfer Coefficient*

RESUMO

Aguiar, G. M. (2017). **Estudo Experimental da Ebulição Convectiva no Interior de Microcanais Únicos Sujeitos a Aquecimento Localizado com Variações Cíclicas do Fluxo de Calor**. Dissertação (Mestrado) – Departamento de Engenharia Mecânica, Escola de Engenharia de São Carlos, Universidade de São Paulo. 155p.

A ebulição convectiva no interior de microcanais é um método promissor para o gerenciamento térmico de dispositivos que dissipam elevados fluxos de calor. Como requisitos adicionais, estes dispositivos comumente operam sob variações temporais do fluxo de calor e na presença de *hotspots* (regiões de elevada dissipação de calor), e.g. CPUs e painéis fotovoltaicos de alta concentração. Até o presente momento, um número crescente de estudos, porém limitado, explorou as consequências da presença de *hotspots* na eficiência da remoção de calor durante a ebulição convectiva no interior de microcanais. O número de estudos abrangendo o aquecimento transiente durante a ebulição convectiva no interior de microcanais é ainda mais escasso. Dentro deste contexto, o presente estudo envolve a investigação experimental do comportamento transiente do grau de superaquecimento da parede e do coeficiente de transferência de calor em um *hotspot* sujeito a pulsos de calor durante a ebulição convectiva. Ensaios foram realizados para o fluido R134a a temperatura de saturação de 31°C no interior de tubos circulares de aço inoxidável com diâmetros de 0.5 e 1.1 mm. Foi realizada uma análise paramétrica sobre os efeitos na transferência de calor da velocidade mássica, título de vapor local e o formato da onda de pulsos de calor e sua respectiva amplitude, frequência e o fluxo de calor médio correspondente. A análise paramétrica revelou que as flutuações do grau de superaquecimento da parede são resultado da superposição dos efeitos de inércia térmica, relacionados a condução de calor na parede do tubo, e da ebulição convectiva. O nível das flutuações do grau de superaquecimento da parede se elevou com o aumento da velocidade mássica, título de vapor e amplitude dos pulsos de calor, e com a redução da frequência dos pulsos de calor e do fluxo de calor médio. Os resultados indicaram o decréscimo das oscilações de temperatura com a intensificação dos efeitos de ebulição nucleada. Oito métodos para a previsão do coeficiente de transferência de calor durante a ebulição convectiva em canais de diâmetro reduzido,

desenvolvidos baseado em banco de dados obtido em condições de aquecimento uniforme e permanente, foram extrapolados para resultados transientes compreendendo pulsos de calor deste trabalho. Os métodos de Kanizawa et al. (2016) e Kim e Mudawar (2013) proporcionaram previsões satisfatórias do coeficiente de transferência de calor médio e da amplitude das flutuações do superaquecimento da parede. Ao final deste estudo, uma metodologia para prever o comportamento transiente do superaquecimento da parede durante pulsos de calor cíclicos é apresentada. A eficácia desta metodologia em reproduzir as principais tendências observadas nos dados experimentais é demonstrada.

Palavras chave: *Ebulição Convectiva, Microcanais, Aquecimento Transiente, Hotspot, Coeficiente de Transferência de Calor*

LIST OF FIGURES

Figure 1.1 – Metallic porous media heat sink (50 mm x 50 mm x 25 mm)	32
Figure 1.2 – Heat transfer coefficient distribution obtained from an array of four impingement jets to cool densely packed photovoltaic cells.....	33
Figure 1.3 – Commercial heat sink for CPUs based on microchannels and using water as the working fluid. Model Nepton 140XL from Cooler Master	34
Figure 1.4 – Power map of a 45 nm Intel Core 2 Duo processor	36
Figure 1.5 – Hotspot development in the solar cell inherent to concentrating systems..	37
Figure 1.6 – Typical irradiance distribution on a solar cell	37
Figure 2.1 – Transitional diameter between macro and micro scale with saturation temperature for R134a according to different criteria	47
Figure 2.2 – Flow pattern images for R245fa flowing through a 2.32 mm internal diameter channel.	48
Figure 2.3 – Sequence of flow patterns observed in microchannels for nucleate boiling dominant heat transfer.....	51
Figure 2.4 – Sequence of flow patterns observed in microchannels for convective boiling dominant heat transfer.....	52
Figure 3.1 – Schematic illustration of a microchannels-based heat sink with oblique fins	57
Figure 3.2 – Heat sink with obliquely finned microchannel of variable pitch evaluated by Lee, Lee and Chou (2013)	58
Figure 3.3 – Hotspot-targeted embedded microchannel structure	59
Figure 3.4 - 5 x 5 array of heater elements and a schematic diagram of the microchannel heat sink used by Ritchey et al. (2014).....	60
Figure 3.5 – Illustration of the displacement of the boiling front as the transverse hotspot position moves from the middle (b) to the the channels inlet (a).	61
Figure 3.6 – Illustration of the anticipation of boiling front as the hotspot is positioned at the channels inlet.....	62
Figure 3.7 – Illustration of the differential pressure signal transition from high-amplitude low frequency to low amplitude high frequency fluctuations for increasing heat flux at the downstream hotspot region	64
Figure 3.8 – Heat sink configurations evaluated by Cho et al. (2010) under non-uniform heating conditions	64

Figure 3.9 – Wall temperature distribution for the heat sink with straight microchannels and trapezoidal headers according to different hotspot positions	65
Figure 3.10 – Wall temperature distribution for the heat sink with diverging microchannels and trapezoidal headers according to different hotspot positions.....	65
Figure 3.11 – Temporal variations of the wall temperature for a fixed position at the heat sink centerline (a) and temperature profile along the heat sink centerline (b) during a cold startup of a silicon microchannels-based heat sink composed of 67 channels, $D_H = 0.1$ mm, R236fa, $G = 1500$ kg/m ² s, $\Delta T_{sub} = 5.5^\circ\text{C}$, $T_{sat} = 31.5^\circ\text{C}$ and $q''_{max} = 300$ kW/m ² .	67
Figure 3.12 – Flow boiling map of water under pulse heating in a microheater within a microchannel.....	69
Figure 4.1 – Multipurpose experimental test bench located at Heat Transfer Research Group – EESC/USP (Nov/2016)	71
Figure 4.2 – Schematic diagram of the refrigerant circuit	72
Figure 4.3 – Pressure vs. enthalpy diagram of the refrigerant thermodynamic states along the main circuit (R134a)	73
Figure 4.4 – Schematic diagram of the auxiliary circuit.....	74
Figure 4.5 – Schematic diagram of the pre-heater and test section (Dimensions in mm)	75
Figure 4.6 – Schematic diagram of the test section (Dimensions in mm)	75
Figure 4.7 – Simulated geometry and boundary conditions adopted for the evaluation of fin effect in the test section due to copper electrodes presence (Dimensions in mm)....	76
Figure 4.8 – Illustration of the fin effect of the soldered copper electrodes on the test section temperature field.....	77
Figure 4.9 – External wall temperature profile along the test section	78
Figure 4.10 – Test section assembly without thermal insulation.....	78
Figure 4.11 – Schematic diagram of data acquisition system components interconnections	81
Figure 4.12 – Front panel of LabVIEW interface.....	82
Figure 5.1 – Relative heat losses to environment vs. average Nusselt number for the 0.5 mm internal diameter tube	85
Figure 5.2 – Relative heat losses to environment vs. average heat transfer coefficient for the 1.1 mm internal diameter tube	85
Figure 5.3 –Nusselt number profile along the tube axial direction during flow boiling for $D = 1.1$ mm, $T_{sat} = 31^\circ\text{C}$, $G = 600$ kg/m ² s, $\Delta T_{sub} = 8^\circ\text{C}$, $q''_{pre} = 6$ kW/m ² , $q''_{bg} = 40$ kW/m ² and $q''_{spot} = 80$ kW/m ² (Heat losses included).....	86

Figure 5.4 – Instantaneous heat flux profile along the tube axial direction during flow boiling tests for $D = 1.1$ mm, $T_{sat} = 31^\circ\text{C}$, $G = 600$ kg/m ² s, $\Delta T_{sub} = 8^\circ\text{C}$, $q''_{pre} = 6$ kW/m ² , $q''_{bg} = 40$ kW/m ² and $q''_{hpot} = 80$ kW/m ²	89
Figure 5.5 – 1-D Fluid discrete element	90
Figure 5.6 – Algorithm for the 1-D Discrete element procedure.....	94
Figure 5.7 – Comparison between predictions for the single-phase Nusselt according to seven methods from literature and the experimental results number of $D = 0.5$ mm test section.	96
Figure 5.8 – Comparison between predictions for the single-phase Nusselt according to seven methods from literature and the experimental results number of $D = 1.1$ mm test section.	97
Figure 5.9 – Comparison of flow boiling heat transfer coefficient for steady-state conditions for $D = 0.5$ mm, $T_{sat} = 31^\circ\text{C}$, $G = 600$ kg/m ² s and $q''_{hpot} = 40$ kW/m ²	97
Figure 5.10 – Comparison of flow boiling heat transfer coefficient for steady-state conditions for $D = 1.1$ mm, $T_{sat} = 31^\circ\text{C}$, $G = 400$ kg/m ² s and $q''_{hpot} = 25$ kW/m ²	98
Figure 5.11– Assessment of the pressure drop model accuracy for the $D = 0.5$ mm test section	99
Figure 5.12 – Assessment of the pressure drop model accuracy for the $D = 1.1$ mm test section	99
Figure 5.13 – Distribution of fluid temperature oscillations during transient flow boiling tests	101
Figure 5.14 – Frequency distribution of estimated time constant based on experimental data for the two tested tube diameters.....	102
Figure 6.1 –Transient behavior of the wall superheat temperature (a) and heat transfer coefficient (b) for square heating pulses. R134a, $D = 1.1$ mm, $T_{sat} = 31^\circ\text{C}$, $G = 400$ kg/m ² s, $\bar{x}_{hpot} = 8\%$, $\bar{q}''_{hpot} = 80$ kW/m ² , $\Delta q''_{hpot} = 40$ kW/m ² and $f = 0.5$ Hz	107
Figure 6.2 –Transient behavior of the (a) wall superheat temperature and (b) HTC under sinusoidal heating pulses. R134a, $D = 1.1$ mm, $T_{sat} = 31^\circ\text{C}$, $G = 400$ kg/m ² s, $\bar{x}_{hpot} = 60\%$, $\bar{q}''_{hpot} = 120$ kW/m ² , $\Delta q''_{hpot} = 40$ kW/m ² and $f = 1$ Hz	108
Figure 6.3 – Variation of the phase angle according to the sinusoidal heating pulses frequency. R134a, $D = 1.1$ mm, $T_{sat} = 31^\circ\text{C}$, $G = 400$ kg/m ² s, $\bar{x}_{hpot} = 60\%$, $\bar{q}''_{hpot} = 120$ kW/m ² , $\Delta q''_{hpot} = 40$ kW/m ² and $f = 1$ Hz.....	108
Figure 6.4 – Fourier transform of the zero-mean heat flux, ΔT_w and HTC signals for R134a, $D = 1.1$ mm, $T_{sat} = 31^\circ\text{C}$, $G = 400$ kg/m ² s, $\bar{x}_{hpot} = 60\%$, $\bar{q}''_{hpot} = 120$ kW/m ² , $\Delta q''_{hpot} = 40$ kW/m ² and $f = 1$ Hz	108

Figure 6.5 – Transient behavior of the (a) wall superheat temperature and (b) HTC under sinusoidal heat pulses. R134a, $D = 1.1$ mm, $T_{sat} = 31^{\circ}\text{C}$, $G = 400$ kg/m ² s, $\bar{x}_{hpot} = 60\%$, $\bar{q}''_{hpot} = 120$ kW/m ² , $\Delta q''_{hpot} = 40$ kW/m ² and $f = 1$ Hz	109
Figure 6.6 – Illustration of the effect of the heat flux waveform on the frequency distribution of the average wall superheat temperature	110
Figure 6.7 – Illustration of the frequency distribution of the difference of amplitude of wall superheat temperature adopting the saw tooth heating pulses as the baseline.....	111
Figure 6.8 – Fourier transform of the heat flux signal for $\Delta q''_{hpot} = 40$ kW/m ² under different waveforms	111
Figure 6.9 – Illustration of the effect of the heat flux amplitude on the frequency distribution of the average wall superheat temperature	112
Figure 6.10 – Illustration of the effect of heat flux amplitude on the frequency distribution of the amplitude of wall superheat temperature.....	113
Figure 6.11 – Illustration of the heat flux waveform frequency on the frequency distribution of the average wall superheat temperature	114
Figure 6.12 – Illustration of the influence of heat flux frequency on the amplitude of the wall superheat temperature oscillations.....	114
Figure 6.13 – Illustration of the influence of the average heat flux level on the frequency distribution of the average wall superheat temperature	115
Figure 6.14 – Illustration of the effect of the average heat flux level on the frequency distribution of the average heat transfer coefficient	115
Figure 6.15 – First partial derivative of the heat transfer coefficient with respect to the heat flux (or the heat transfer coefficient sensitivity to the heat flux) according to the method of Kanizawa et al. (2016), R134a and $T_{sat} = 31^{\circ}\text{C}$	116
Figure 6.16 – Illustration of the influence of the average heat flux level on the frequency distribution of the amplitude of wall superheat temperature variation.....	117
Figure 6.17 – Boiling curve for R134a at $G = 400$ kg/m ² s, $D = 0.5$ mm, $T_{sat} = 31^{\circ}\text{C}$ and $x = 60\%$ according to Kanizawa et al. (2016), illustrating the reduction of wall superheat temperature amplitude with the increment of the average heat flux.....	118
Figure 6.18 – Illustration of the influence of vapor quality on the frequency distribution of the difference of the average wall superheat temperature	119
Figure 6.19 – Illustration of the influence of the vapor quality on the frequency distribution of the average heat transfer coefficient	119
Figure 6.20 – Heat transfer coefficient vs. vapor quality according to the method of Kanizawa et al. (2016) for R134a at $T_{sat} = 31^{\circ}\text{C}$	120

Figure 6.21 – Influence of vapor quality on the frequency distribution of the amplitude of fluctuations of the wall superheat temperature	121
Figure 6.22 – Illustration of the influence of the increment of the average heat transfer coefficient (and consequently the slight reduction of the time constant) on the improvement of wall superheat temperature oscillations	122
Figure 6.23 – Illustration through boiling curves of the effect of vapor quality variations on ΔT_w under fixed heat flux average value and amplitude based on the method of Kanizawa et al. (2016) for R134a at $G = 600 \text{ kg/m}^2\text{s}$ and $T_{sat} = 31^\circ\text{C}$	122
Figure 6.24 – Illustration of the influence of the mass velocity on the frequency distribution of the average wall superheat temperature	123
Figure 6.25 – Illustration of the effect of the mass velocity on the frequency distribution of the average heat transfer coefficient	124
Figure 6.26 – Illustration of the effect of the mass velocity on the frequency distribution of the amplitude of the wall superheat temperature	124
Figure 6.27 – Illustration based on boiling curves of the effects of mass velocity on the variation of the wall superheat temperature based on the method of Kanizawa et al. (2016) for R134a at $T_{sat} = 31^\circ\text{C}$ and $x = 8\%$	125
Figure 6.28 – Comparison among the predicted and the experimental average heat transfer coefficients.....	127
Figure 6.29 – Comparison of the predicted and the experimental wall superheat temperature half-amplitude for the entire database	131
Figure 6.30 – First partial derivative of the heat transfer coefficient with respect to the heat flux for the eight HTC methods, R134a at $T_{sat} = 31^\circ\text{C}$, $D = 0.5 \text{ mm}$, $G = 400 \text{ kg/m}^2\text{s}$ and $x = 60\%$	133
Figure 6.31 – Schematic illustration of the estimation of the thermal resistance related to the $\Delta T_w'$ from the boiling curve.....	136
Figure 6.32 – Block diagram illustrating the superposition of the effects of the flow boiling mechanisms and the thermal inertia of the tube walls for estimating the fluctuations of wall superheat temperature for transient heat loads	137
Figure 6.33 – Summary of the methodology for estimating the wall superheat temperature dynamic behavior under transient and cyclical heat loads.....	137
Figure 6.34 – Comparison of the wall superheat temperature transient behavior for direct estimation through the use of experimental data for every time instant for estimating HTC (a), the methodology presented in this study (b) and experimental data (c) for $\tau = 180 \text{ ms}$, R134a, $D = 0.5 \text{ mm}$, $T_{sat} = 31^\circ\text{C}$, $G = 600 \text{ kg/m}^2\text{s}$, $\bar{x}_{hpot} = 40\%$, $\bar{q}''_{hpot} = 80 \text{ kW/m}^2$, $\Delta q''_{hpot} = 40 \text{ kW/m}^2$ and $f = 0.5 \text{ Hz}$	138

Figure 6.35 – Experimental vs. estimated transient behaviors of the wall superheat temperature for $\tau = 180$ ms, R134a, $D = 0.5$ mm, $T_{sat} = 31^\circ\text{C}$, $G = 600$ kg/m²s, $\bar{x}_{hpot} = 40\%$, $\bar{q}''_{hpot} = 120$ kW/m², $\Delta q''_{hpot} = 40$ kW/m² and $f = 1$ Hz 139

Figure 6.36 – Experimental vs. estimated transient behaviors of the wall superheat temperature under saw tooth heating pulses for $\tau = 180$ ms, R134a, $D = 0.5$ mm, $T_{sat} = 31^\circ\text{C}$, $\bar{x}_{hpot} = 60\%$, $\bar{q}''_{hpot} = 120$ kW/m², $\Delta q''_{hpot} = 40$ kW/m² and $f = 1$ Hz..... 140

Figure 6.37 – Experimental vs. estimated transient behaviors of the wall superheat temperature under sinusoidal heating pulses for $\tau = 180$ ms, R134a, $D = 0.5$ mm, $T_{sat} = 31^\circ\text{C}$, $G = 600$ kg/m²s, $\bar{q}''_{hpot} = 80$ kW/m², $\Delta q''_{hpot} = 40$ kW/m² and $f = 0.5$ Hz. 140

Figure 6.38 – Experimental vs. estimated transient behaviors of the wall superheat temperature under square heating pulses for $\tau = 180$ ms, R134a, $D = 0.5$ mm, $T_{sat} = 31^\circ\text{C}$, $\bar{x}_{hpot} = 40\%$, $G = 400$ kg/m²s, $\Delta q''_{hpot} = 40$ kW/m² and $f = 0.5$ Hz..... 141

LIST OF TABLES

Table 1.1 – Operating temperature ranges of IC devices for different applications.....	31
Table 1.2 – Performance comparison based on literature of different technologies for high heat flux removal ($q'' > 3 \text{ MW/m}^2$) using water as the coolant fluid	35
Table 2.1 — Summary of the prediction methods for flow boiling heat transfer in microchannels	53
Table 3.1 – Summary of studies concerning non-uniform heating on flow boiling inside evaporators.....	60
Table 4.1 – Micropump operational parameters	79
Table 4.2 – Main specification and associated errors of the sensors and actuators installed in the test bench.....	82
Table 5.1 – Range of experimental conditions and main results of the diabatic single-phase tests for estimating the relative heat losses to the environment.....	84
Table 5.2 – Experimental uncertainties associated with measured (left) and estimated (right) parameters.....	95
Table 6.1 – Experimental conditions evaluated in the present study.....	106
Table 6.2 – Statistical parameters resulting from the comparison of the experimental data and the corresponding predictions for the average HTC under transient heat loads	127
Table 6.3– Statistical parameters resulting from the comparison of the predictions and experimental results for the wall superheat temperature half-amplitude.....	131
Table A.1 – Experimental mass velocity uncertainties.....	155
Table A.2 – Experimental uncertainties for the local heat flux	156
Table A.3 – Experimental uncertainties for the local heat transfer coefficient	157
Table A.4 – Experimental uncertainties for the vapor quality	159

NOMENCLATURE

Alphabetic Symbols

Symbol	Nomenclature	Dimensions
A	Cross-sectional Area	$[m^2]$
c	Heat Capacity	$[J/kg\ K]$
D	Diameter	$[m]$
f	Friction Factor	$[-]$
F	Convective Effects Enhancement Factor	$[-]$
f	Frequency	$[Hz]$
G	Mass Velocity	$[kg/m^2s]$
g	Gravitational Acceleration at Sea Level	$[m/s^2]$
h	Enthalpy	$[J/kg]$
I	Electrical Current	$[A]$
J	Superficial Velocity	$[m/s]$
k	Thermal Conductivity	$[W/m\ K]$
L	Length	$[m]$
ΔL	Discrete Element Length	$[m]$
\dot{m}	Mass Flow Rate	$[kg/s]$
n	Asymptotic Coefficient	$[-]$
p	Absolute Pressure	$[Pa]$
Δp	Pressure Drop	$[Pa]$
\dot{P}	Electrical Power Output (DC Source)	$[W]$
\dot{Q}	Heat Removal Rate	$[W]$
q''	Heat Flux	$[W/m^2]$
$\Delta q''$	Heat Flux Half-Amplitude	$[W/m^2]$
R	Gas Constant	$[J/mol\ K]$
R^2	Coefficient of Determination	$[-]$
S	Slip Ratio (Gas-liquid Flow)	$[-]$

Symbol	Nomenclature	Dimensions
S	Nucleate Boiling Suppression Factor	[—]
s	Complex Variable (Laplace Transform)	[1/s]
T	Temperature	[°C]
ΔT	Superheat/Subcooling Temperature Difference	[K]
$\Delta T'$	Temperature Fluctuating Component	[K]
t	Time	[s]
V	Electric Potential Difference	[V]
\dot{V}	Volumetric Flow Rate	[m ³ /s]
\dot{W}	Pump Power	[W]
x	Vapor Quality	[—]

Greek Symbols

Symbol	Nomenclature	Dimensions
α	Heat Transfer Coefficient	[W/m ² K]
γ	Surface Tension	[N/m]
ε	Void Fraction	[—]
λ	Parcel of the Data Within a Deviation Band	[%]
μ	Viscosity	[N/m ² s]
ρ	Density	[kg/m ³]
σ	Relative Heat Losses	[—]
τ	Time Constant	[s]
ϕ	Two-Phase Flow Multiplier (Pressure Drop)	[—]
ψ	Mean Absolute Deviation	[%]

Subscripts

Symbol	Nomenclature
1θ	Single-phase
2θ	Two-phase

Symbol	Nomenclature
<i>accel</i>	Accelerational
<i>bg</i>	Background
<i>c</i>	Convection
<i>diff</i>	Differential (Pressure)
<i>f</i>	Fluid
<i>fb</i>	Flow Boiling
<i>fric</i>	Friction
<i>grav</i>	Gravitational
<i>h</i>	Related to the Enthalpy
<i>H</i>	Hydraulic Diameter
<i>hom</i>	Homogeneous
<i>hpot</i>	Hotspot
<i>i</i>	Discrete Space Index
<i>in</i>	Inlet
<i>int</i>	Internal
<i>j</i>	Discrete Time Index
<i>l</i>	Liquid Phase
<i>lo</i>	Liquid Only
<i>lv</i>	Difference from Liquid to Vapor (Properties)
<i>max</i>	Maximum
<i>mod</i>	Modified
<i>nb</i>	Nucleate Boiling
<i>out</i>	Outlet
<i>p</i>	Constant Pressure (Heat Capacity)
<i>pre</i>	Pre-heater
<i>sat</i>	Saturation (Thermodynamic)
<i>sub</i>	Subcooled
<i>tc</i>	Thermocouple

Symbol	Nomenclature
v	Vapor Phase
vo	Vapor Only
w	Wall

Dimensionless Numbers

Symbol	Nomenclature	Definition
Bd	Bond Number	$\frac{(\rho_l - \rho_v)gL^2}{\gamma}$
Bi	Biot Number	$\frac{\alpha L}{k}$
Bo	Boiling Number	$\frac{q''}{\dot{m} h_{lv}}$
Co	Confinement number	$\frac{1}{L} \sqrt{\frac{\gamma}{g(\rho_l - \rho_v)}}$
Fr	Froude Number	$\frac{J}{\sqrt{gL}}$
Kn	Knudsen Number	$\frac{\mu_v \sqrt{\pi}}{L \rho_v \sqrt{2RT}}$
Nu	Nusselt Number	$\frac{\alpha L}{k}$
Pr	Prandtl Number	$\frac{c_p \mu}{k}$
Re	Reynolds Number	$\frac{\rho J L}{\mu}$
We	Weber Number	$\frac{\rho J^2 L}{\gamma}$

Acronyms

Symbol	Nomenclature
<i>CHF</i>	Critical Heat Flux
<i>CPU</i>	Computer Processing Unit
<i>DAQ</i>	Data Acquisition
<i>DC</i>	Direct Current
<i>HALF</i>	High-amplitude Low-frequency
<i>HCPV</i>	High-concentration Photovoltaics
<i>HTC</i>	Heat Transfer Coefficient
<i>IC</i>	Integrated Circuit
<i>LAHF</i>	Low-amplitude High-frequency
<i>PV</i>	Photovoltaics

TABLE OF CONTENTS

1. INTRODUCTION	31
1.1. Study Motivation	31
1.2. Study Objectives	39
1.3. Text Structure.....	39
2. FUNDAMENTALS OF TWO-PHASE FLOW AND FLOW BOILING IN MICROCHANNELS	41
2.1. General Parameters	41
2.2. Macro to Micro Scale Transition	44
2.3. Two-phase Flow Patterns in Small Diameter Channels	47
2.4. Two-phase Flow Pressure Drop.....	49
2.5. Heat Transfer Mechanisms and Prediction Methods for Flow Boiling Inside Small Diameter Channels.....	50
3. LITERATURE REVIEW	57
3.1. Introduction.....	57
3.2. Steady Non-Uniform Heat Dissipation in Microchannels-based Heat Sinks Operating Under Single-phase Flow	57
3.3. Steady Non-Uniform Heat Dissipation in Microchannels-based Heat Sinks Operating Under Flow Boiling.....	59
3.4. Transient Heat Loads to Flow Boiling in Microchannels.....	66
3.5. Conclusions.....	69
4. EXPERIMENTAL APPARATUS	71
4.1. Test Bench	71
4.1.1. Auxiliary Circuit	74
4.1.2. Pre-heater and Test Section	75
4.1.3. Instrumentation and Apparatus	78
5. EXPERIMENTAL PROCEDURE AND DATA REDUCTION.....	83
5.1. Introduction.....	83
5.2. Energy Balance and Heat Losses Estimation.....	83

5.2.1.	Heat Losses Evaluation.....	83
5.2.2.	Analytical Expressions for the Heat Losses.....	84
5.2.3.	Procedure for Estimating Heat Losses During Flow Boiling Tests.....	85
5.3.	Data Reduction Procedure	87
5.3.1.	Presentation of the Model	88
5.4.	Experimental Uncertainties.....	95
5.5.	Experimental Validation of the Test Apparatus and Data Reduction Procedure	96
5.6.	Experimental Procedure.....	99
5.6.1.	Transient Heating Flow Boiling Tests	99
5.6.2.	Uniform Heating Single-Phase Flow	100
5.7.	Influence of the Fluid Saturation Temperature on the Wall Superheat Temperature Dynamics	100
5.8.	Characterization of the Temperature Sensor Dynamic Response.....	102
6.	RESULTS.....	105
6.1.	Introduction.....	105
6.2.	Experimental Database Description.....	105
6.3.	Characteristic Behavior of the Wall Superheat Temperature and the Heat Transfer Coefficient According to the Heating Pulses Waveforms.....	106
6.4.	Parametric Analysis of the Transient Behavior of the Wall Superheat Temperature	109
6.4.1.	Waveform Effects	110
6.4.2.	Heat Flux Amplitude Effects	112
6.4.3.	Effects of Heat Flux Frequency	113
6.4.4.	Effects of the Average Heat Flux Level	115
6.4.5.	Vapor Quality Effects	118
6.4.6.	Effects of Mass Velocity.....	123
6.5.	Assessment of Flow Boiling Prediction Methods to Transient Heating.....	125
6.5.1.	Average Heat Transfer Coefficient.....	126
6.5.2.	Wall Superheat Temperature Amplitude	130

6.6. Methodology for Estimating the Dynamic Behavior of Wall Superheat Temperature under Transient and Cyclical Heat Loads.....	134
6.6.1. Presentation of the Methodology	134
6.6.2. Validation of the Methodology	138
7. CONCLUSIONS AND FUTURE WORK.....	143
7.1. Conclusions.....	143
7.2. Future Work.....	145
REFERENCES	147
APPENDIX A: MEASUREMENT UNCERTAINTIES AND ERROR PROPAGATION	155

1. INTRODUCTION

1.1. Study Motivation

The semiconductor industry experiences a fast advance towards the miniaturization of its components from early 1980s. Following this trend, the heat flux dissipated by electronic devices largely increased and their thermal management became a critical design issue. According to Benda, Gowar and Grant (1999), the maximum junction temperature recommended for semiconductors is 150°C for silicon, 200°C for gallium arsenide, 400°C for silicon carbide and 700°C for diamond. Increasing the maximum junction temperature is desired in applications such as high power laser diodes because it allows to increase the electrical current density. On the other hand, high junction temperatures can impact severely on the failure mechanisms of electronic devices such as electromigration, stress migration and time-dependent dielectric breakdown (Sharma et al., 2007).

Most modern electronic circuits are made from silicon due to its physical properties as well as its abundance, which implies on lower manufacturing costs. Integrated circuits (ICs) are generally specified to work under temperatures between 60 and 150°C, as illustrated in Tab. 1.1. It is important to note that exceeding the temperature range limits does not necessarily imply on immediate circuit failure, but the IC will be more susceptible to failure mechanisms and, as a result, its reliability and lifetime will be greatly reduced.

Table 1.1 – Operating temperature ranges of IC devices for different applications

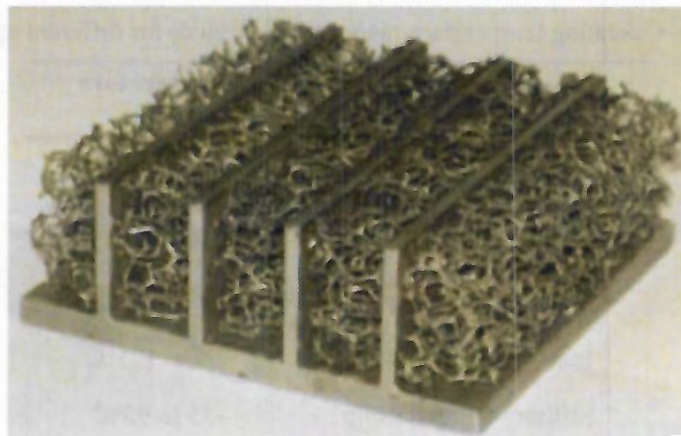
Category	Temperature Range
Computer	15 to 60°C
Telecommunications	-40 to 85°C
Commercial Aircraft	-55 to 95°C
Industrial/Automotive	-55 to 125°C
Military Ground/ Ship	-55 to 95°C
Space	-40 to 85°C
Military Avionics	-55 to 95°C
Automotive (Under the hood)	-65 to 150°C

Source: Pfahnl, Lienhard and Slocum (1999)

Agostini et al. (2007) reported a study conducted by an international consulting company that forecasted 4.1 billion per year the global market for cooling of computers and telecom equipment, with a panorama of market growth for the sub sequential years. In the same study, the consulting company identified a technological transition from traditional air-cooling methods to more sophisticated and efficient cooling solutions. In 2005, Kandlikar pointed out that the current physical limits of air-cooling technology were around 1 MW/m^2 , with modern ICs easily overcoming this limit. More recently, Mudawar (2013) suggested that high heat flux dissipation is not only limited to applications such as computer chips, but similar demands emerge in early 1990s for high-concentration photovoltaics (HCPV), lasers, particle accelerators, fuel cell and radar applications. From all new advanced cooling techniques currently in development, Agostini et al. (2007) points out that the most promising technologies are single-phase/two-phase flow in porous media, impingement jets and single-phase/two-phase flow in microchannels.

The use of heat sinks composed of metallic porous layers and fins, as illustrated in Fig. 1.1, is one of the proposed solutions to cope with high heat flux removal. Porous heat exchangers exhibit enhanced heat transfer efficiency due to the increase of the area-to-volume ratio attributed to pores presence and the heat transfer increase promoted by interstitial mixture effects. Despite of its reasonable thermal performance, porous heat sinks imposes very large pressure drop, which limit their application.

Figure 1.1 – Metallic porous media heat sink (50 mm x 50 mm x 25 mm)

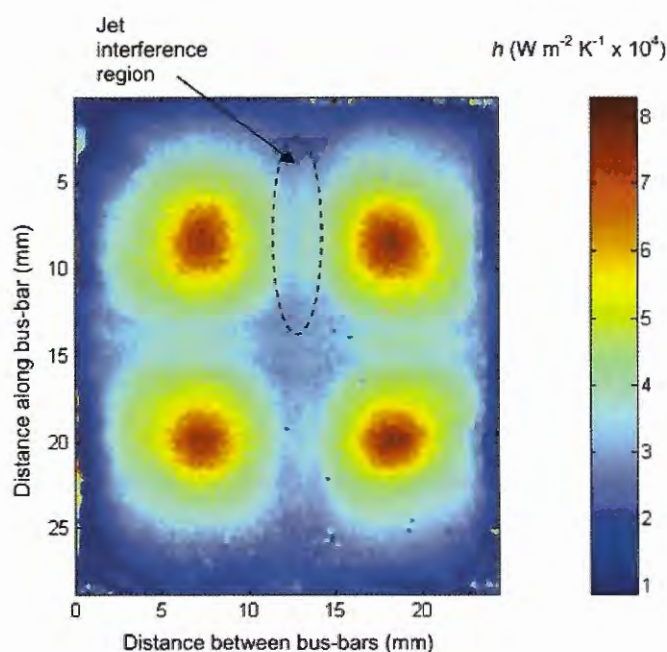


Source: Feng et al. (2015)

Impingement jets are also an alternative technology that has already been employed with success for thermal management of electronic components. The great heat removal efficiency of this technology is attributed mainly to the high heat transfer coefficients on the jet

stagnation region. The jets impinge directly on the cooling zone, removing the necessity of an extra thermal interface resistance between the components and cooling fluid. According to Sung and Mudawar (2006), the major disadvantage of this method is the rapid degradation of the heat transfer coefficient as we move away from the stagnation zone, as shown in Fig. 1.2. This problem can be overcome by reducing the jet diameter and using compact arrays of jets as demonstrated by Brunschwiler et al. (2006).

Figure 1.2 – Heat transfer coefficient distribution obtained from an array of four impingement jets to cool densely packed photovoltaic cells



Source: Royne and Dey (2006)

Tuckerman and Pease (1981) were the first authors in literature to evaluate single-phase flow in microchannels for cooling purposes. When compared to conventional channels, the reduced diameter channels exhibit greater wetted area to volume ratio, favoring high heat transfer coefficients. As indicated by Agostini et al. (2007), the main drawback of employing single-phase flow is the thermal gradient along the fluid, as it only exchanges sensible heat. To keep thermal gradient within acceptable limits, the mass flow rate needs to be increased, requiring greater pumping power. Figure 1.3 illustrates a commercial parallel microchannels heat sink that operates with water as the working fluid.

Figure 1.3 – Commercial heat sink for CPUs based on microchannels and using water as the working fluid. Model Nepton 140XL from Cooler Master



Source: Cooler Master Website

Flow boiling inside microchannels has advantage of exchanging both sensible and latent heat. Due to physical phenomena underlying boiling process such as fluid agitation promoted by bubble growth and coalescence in isolated bubbles regime and thin liquid film evaporation in annular flows, the heat transfer coefficient is superior when compared to single-phase flow. With respect to geometrical effects caused by diameter reduction, Ong and Thome (2011) argues that the bubble confinement in microchannels modifies the relative importance of the forces acting on the flow such as inertial, surface tension and gravitational, increasing the heat transfer coefficient when compared to conventional channels.

Mudawar (2013) reported that one of the main difficult encountered when employing two-phase flow for cooling is the limited understanding of two-phase transport behavior at small scales, making the thermal design of these devices heavily dependent on empirical correlations, which are usually developed for restrict range of operational conditions and with dubious extrapolation capability. In addition to the hardship of predicting the heat transfer coefficient for design purposes, flow instabilities can lead to a premature critical heat flux (CHF) (Mudawar, 2013). In microchannels, the confined growth of bubbles causes vapor expansion in both upstream and downstream directions and induces flow instabilities, which takes form as pressure oscillations. If the momentum of the coming liquid at the channel

entrance is not enough to overcome the pressure drop across the channel, the vapor at channel exit flows backwards to the channel inlet, causing premature CHF.

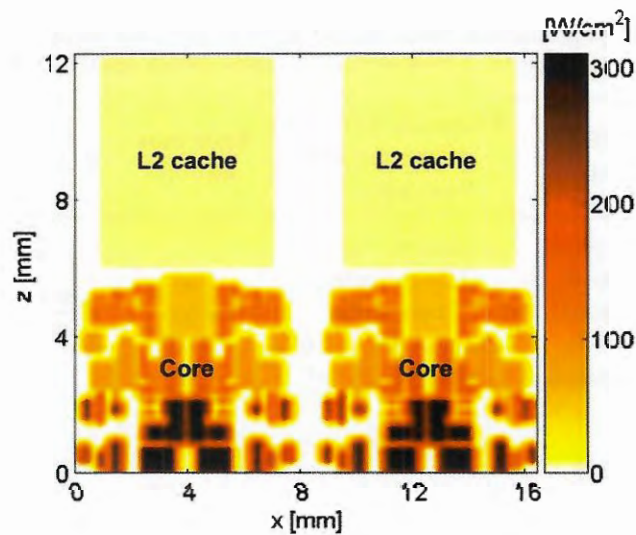
Table 1.2 presents a comparison concerning the heat removal efficiency and capability between the four cooling methods discussed so far. From this table, it can be seen that the lowest heat removal to pumping power ratio occurs for single-phase flow in porous media, which can be explained by the inherent enormous pressure drop. Although its volumetric flow rate was more than two times superior, the average heat transfer coefficient obtained by Zhang et al. (2014) for single-phase conditions was four times smaller than the average heat transfer coefficient obtained by Kalani and Kandlikar (2016). This result discloses the great heat transfer efficiency exhibited by flow boiling in microchannels. Also, it can be seen from Tab. 1.2 that the heat removal efficiency of flow boiling in microchannels, defined by the ratio between the heat load to the pump power (calculated by the product of the volumetric flow rate and total pressure drop), is at least two times superior than the second most efficient method (impingement jets array).

Table 1.2 – Performance comparison based on literature of different technologies for high heat flux removal ($q'' > 3 \text{ MW/m}^2$) using water as the coolant fluid

Author	Cooling Method	Material, Hydraulic Diameter and Footprint Area	Flow rate and Δp	q''_{max}	\overline{HTC} (kW/m ² K)	$\frac{\dot{Q}}{\dot{W}}$
Hetsroni, Gurevich and Rozenblit (2006)	Single-phase flow in porous media channels	Stainless Steel, 32% porosity, Rectangular channel, $D_H = 1.67 \text{ mm}$, $5 \times 2 \text{ mm}^2$	0.24 L/min, 464 kPa	$6 \frac{\text{MW}}{\text{m}^2}$	109	57
Brunschwiler et al. (2006)	40.000 Impingement Jets array	Silicon, $D_{jet} = 0.025 \text{ mm}$, $H_{jet} = 0.1 \text{ mm}$, $14 \times 14 \text{ mm}^2$	2.5 L/min, 35 kPa	$4 \frac{\text{MW}}{\text{m}^2}$	67	1013
Zhang et al. (2014)	Single-phase flow in parallel small channels	Silicon, 100 Rectangular channels, $D_H = 0.085 \text{ mm}$, $10 \times 10 \text{ mm}^2$	0.46 L/min, 215 kPa	$10 \frac{\text{MW}}{\text{m}^2}$	75	607
Kalani and Kandlikar (2016)	Two-phase flow in parallel small channels	Cooper, 26 Rectangular channel, $D_H = 0.185 \text{ mm}$, $L = 10 \text{ mm}$, $10 \times 10 \text{ mm}^2$	0.2 L/min, 30 kPa	$10 \frac{\text{MW}}{\text{m}^2}$	295	2512

Non-uniform heat dissipation is inherent to several applications, e.g. CPUs and solar concentrating systems. The term hotspot is commonly used to refer to a region where the heat flux is much greater than its vicinities. Similarly, transient hotspots are characterized by high spatial and temporal variations of the dissipated heat flux. Because the temperature peaks are most likely to occur at the hotspots, proper thermal management is required to improve the temperature uniformity. Hamman et al. (2007) suggested the following two critical conditions to estimate the maximum allowed heat dissipation rate of a given device: the first critical condition is when the total power is limited by the average temperature, calculated as the ratio of average footprint heat flux to the overall heat transfer coefficient; the second critical condition takes into account the non-uniform heat dissipation and considers that the heat dissipation rate is limited by the peak temperatures at hotspot regions, which can cause the local temperature to exceed maximum allowed junction temperature even for low average heat fluxes. An example of a typical power map of a late CPU is shown in Fig. 1.4.

Figure 1.4 – Power map of a 45 nm Intel Core 2 Duo processor

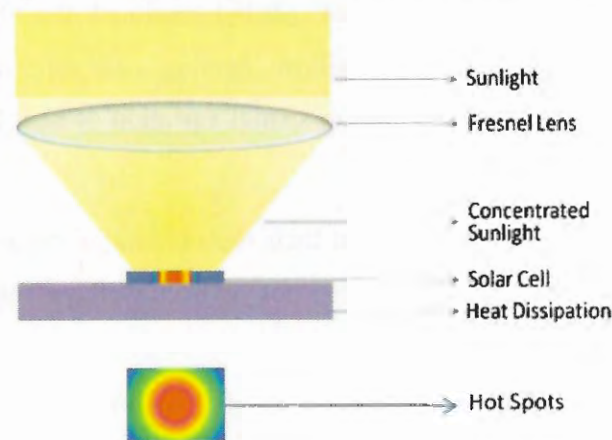


Source: Kim et al. (2010)

According to Fig 1.4, spatially distributed hotspots are present and the power density varies between 113 kW/m² for L2 cache region up to a maximum power density of 3050 kW/m² at the core, where the density of transistors is greater. The power map of Fig. 1.4 illustrates a typical case where the peak temperatures at hotspot regions limits the maximum allowed heat dissipation rate. Its worth mentioning that the power map shown in Fig. 1.4 was obtained from the averaged heat flux measurements over a time period, hence it does not reveal the rapid variations of the instantaneous dissipated heat flux caused by the fluctuations of CPU load.

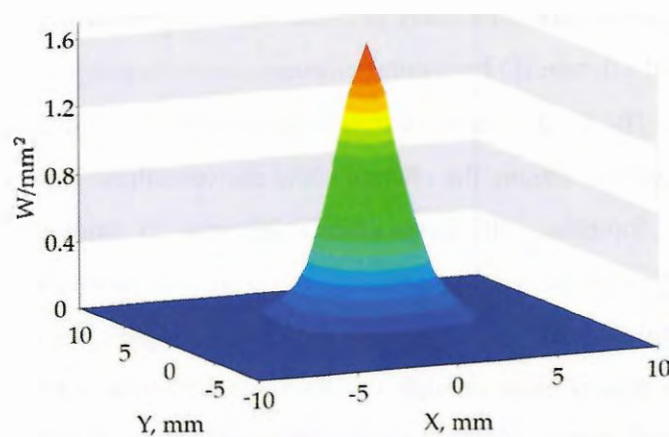
Although most of the studies from literature deal with hotspot mitigation on CPUs, it is important to note that non-uniform heat dissipation is also found in important applications such as photovoltaic (PV) concentrating solar cells as indicated by Baig, Heasman and Mallick (2012) and illustrated in Figs. 1.5 and 1.6. Cooling of concentrator PV panels is a critical issue in their design and operation because temperature non-uniformity degrades energy conversion efficiency and induces thermal stresses, reducing the lifetime of panels. Bahaidarah, Baloch and Gandhidasan (2016) performed a literature review on uniform cooling techniques applied to PV panels and showed that microchannels, impingement cooling and hybrid microchannels-impingement cooling were found to be most effective in dissipating high heat flux from PV surface. Royne et al. (2005) pointed out that microchannels are particularly interesting because they can be incorporated in the cell manufacturing process.

Figure 1.5 – Hotspot development in the solar cell inherent to concentrating systems



Source: Baig et al. (2012)

Figure 1.6 – Typical irradiance distribution on a solar cell



Source: Tien and Shin (2016)

The study of hotspot effects on the heat removal efficiency is a relatively new topic in the literature concerning two-phase cooling solutions through flow boiling in microchannels. Bogojevic et al. (2011) pointed out at the beginning of this decade that the effect of localized high heat flux regions (hotspots) on the system performance is still an open issue that remains unclear. Koo et al. (2002) were the first authors to perform a theoretical study on the effects of non-uniform heat dissipation on the thermal performance of heat sinks based on flow boiling in microchannels.

The majority of studies available in literature concerning non-uniform heat dissipation for flow boiling in heat sinks composed of multiple microchannels considers only the spatial variation of the heat flux and, in general, focus on exploring optimal conditions where the temperature uniformity is maintained under acceptable limits and the pump power requirement is minimized (Cho et al., 2010; Bogojevic et al., 2011; Costa-Patry et al., 2012; Alam et al., 2013; Ritchey et al., 2014). Huang et al. (2016) explored the thermal response of a microchannels-based evaporator under uniform heating and step temporal variations of dissipated heat flux and cold startups, but no spatial variation of heat flux was considered in their study.

Cheng and Xia (2017) identified in their recent state of the art review that transient flow boiling heat transfer in microchannels has not yet been well understood, hence systematic studies on this topic must be performed to provide comprehensive knowledge. To the best of present author's knowledge, solely Miler et al. (2010) contemplated both temporal and spatial variations of dissipated heat flux under flow boiling conditions for a single microscale channel. In their study, the wall temperature was monitored, but unfortunately data reduction for the heat transfer coefficient was not performed.

Within this framework, this study presents novel experimental heat transfer data for flow boiling in 0.5 and 1.1 mm ID horizontal channels under heating conditions characterized by a transient hotspot. The single channel configuration permits to eliminate the effects of flow maldistribution, interactions among the channels and between them and the plenums and heat spreading along the footprint, all these effects inherent to multichannel configuration. Moreover, this study is interested in capturing the transient behavior of the heat transfer coefficient associated with heat flux variations. By using a single-channel with thin walls, the temperature sensor is placed close enough to the channel internal wall in such way that the effects of wall thermal inertia on the transient measurements of wall temperature can be minimized.

1.2. Study Objectives

The main objective of the present work is to perform an experimental evaluation of the transient behavior of wall superheating and heat transfer coefficient during flow boiling for a transient hotspot in small diameter channels. The specific objectives are the following:

- Accomplish a comprehensive literature review concerning the implications of hotspot presence on convective boiling heat transfer inside microchannels;
- Development of a broad experimental dataset for the heat transfer coefficient transient behavior at the hotspot region;
- Perform a parametric study of the influence of several parameters on the transient behavior of the wall superheat temperature;
- Evaluate at which extend does consolidated correlations developed for steady-heating during flow boiling inside microchannels can be used to predict the behavior of the heat transfer coefficient during transient heating;
- Propose a methodology for predicting the wall superheat temperature transient behavior under transient and periodical heat loads during flow boiling inside microchannels.

1.3. Text Structure

This document is organized according to the following chapters:

In Chapter 2, a few fundamental parameters necessary to describe gas-liquid flows are presented and briefly discussed. Also, the two-phase flow patterns and transition criteria from macro to micro scale according to different authors is explored.

In Chapter 3, a literature review on hotspot mitigation solutions and its implications on the cooling efficiency of heat sinks based on microchannels is performed. Then, the few studies concerning transient heating conditions during flow boiling in microchannels are presented.

In Chapter 4, the experimental apparatus used in the present study is described.

In Chapter 5, the data reduction and experimental procedures are detailed. Also, the validation of the experimental apparatus is presented and the characterization of the transient temperature measurements useful bandwidth is performed.

In Chapter 6 the experimental results for transient hotspots are presented. A parametric analysis of the data is performed and the main trends are identified. Also, the experimental results for transient heating are compared against the predictions by correlations developed for steady-heating. At the end of this chapter, a methodology for predicting the transient behavior of wall superheat temperature is presented.

In Chapter 7, the main conclusions drawn from the experimental results are summarized and recommendations for future works are outlined.

2. FUNDAMENTALS OF TWO-PHASE FLOW AND FLOW BOILING IN MICROCHANNELS

In this chapter, the general parameters describing the gas-liquid flow are presented. Also, a review on the transition criteria between macro and micro-scale channels according to different authors is provided. Then, the flow patterns occurring in microchannels are presented and the components of the total pressure drop are outlined and briefly discussed. At the end of the chapter, the heat transfer mechanisms of flow boiling are discussed and a compilation of eight well-known prediction methods in literature for the heat transfer coefficient during flow boiling inside small diameter channels is presented.

2.1. General Parameters

The key quantitative parameters used to characterize and describe the gas-liquid flows are explained in this section. Solving local equations for the mass, momentum and energy conservation is very complex in two-phase flows because of the deformable interfaces between the phases, discontinuities of fluid properties along phase boundaries and existence of turbulent fluctuations (Ishii and Hibiki, 2010). Consequently, time and space averaged parameters are commonly used for describing two-phase flows. All parameters presented in this section are time-averaged and space-averaged on the cross-sectional area.

Vapor Quality

The vapor quality related to mass flow rate $x_{\dot{m}}$ is defined as the ratio of the gas \dot{m}_v to the total mass flow rate \dot{m} , as follows:

$$x_{\dot{m}} = \frac{\dot{m}_v}{\dot{m}_v + \dot{m}_l} = \frac{\dot{m}_v}{\dot{m}} \quad (2.1)$$

The vapor quality is also defined based on the local enthalpy. The thermodynamic vapor quality is helpful when non-equilibrium thermodynamic states are present such as during boiling and condensation under subcooled and superheated conditions. The definition of the equilibrium thermodynamic vapor quality x_h is given by:

$$x_h = \frac{h_{2\phi} - h_{l,sat}}{h_{lv,sat}} \quad (2.2)$$

The thermodynamic vapor quality is negative under subcooled conditions and greater than unity for superheated conditions. When in conditions of thermodynamic equilibrium between the phases, $x_m = x_h$. In this study, the thermodynamic vapor quality is adopted throughout the text because this parameter is directly estimated from energy balances (see Section 5.3.1).

Superficial Velocity and Slip Ratio

The superficial velocity of a phase can be understood as the velocity that this phase would have if it was flowing separately through a channel with the same cross-sectional area of the channel in which the two-phase mixture flows. Thus, the superficial velocities of liquid and gas phases are defined as the ratio of the respective volumetric flow rates \dot{V} to the total cross-sectional area A , as follows:

$$J_l = \frac{\dot{V}_l}{A} \quad (2.3)$$

$$J_v = \frac{\dot{V}_v}{A} \quad (2.4)$$

The total superficial velocity can be interpreted as the velocity of the centroid of a volume containing the two-phase mixture and is given as the sum of superficial velocities of each phase, as indicated:

$$J = J_l + J_v \quad (2.5)$$

The slip-ratio for gas-liquid flows is defined as the ratio of *in-situ* superficial velocities of gas to liquid phase:

$$S = \frac{J_v}{J_l} \quad (2.6)$$

Mass Velocity

The mass velocity (also named as mass flux) of the liquid and gas phases are defined as the ratio of respective mass flow rate to the total cross-sectional area A , as follows:

$$G_l = \frac{\dot{m}_l}{A} \quad (2.7)$$

$$G_v = \frac{\dot{m}_v}{A} \quad (2.8)$$

The total mass velocity is given by the sum of the liquid and gas mass velocities, as follows:

$$G = G_l + G_v = \frac{\dot{m}_l + \dot{m}_v}{A} = \frac{\dot{m}}{A} \quad (2.9)$$

Superficial void fraction

The void fraction is a key two-phase flow characteristic that is necessary to determine important parameters such as two-phase density and viscosity, average mixture velocity, flow pattern, pressure drop and heat transfer coefficient (Thome, 2004). The void fraction in gas-liquid flows is defined as the ratio of the area occupied by the gas phase to the total area, as follows:

$$\varepsilon = \frac{A_v}{A} = 1 - \frac{A_l}{A} \quad (2.10)$$

The void fraction assumes values within the interval $0 \leq \varepsilon \leq 1$, where $\varepsilon = 0$ is the condition when only liquid is present and $\varepsilon = 1$ only gas. For homogeneous two-phase flow, the liquid and gas fractions are assumed to travel at the same velocity, hence $S = 1$ or $J_v = J_l$. Moreover, the velocity profiles of the liquid and gas phases are assumed uniform. Then, the cross-sectional void fraction is given by:

$$\varepsilon = \left(1 + \frac{1-x}{x} \frac{\rho_v}{\rho_l} \right)^{-1} \quad (2.11)$$

The drift-flux void fraction models (e.g. Zuber and Findlay, 1965) assume that the gas and the liquid phases present different *in-situ* velocities ($S \neq 1$) and are non-uniformly distributed along the cross-sectional area. In these models, the effects of the differences between the phases velocities and non-uniformities are accounted by the drift-flux of the gas phase \widetilde{V}_{vj} and the distribution parameter C_0 , respectively. The generic equation for the void fraction models based on the drift-flux void fraction models is given as follows:

$$\varepsilon = \frac{x}{\rho_v} \left[C_0 \left(\frac{x}{\rho_v} + \frac{1-x}{\rho_l} \right) + \frac{\widetilde{V}_{vJ}}{\dot{m}} \right]^{-1} \quad (2.12)$$

where \widetilde{V}_{vJ} and C_0 are obtained through experimental data fitting. The values of \widetilde{V}_{vJ} and C_0 are usually restrict to a specific flow pattern and cross-sectional geometry.

The void fraction models based on the principle of minimum kinetic energy (e.g. Zivi, 1964 and Kanizawa and Ribatski, 2016) assumes that two-phase flow tends to a condition of minimum entropy generation when steady-state is attained. Under this principle, the irreversibilities are minimized. According to this approach, the void fraction ε is given by:

$$\varepsilon = \left[1 + \left(\frac{K_l}{K_v} \right)^{\frac{1}{3}} \left(\frac{\rho_v}{\rho_l} \right)^{\frac{1}{3}} \left(\frac{1-x}{x} \right)^{\frac{2}{3}} \right]^{-1} \quad (2.13)$$

where K_l and K_v are the momentum coefficients accounting for the non-uniformities of the velocity profile along the cross section of the liquid and gas phases, respectively. Zivi (1964) assumes that $\left(\frac{K_l}{K_v} \right)^{\frac{1}{3}} = 1$ while the method of Kanizawa and Ribatski correlates $\left(\frac{K_l}{K_v} \right)^{\frac{1}{3}}$ to the ratio of liquid and gas viscosities and the Froude and Weber numbers for horizontal and vertical flows, respectively, as follows:

$$\left(\frac{K_l}{K_v} \right)^{\frac{1}{3}} = 1.021 \left(\frac{G^2}{(\rho_l - \rho_v)gD} \right)^{-0.092} \left(\frac{\mu_l}{\mu_v} \right)^{-0.368} \quad \text{for horizontal flows} \quad (2.14)$$

$$\left(\frac{K_l}{K_v} \right)^{\frac{1}{3}} = 14.549 \left(\frac{G^2 D}{(\rho_l - \rho_v)\gamma} \right)^{-0.222} \left(\frac{\mu_l}{\mu_v} \right)^{-1.334} \quad \text{for vertical flows} \quad (2.15)$$

2.2. Macro to Micro Scale Transition

Up to present date, there is no consensus in literature about how to define the transition between macro and micro-scale channels. Mehendale, Jacobi and Shah (2000) accomplished an extensive review comparing the heat transfer performance, pressure drop and main design issues concerning compact heat exchangers from 67 different studies from literature covering tube diameters from 0.001 to 6 mm. In order to maintain a concise nomenclature, the authors defined the following arbitrary classification for the tube size: conventional channels ($D_H >$

6 mm), compact channels ($1 \text{ mm} < D_H < 6 \text{ mm}$), meso-channels ($0.1 \text{ mm} < D_H < 1 \text{ mm}$) and microchannels ($0.001 \text{ mm} < D_H < 0.1 \text{ mm}$).

Kandlikar and Grande (2003) proposed a channels classification according also to an arbitrary system based on the range of the channel hydraulic diameters: conventional channels ($D_H > 3 \text{ mm}$), minichannels ($3 \text{ mm} < D_H < 0.2 \text{ mm}$), microchannels ($0.01 \text{ mm} < D_H < 0.2 \text{ mm}$), transition channels subdivided in transition microchannels ($0.001 \text{ mm} < D_H < 0.01 \text{ mm}$) and transition nanochannels ($0.0001 \text{ mm} < D_H < 0.001 \text{ mm}$) and molecular channels ($D_H < 0.0001 \text{ mm}$). The hydraulic diameter range of minichannels was chosen based on the manufacturing feasibility of obtaining small channels through conventional fabrication processes, hence, not requiring special installations (e.g. clean rooms). The inferior limit adopted for microchannels classification according to Kandlikar and Grande (2003) is based on rarefaction effects in gas flows through the Knudsen Number. The rarefaction effect is characterized by the Knudsen number Kn_D , defined as the ratio between the mean free path of gas molecules and the channel hydraulic diameter D_H .

$$Kn_D = \frac{\mu_v \sqrt{\pi}}{D_H \rho_v \sqrt{2RT}} \quad (2.16)$$

Kandlikar and Grande (2003) state that, although the range of transition is determined based on gas flow, it can be also extended to two-phase and liquid flows. Kew and Cornwell (1997) introduced a phenomenological criterion for the transition between macro and microscale based on bubble departure diameter. The criterion of Kew and Cornwell (1997) considers that bubble confinement during boiling is the main responsible for modifying the heat transfer characteristics during convective boiling inside microchannels when compared to larger channels. The confinement number is a dimensionless quantity defined as the ratio of Laplace length to the channel hydraulic diameter, as follows:

$$Co = \frac{1}{D_H} \sqrt{\frac{\gamma}{g(\rho_l - \rho_v)}} \quad (2.17)$$

Kew and Cornell (1997) adopted a confinement number of 0.5 as the transition criterion. In contrast, Tripplett et al. (1999) chooses the transition between scales for a confinement number equal to the unity. In a study pertinent to the linear stability of stratified flows, Brauner and Moalem-Maron (1992) defined the transition from macro to micro scale

based on a modified Bond number Bd_{mod} . The authors argued that the transition from macro to micro scale occurs when Bd_{mod} , given below, is equal to the unity.

$$Bd_{mod} = \frac{(2\pi)^2 \gamma}{(\rho_l - \rho_v) D_H^2 g} \quad (2.18)$$

Tibiriçá and Ribatski (2015) proposed two different phenomenological criteria based on flow patterns for calculating the transitional diameter between macro and micro scales. The first criterion is based on the analysis of minimum diameter for the occurrence of stratified flows, taking into account the effects of contact angle. For a static plug of liquid surrounded by vapor, when the forces due to thermodynamic pressure are equal to the horizontal component of force due to surface tension at the triple contact line (liquid-solid-vapor), the liquid plug is said to be statically stable and the transition diameter is given by:

$$D_H = \sqrt{\frac{8 \gamma \cos\theta}{(\rho_l - \rho_v) g}} \quad (2.19)$$

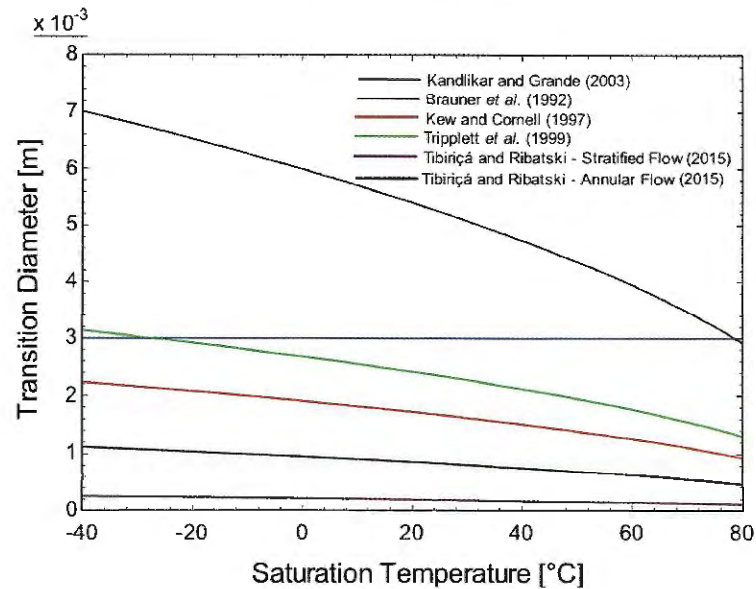
The second transition criterion is based on the liquid film thickness uniformity in annular flows. They took into account the fact that the degree of uniformity of the liquid film is closely related to the channel diameter and vapor velocity. This behavior is associated to the fact that, as the tube diameter is reduced, the surface tension forces overcome gravitational forces. Tibiriçá and Ribatski (2015) adopted a transition from macro to micro scale when the gravitational force is 5% of the surface tension force. The transitional diameter according to their criterion is indicated below:

$$D_H = \sqrt{\frac{\gamma}{20(\rho_l - \rho_v) g}} \quad (2.20)$$

Figure 2.1 illustrates the variation of the transitional diameter with the saturation temperature for R134a according to the different methods presented here. From this figure, it is seen that large discrepancies among the different criteria are present. For 0°C, the criterion of Brauner and Moalem-Maron (1992) predicts a transition diameter of 6 mm while the criterion of Tibiriçá and Ribatski (2015) based on the annular film uniformity predicts a transition of scales at only 0.2 mm. In this study, the 3 mm diameter is adopted as the limit between macro

and micro scale channels, similarly to the studies of Cheng, Ribatski and Thome (2008) and Kandlikar and Grande (2003).

Figure 2.1 – Transitional diameter between macro and micro scale with saturation temperature for R134a according to different criteria



2.3. Two-phase Flow Patterns in Small Diameter Channels

The variations of parameters such as pressure, temperature and mass velocities give rise to a couple of different interfacial geometries between the phases, characterizing different flow patterns (Cheng, Ribatski and Thome, 2008). Depending on the application, some flow patterns can be sought or avoided. For example, the churn flow pattern is usually avoided in tube bundles because this type of flow favors excessive vibrations (Álvarez-Briceño et al., 2017), which can lead to fatigue failure. On the other hand, the annular flow can be preferred in evaporators because the thin film evaporation leads to high heat transfer coefficients. Because the heat transfer coefficient and pressure drop are strongly linked to the prevailing flow pattern, it is important to have reliable methods able to predict the flow patterns and their transitions.

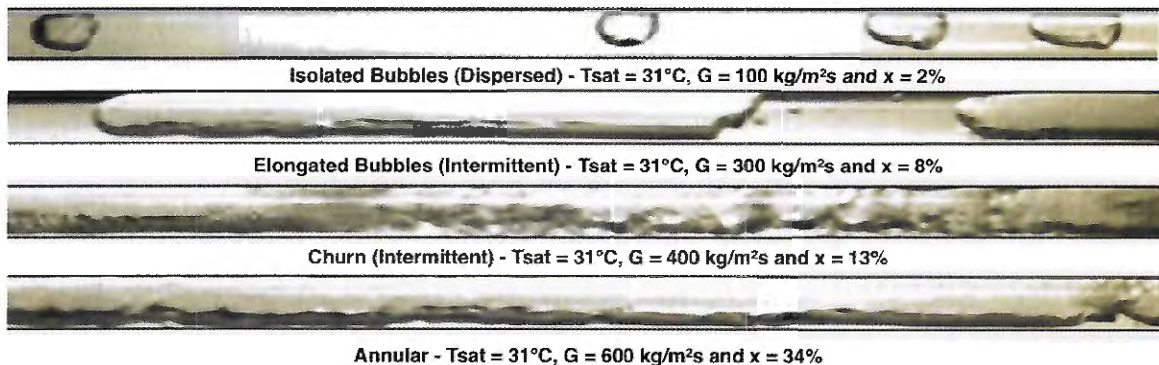
The flow patterns are commonly classified according to subjective criteria such as visual inspection through transparent ducts and with the aid of high-speed cameras. Objective criteria such as spectral analysis of pressure drop and void fraction are also used (Jones and Zuber, 1974). For adiabatic flows and short tube lengths, the void fraction can be usually assumed as constant and, consequently, a prevailing flow pattern is present along the channel.

Contrastingly, diabatic flows exhibits variations of the gas fraction along the flow direction, which gives rises to a sequence of flow patterns.

There are differences regarding the flow pattern characteristics and their transitions between macro and micro scale channels. As the channel diameter decreases, the surface tension forces become more relevant when compared to other forces such as pressure, inertial and gravitational. This causes a reduction of the slip velocity and the flow characteristics become independent of channel orientation with respect to gravity (Tripplett et al., 1999). Only the flow patterns occurring in microscale channels are discussed in this section. If the reader is interested in learning more about the flow patterns occurring in macro scale channels, it should refer to the books of Collier and Thome (1994) and Ishii and Hibiki (2010).

Similarly to vertical flows in macro scale channels, the stratified flow is absent in small diameter channels, even for horizontal flows. Figure 2.2 illustrates the four possible flow patterns according to Sempertégui-Tápia, Alves and Ribatski (2013). For microchannels, generally isolated bubbles flow is present for vapor qualities lower than 10% (Costa-Patry and Thome, 2013). With increasing vapor quality, intermittent flow (elongated bubbles and churn) occurs for vapor qualities of approximately from 15 to 40% according to Costa-Patry and Thome (2013). The intermittent flow is characterized as a transitional flow pattern between isolated bubbles and annular flow. As the vapor quality further increases from 40%, the flow becomes annular and then mist flow.

Figure 2.2 – Flow pattern images for R245fa flowing through a 2.32 mm internal diameter channel.



Source: Sempertégui-Tápia, Alves and Ribatski (2013)

2.4. Two-phase Flow Pressure Drop

The local pressure gradient is a result of the combination of three main components: gravitational, accelerational and frictional (Collier and Thome, 1994). Hence, the pressure gradient can be written as follows:

$$-\frac{dP}{dz_{2\phi-total}} = \frac{dp}{dz_{grav}} + \frac{dp}{dz_{accel}} + \frac{dp}{dz_{2\phi-fric}} \quad (2.21)$$

The gravitational parcel of the gas-liquid flow pressure drop gradient is given as:

$$\frac{dp}{dz_{grav}} = [\rho_l(1 - \varepsilon) + \rho_v\varepsilon]g \sin(\theta) \quad (2.22)$$

where θ is the angle between the channel orientation and the horizontal plane. For horizontal flows, $\theta = 0^\circ$ and consequently $\frac{dp}{dz_{grav}} = 0$.

The accelerational pressure drop accounts for the kinetic energy variations of the flow along the channel. In adiabatic two-phase flows, the vapor quality is usually constant and consequently the kinetic energy variation is negligible (except when liquid flashing effects are relevant). For diabatic flows, the vapor quality changes along the flow direction, causing variations of the void fraction which ultimately results in variations of the flow kinetic energy. Hence, generally, the accelerational pressure gradient cannot be neglected. The equation that describes the average accelerational pressure gradient across an infinitesimal channel length ΔL of constant cross-sectional area is given by:

$$-\frac{\Delta p}{\Delta L_{accel}} = G^2 \left\{ \left[\frac{(1-x)^2}{\rho_l(1-\varepsilon)} + \frac{x^2}{\rho_v\varepsilon} \right]_{out} - \left[\frac{(1-x)^2}{\rho_l(1-\varepsilon)} + \frac{x^2}{\rho_v\varepsilon} \right]_{in} \right\} \quad (2.23)$$

The frictional pressure drop gradient accounts for the flow irreversibilities. Because of the underlying phenomena complexity, the analytical models for estimating the frictional pressure drop gradient are either not accurate enough or restrict to a narrow range of conditions. Consequently, a great number of studies are still devoted to develop new semi-empiric methods for estimating this quantity. The two-phase multipliers (ϕ^2) are used to estimate the frictional parcel of the total pressure gradient and can be interpreted as a correction factor for the two-

phase flow frictional parcel estimated based on single-phase flow of either liquid or gas flows, as follows:

$$\frac{dp}{dz_{2\phi-fric}} = \frac{2f_l G^2}{\rho_l D} \phi_{lo}^2 = \frac{2f_v G^2}{\rho_v D} \phi_{vo}^2 \quad (2.24)$$

In the pertinent literature, the expressions for the two-phase multiplier calculation are function of parameters such as the Lockhart-Martinelli and also to the Reynolds, Froude and Weber numbers. From the classical methods in literature, for estimating the frictional pressure gradient during two-phase flow using two-phase multipliers, it is worth to highlight the following studies: Chisholm (1967), Grønnerud (1972) and Friedel (1979).

Strictly empirical methods for estimating the pressure drop of gas-liquid flows such as the method of Müller-Steinhagen and Heck (1986) and Xu and Fang (2012) rely on mathematical expression obtained by trial-and-error based on experimental data where for $x = 0$, $\Delta p_{2\phi} = \Delta p_l$ and for $x = 1$, $\Delta p_{2\phi} = \Delta p_v$. More recently, Sempertégui-Tápia and Ribatski (2017) developed a strictly empirical method for predicting the frictional pressure gradients in small diameter channels based on the procedure proposed by Muller-Steinhagen and Heck (1986).

Homogeneous models can be also employed for estimating the frictional parcel of pressure drop in gas-liquid flows. In homogeneous models, the pressure drop is estimated similarly to single-phase flow by treating the gas-liquid mixture as a pseudo fluid with density estimated according to $\rho_{hom,2\phi} = \left(\frac{x}{\rho_l} + \frac{1-x}{\rho_v}\right)^{-1}$ and dynamic viscosity according to a relationship from literature such as the method of McAdams (1942) or Cicchiti et al. (1960).

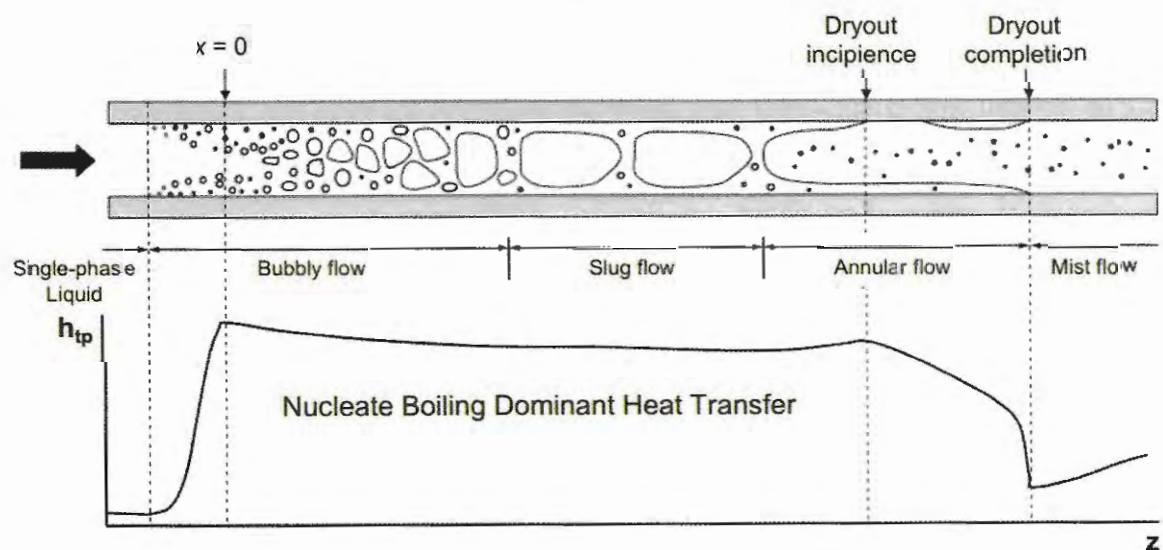
2.5. Heat Transfer Mechanisms and Prediction Methods for Flow Boiling Inside Small Diameter Channels

Flow boiling heat transfer is governed by two main mechanisms: nucleate boiling and convective effects. The nucleate boiling effects are related to the heat transport by the bubble formation and its dynamics, while the convective effects are related to the heat conduction and advection throughout the fluid. When nucleation effects are dominant, the heat transfer coefficient exhibits a strong dependency upon the dissipated heat flux and saturation temperature. On the other hand, when convective effects predominate, the heat transfer coefficient is strongly dependent on the mass velocity and vapor quality. During flow boiling,

the nucleate and convective boiling effects occur concomitantly, hence, the overall heat transfer rate is the result of the complex superposition of these mechanisms.

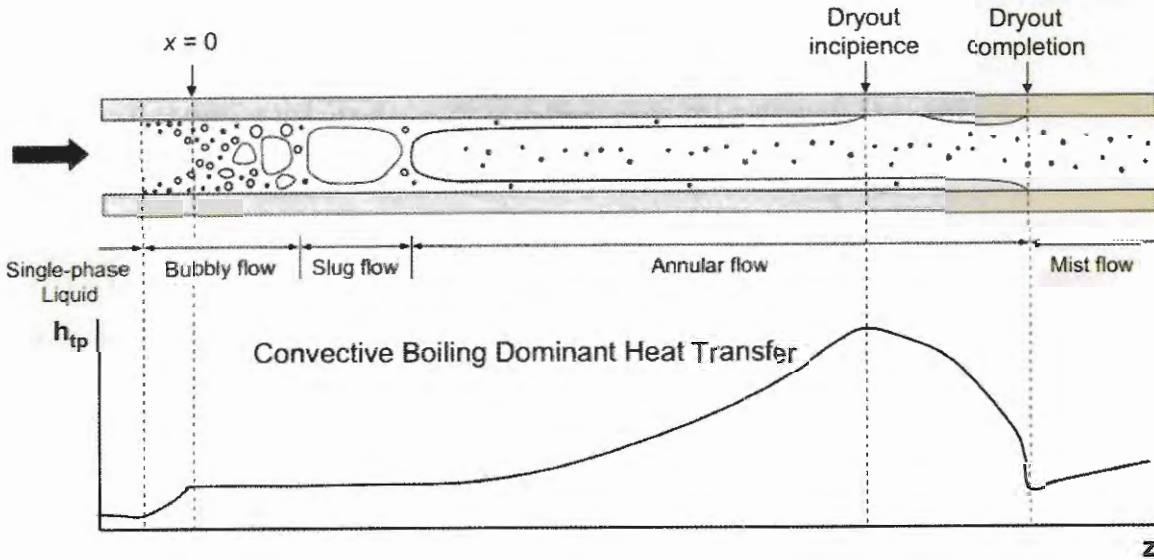
Figure 2.3 and 2.4 illustrates the differences between flow boiling under predominance of nucleate boiling and convective effects according to Kim and Mudawar (2013). In these two figures, subcooled liquid enters the channel. As the bubble nucleation process is triggered in the subcooled region, the heat transfer coefficient promptly elevates and bubbly flow occurs. In nucleate boiling dominant heat transfer (Fig. 2.3), most of the channel length is typically under bubbly and slug flow and the heat transfer coefficient decreases with increasing vapor quality as a result of a gradual suppression of nucleation effects caused by flow acceleration due to increasing void fraction. Conversely, under predominance of convective effects (Fig. 2.4), the heat transfer coefficient rises with increasing vapor quality and most of the channel length is under annular flow. The increment of the heat transfer coefficient with vapor quality is caused by the gradual thinning of annular film. It is worth noting that Figs. 2.3 and 2.4 represent limiting cases, thus, the heat transfer coefficient behavior represented in this figures cannot be take for granted, e.g. Tibirićá and Ribatski (2015) observed bubble nucleation for elongated bubbles and annular flow patterns.

Figure 2.3 – Sequence of flow patterns observed in microchannels for nucleate boiling dominant heat transfer.



Source: Kim and Mudawar (2013)

Figure 2.4 – Sequence of flow patterns observed in microchannels for convective boiling dominant heat transfer.



Source: Kim and Mudawar (2013)

Independently of the dominant heat transfer mechanism, the dryout of annular liquid film is gradual because of the lack of symmetry in the formation and drying of the annular film (Kim and Mudawar, 2013). From the dryout incipience to its completion, the wall intermittently dries and rewets over a short time of period and the heat transfer coefficient abruptly decreases with increasing vapor quality. Therefore, the dryout inception constitutes an important operational limit because, under uniform and constant heat dissipation, it would lead to a sudden rise of the wall temperature due to the rapid degradation of the local heat transfer coefficient. The mist flow occurs right after the dryout completion and its main heat transfer mechanism is the forced convection of gas phase.

Table 2.1 compile eight well-known methods from literature for predicting the heat transfer coefficient during flow boiling inside small diameter channels. In this table, the methods were classified according to the following categories: strictly empirical, superposition of effects and phenomenological. The strictly empirical models rely on the Buckingham π theorem to correlate the heat transfer coefficient to relevant dimensionless parameters such as the Boiling, Weber, Bond and Reynolds numbers as well as the ratio of liquid and gas densities. The methods based on the superposition of effects considers that the resultant heat transfer coefficient is a combination of nucleate boiling and convective effects. In these methods, a suppression factor S and an enhancement factor F are included to account for the gradual suppression of bubbles formation and enhancement of convective effects, respectively. The

phenomenological models assume a given flow pattern and the heat transfer coefficient is modelled based on the specific characteristics and heat transfer mechanisms pertinent to the gas and liquid phases topology.

Table 2.1 — Summary of the prediction methods for flow boiling heat transfer in microchannels

Author	Database	G [kg/m ² s] x [-] q'' [kW/m ²]
Strictly Empirical		
Lazarek and Black (1982)	R113, Circular Single-channel, $D = 3.15$ mm, 738 Data Points	$G = 125 - 750$ $x = 0 - 1$ $q'' = 14 - 380$
Tran et al. (1996)	R12, Rectangular/Circular Single-channel, $D = 2.46$ and 2.92 mm, 296 Data Points	$G = 44 - 832$ $x = 0 - 0.94$ $q'' = 3.6 - 129$
Sun and Mishima (2009)	R11, R12, R123, R134a, R141b, R22, R404a, R407c, R410a, CO ₂ , H ₂ O, Rectangular/Circular Single-channel, $D = 0.21 - 6.5$ mm, 2505 Data Points	$G = 44 - 1500$ $x = 0 - 1$ $q'' = 5 - 109$
Li and Wu (2010)	R11, R12, R22, R134a, R245fa, R235fa, R123, R410a, FC77, H ₂ O, CO ₂ , Propane, Ethanol, $D = 0.16 - 3.1$ mm, Circular Single-channel, 3744 Data Points	$G = 23 - 3570$ $x = 0.1 - 1$
Superposition of Effects		
Kim and Mudawar (2013)	R11, R22, R32, R113, R123, R134a, R152a, R1234yf, R1234ze, R236fa, R245fa, R404a, R407c, R410a, R417a, FC72, CO ₂ , H ₂ O, $D = 0.19 - 6.5$ mm, Single/Multi-channels, 10805 Data Points	$G = 19 - 1608$ $x = 0 - 1$
Kanizawa et al. (2016)	R134a, R245fa, R600a, $D = 0.38 - 2.6$ mm, Single-channel, 2050 Data Points	$G = 49 - 2200$ $x = 0.05 - 0.93$ $q'' = 5 - 185$
Phenomenological		
Thome et al. (2004)	R11, R12, R113, R123, R134a, R141b, CO ₂ , $D = 0.77 - 3.1$ mm, Single/Multi-channel, 1591 Data Points	$G = 50 - 574$ $x = 0.01 - 0.99$ $q'' = 5 - 178$
Costa-Patry and Thome (2013)	R134a, R236fa, R245fa, R1234ze(E), $D = 0.146 - 3.04$ mm, Single/Multi-channel	$G = 100 - 1100$ $x = 0 - 1$ $q'' = 8 - 260$

The method of Lazarek and Black (1982) considers that the nucleate boiling mechanism controls the heat transfer process, hence, the heat transfer coefficient is assumed as independent of vapor quality. In their method, Lazarek and Black (1982) correlated the HTC to the liquid Reynolds number and the Boiling number. Tran et al. (1996) also considered the nucleate boiling effects as dominant, but instead of including the liquid Reynolds number, similarly to Lazarek and Black (1982), the authors replaced it with the Weber number to capture the surface tension instead of viscous effects. Sun and Mishima (2009) observed a weak dependency of the heat transfer coefficient upon the vapor quality on their database. Therefore, these authors correlated the heat transfer coefficient to Boiling, liquid Reynolds and Weber numbers. Likewise, Li and Wu (2010) considered the heat transfer coefficient to be a function of the liquid Reynolds and Boiling numbers, but the Bond number was preferred over the Weber number because it captures the bubble confinement effects in small diameter channels. It is worth mentioning that the methods of Lazarek and Black (1982) and Tran et al. (1996) are based on very restrict databases covering only one refrigerant, while the methods of Sun and Mishima (2009) and Li and Wu (2010) relies on broader databases comprising more than 10 refrigerants.

The methods based on the superposition of effects, which were pioneered by Chen (1966), are based on the estimatives of the nucleate boiling and convective heat transfer coefficients as well as the enhancement and suppression factors. The relationship representing the superposition of effects is similar to mathematical expression originally proposed by Churchill and Usagi (1972) of the type: $HTC_{2\phi} = [(S HTC_{nb})^n + (F HTC_c)^n]^{\frac{1}{n}}$. In this relationship, the asymptotic coefficient n is used to provide a smooth transition between nucleate and convective effects dominant heat transfer. Kanizawa et al. (2016) adopts $n = 1$ and considers the correlation of Stephan and Abdelsalam (1980) and the Dittus-Boelter (1930) equation for estimating the nucleate boiling and convective heat transfer coefficients, respectively. On the other hand, Kim and Mudawar (2013) adopts $n = 2$ and use the same methods of Kanizawa et al. (2016) for estimating the nucleate boiling and convective heat transfer coefficients. The suppression factor S is given as a function of the Boiling number, reduced pressure and vapor quality in the method of Kim and Mudawar (2013), while Kanizawa et al. (2016) considers this parameter to be a function of the Bond and modified Reynolds numbers. The two methods consider that the enhancement factor F is a function of the Lockhart-Martinelli parameter and the Weber number. The method of Kim and Mudawar (2013) was able to predict 80% of the database used in the adjustment of its empirical constants within an

error band of $\pm 30\%$ (10805 data points) and the method of Kanizawa et al. (2016) predicted 97% of its database within $\pm 30\%$ (2050 data points).

The phenomenological methods consider that the heat transfer coefficient is closely linked to the prevailing flow pattern. Thome, Dupont and Jacobi (2004) proposed a three-zone phenomenological model for predicting the heat transfer coefficient based on the elongated bubbles flow pattern. In their three-zone model, transient variations of the local heat transfer coefficient are present and caused by the cyclic passage of a liquid slug, an evaporating elongated bubble and a vapor slug. The local heat transfer coefficient is considered as the time-averaged value of the heat transfer coefficient over a cycle. Besides its efforts on obtaining a complete mechanistic model, the three-zone methodology still relies on the adjustment of five empirical coefficients to the experimental database, which are difficult to predict theoretically. The flow pattern-based prediction method of Costa-Patry and Thome (2013) is based on the combination of the three-zones model (Thome et al., 2004) for intermittent flow and the Cioncollini and Thome (2011) method for evaporating annular two-phase flow. A buffer/transition zone is included in this model to provide a smooth transition between the two flow patterns.

In summary, it is speculated that the four methods based on a strictly-empirical approach presented in Tab. 2.1 are most suitable for predicting the heat transfer coefficient under dominant nucleate boiling effects, as this condition was predominant in their respective databases used for adjusting its empirical coefficients. On the other hand, the methods based on the superposition of effects of Tab. 2.1 relied on experimental databases contemplating both nucleate boiling dominant and convective dominant heat transfer, hence they are expected to be accurate over a wider range of conditions. The mechanistic models seem to be at its early stage given that the pioneering studies in this area are still recent and a small number of these model types is available in literature up to present date. There is a lack in literature of fully-mechanistic models up to present date, as the methods of Thome et al. (2004) and Costa-Patry and Thome (2013) still relies on semi-empiric coefficients obtained through data fitting.

3. LITERATURE REVIEW

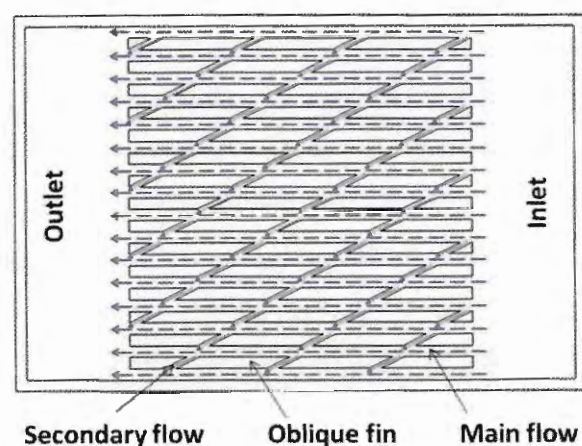
3.1. Introduction

In this chapter, the implications of steady and non-uniform heat dissipation (spatial variations) in the system level performance of heat sinks based on microchannels operating under single-phase flow and flow boiling is addressed. Then, the discussion proceeds to a presentation of the studies covering the effects of transient heat loads (temporal variations) in the flow boiling inside microchannels. At the end, the main conclusions drawn from the evaluated studies and a contextualization of the present study is performed.

3.2. Steady Non-Uniform Heat Dissipation in Microchannels-based Heat Sinks Operating Under Single-phase Flow

Lee, Lee and Chou (2013) experimentally investigated the use of obliquely finned microchannels-based heat sink operating under single-phase flow for the thermal management of hotspots. A schematic diagram of the heat sink used in their study is shown in Fig. 3.1. Oblique fins provide a combined effect of thermal boundary layer redevelopment and generation of secondary flows, enhancing the heat transfer efficiency. Shorter fin pitches lead to intensification of the thermal boundary layer redevelopment and secondary flow generation, increasing the local heat transfer coefficient. The authors found that, by varying the oblique fin length and fin pitch at heat sink, the local heat transfer coefficient could be tailored to meet local heat dissipation and maximum temperature requirements.

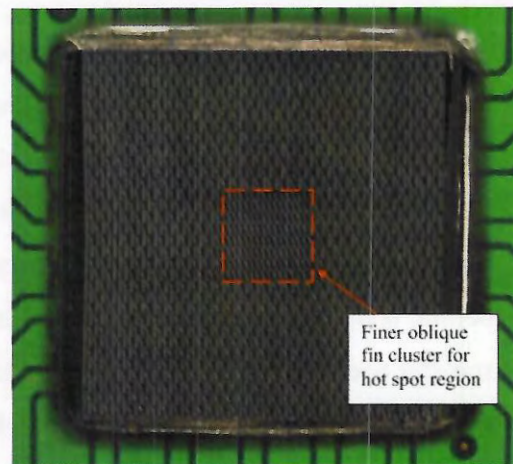
Figure 3.1 – Schematic illustration of a microchannels-based heat sink with oblique fins



Source: Lee et al. (2013)

The authors compared the performance of obliquely variable pitch finned configuration to fixed obliquely pitch and rectangular channels. According to their results, the variable pitch oblique finned heat sink exhibited the lowest maximum temperature and the highest degree of wall temperature uniformity at a pressure drop penalty increase of approximately 10-20% when compared to rectangular channels. Figure 3.2 shows a picture of the heat sink evaluated by Lee et al. (2013) with variable pitch oblique fins to mitigate the effects of a central hotspot. It can be noted in this figure that the region with smaller fin pitch corresponds to the hotspot central region. The goal of such solution is to take advantage of higher heat transfer coefficients with smaller fin pitches.

Figure 3.2 – Heat sink with obliquely finned microchannel of variable pitch evaluated by Lee, Lee and Chou (2013)

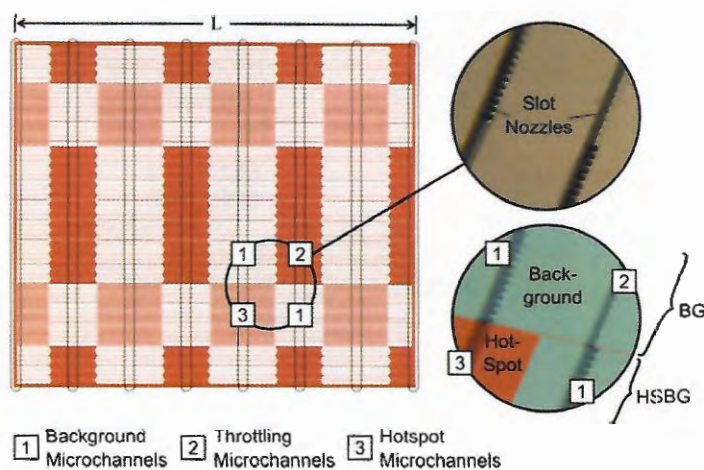


Source: Lee, Lee and Chou (2013)

Sharma et al. (2015) proposed an embedded liquid cooling solution based on microchannels for dissipating non-uniform heat flux in electronics. In their study, a rational distribution of the flow rate was accomplished through passively throttling the flow in regions of low heat flux in order to drive the flow towards the regions of high heat flux. The channels were etched directly into a silicon wafer. The manifolds were placed on top of microchannels to further improve the heat transfer coefficient by the jet impingement at inlet slot nozzles. The heat sink was composed of fine channels over the hotspot, coarse channels over the background and a flow-throttling zone to passively regulate flow distribution in the different regions of the chip. Figure 3.3 illustrates a schematic diagram of tested microchannels heat sink. For this heat sink configuration, the authors were able to successfully improve temperature uniformity while

fulfilling industrially relevant constraint of pressure drop (≤ 0.4 bar) and pumping power ($< 0.3\%$ of total chip power).

Figure 3.3 – Hotspot-targeted embedded microchannel structure



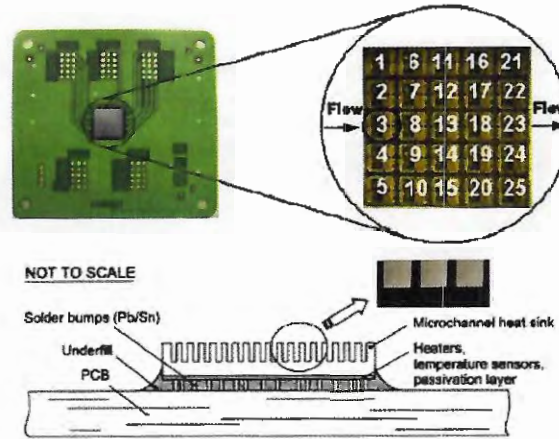
Source : Sharma et al. (2015)

3.3. Steady Non-Uniform Heat Dissipation in Microchannels-based Heat Sinks Operating Under Flow Boiling

The investigations on how the system-level performance is affected by the heat dissipation spatial non-uniformities is relatively recent in literature. Essentially, most of studies concerning the thermal management of hotspots in heat sinks explores optimal fluid-geometry configurations that maximize temperature uniformity while maintaining pump power within acceptable limits. Koo et al. (2002) pioneered the theoretical study of the effects of hotspot location on the thermal performance of microchannels-based heat sinks operating under flow boiling conditions. These authors developed a discrete 1-D model using correlations for estimating flow boiling HTC and Δp to explore optimal geometric designs under non-uniform heating. Unfortunately, this model was not able to evaluate CHF and flow instabilities.

Table 3.1 summarizes the experimental studies found in literature covering the effects of non-uniformities in heat dissipation on the performance of heat sinks based on microchannels under flow boiling. The majority of the studies outlined in Tab. 3.1 used arrays of independent heaters to impose non-uniform heat flux on the evaporator footprint, as shown in Fig. 3.4. The heaters have integrated RTD sensors, hence, they monitor simultaneously the heat flux and wall temperature. Because each heater is controlled individually, different power map arrangements can be generated.

Figure 3.4 - 5 x 5 array of heater elements and a schematic diagram of the microchannel heat sink used by Ritchey et al. (2014).



Source: Ritchey et al. (2014).

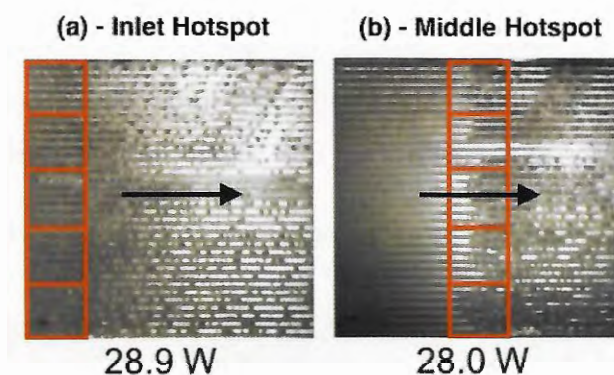
Table 3.1 – Summary of studies concerning non-uniform heating on flow boiling inside evaporators

Reference	Number of Channels and D_H [μm]	Fluid and T_{sat} [$^{\circ}\text{C}$]	Mass velocity [$\text{kg}/\text{m}^2\text{s}$]	Heat Sink Dimensions (L x W) [mm^2] and Heaters Array	Maximum q'' [kW/m^2]	Hotspot orientation and position
Bogojevic et al. (2011)	40, 423	DI Water 100 $^{\circ}\text{C}$	173	15 x 10, 1x3	570	Transverse (inlet, middle, outlet)
Cho et al. (2010)	33, 300	R123 –	40 to 60	20 x 20, 3x3	120	Transverse (inlet, middle, outlet)
Costa-Patry et al. (2012)	135, 148	R245fa 30.5 $^{\circ}\text{C}$	500 to 1050	12.8 x 17.78, 5x7	1600	Point, Transverse (inlet, middle, outlet) and Parallel (middle)
Ritchey et al. (2014)	35, 291	FC77 97 $^{\circ}\text{C}$	890	12.7 x 12.7, 5x5	329	Transverse (inlet, middle and inlet/outlet), Parallel (middle)

Costa-Patry et al. (2012) verified that the position and orientation of hotspots severely impact the HTC distribution and Δp across the heat sink. These authors observed an increment of Δp for transversal hotspots positioned at the channels inlet when compared to middle and downstream positions. The increment of Δp was attributed to the anticipation of boiling front,

which increased the two-phase region length and consequently the overall pressure drop. Moreover, the local HTC at the hotspot region was found to increase with increasing local heat flux. Costa-Patry et al. (2012) attributed this behavior to the predominance of nucleation effects at the channels inlet, as the flow pattern in this region is usually isolated/elongated bubbles. Figure 3.5 (a) and 3.5 (b) shows the flow boiling images obtained by Ritchey et al. (2014) for a heat sink operating under non-uniform heating dissipation and presenting transversal hotspots at its inlet and central portions, respectively. According to these figures, the boiling front is moved upstream as closer are the hotspots to the inlet region of the channels. Also, the predominance of isolated/elongated bubbles flow pattern at the channels inlet is shown in Fig. 3.5 (a).

Figure 3.5 – Illustration of the displacement of the boiling front as the transverse hotspot position moves from the middle (b) to the the channels inlet (a).

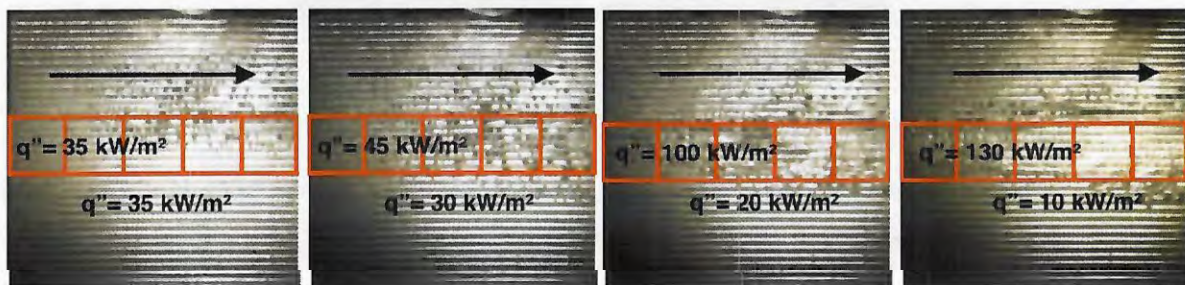


Source: Ritchey et al. (2014)

For transversal hotspots positioned at the channels outlet, Costa-Patry et al. (2012) did not observe significant changes of the Δp across the evaporator and of the local HTC at the hotspot region. Moreover, under these conditions, annular flow was present at the downstream portion of the channels. These authors attributed to the predominance of the convective effects under annular flow, the fact that the HTC is weakly dependent upon the heat flux. This also explains the low variations of local HTC with increasing heat flux for this hotspot configuration. For transversal hotspots located at the central portion of the heat sink, the region of the channels on top of the hotspot region were found to correspond to the transition between elongated/coalescing bubbles and annular flow pattern. Under this configuration, the local HTC at the hotspot region increases with increasing the local heat flux, mostly due to the predominance of nucleate boiling effects (Costa-Patry et al., 2012).

Costa-Patry et al. (2012) and Cho et al. (2010) verified as direct consequence of streamwise-oriented and local (single heater) hotspots at multichannel heat sinks, the flow maldistribution among the channels. Under this heating condition, the channels located close to the hotspot experience higher heat dissipations than the neighbor channels, leading to an increase on the vapor quality at their exit. Assuming that all channels should present almost the same pressure drop (plenums with constant and uniform absolute pressure), the mass flow rate of the channels positioned close to the hotspot position is reduced to counter balance the increase of the pressure drop gradient along these channels due to higher vapor qualities. Moreover, the reduction of the mass flow rate along the channels closer to the hotspot region is followed by an increase of the mass flow rate in the neighbor channels, keeping the total mass flow rate constant. Figure 3.6 exhibits images obtained by Ritchey et al. (2014) illustrating the aggravation of flow maldistribution as the average footprint heat flux is maintained fixed while the local heat flux of a streamwise oriented hotspot is increased. It is important to note that, for high ratios of hotspot to the footprint heat flux, the mass flow rate reduction associated to the hotspot region can be great enough to lead to critical heat flux. Thus, the authors suggested that is preferable to orient hotspots perpendicular to flow direction when possible.

Figure 3.6 – Illustration of the anticipation of boiling front as the hotspot is positioned at the channels inlet



Source: Ritchey et al. (2014)

Overall, the studies that investigated the effects of hotspot position and orientation on the overall performance of microchannels-based heat sinks (Cho et al., 2010; Costa-Patry et al., 2012; Ritchey et al., 2014) observed that the modifications of the system-level performance is closely linked to modifications of the flow pattern along the channels. Costa-Patry et al. (2012) concluded that transverse hotspots should be placed at the channels inlet for optimum cooling performance, but at an expense of increments of Δp . Also, long hotspots streamwise-oriented

should be avoided when possible, as they cause severe flow maldistribution among the channels.

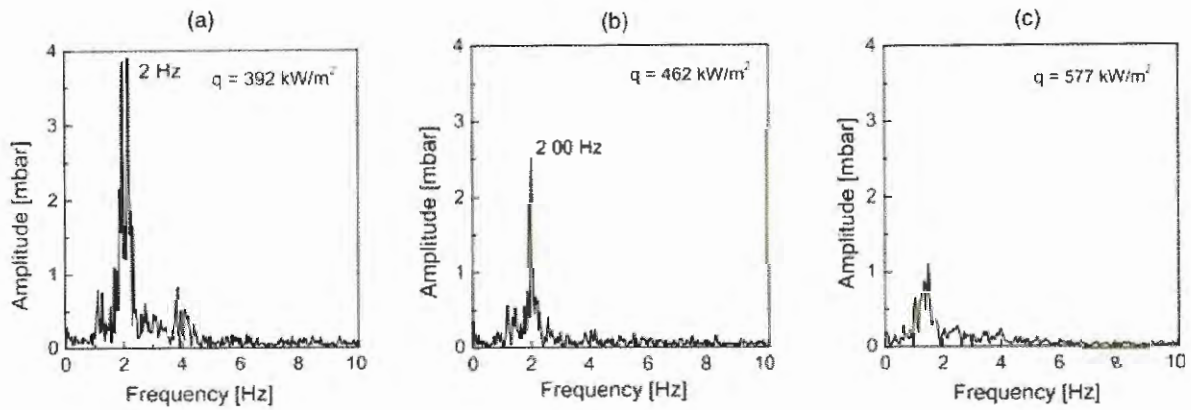
Bogojevic et al. (2011) performed an experimental evaluation of non-uniform heating effect on flow boiling instabilities in a silicon multi-microchannel. The influence of transverse hotspot position (channels inlet, middle and outlet) and hotspots severity on the flow instabilities was investigated by these authors. During single-phase flow, no variations of the temperature in the perpendicular direction of the channels were noted. However, Bogojevic et al. (2011) observed that, for increasing heat flux, the onset of boiling promptly caused non-uniform flow distribution among channels, with the presence of boiling in some channels and single-phase flow in others, leading to transverse temperature variations across the heat sink. The authors attributed this behavior to the irregularity of the number of stable bubble nucleation sites per channel, which is inherent to the random distribution of cavities size of the channels surface. Under non-uniform heating, Bogojevic et al. (2011) found that the transverse variations of temperature were less severe when the hotspot was positioned at the ending portion of the channels.

The influence of hotspot severity on flow instabilities was studied by Bogojevic et al. (2011) through an analysis of the pressure and temperature signals in the frequency domain. For this analysis, the heat flux at the hotspot was gradually increased while the background heat flux was maintained along the remaining sections. Based on the signals from pressure transducers and temperature sensors, a progressive transition from high-amplitude low frequency (HALF) to low amplitude high frequency (LAHF) fluctuations was observed for increasing heat flux at the hotspot region, independently of its position. Moreover, a cross-correlation analysis revealed that the peaks of pressure and wall temperature signals occurred concomitantly. Figure 3.7 shows the discrete Fourier transform of the differential pressure signal for increasing heat flux in the hotspot positioned at the ending portion of the channels, illustrating the transition from HALF to LAHF fluctuations.

Bogojevic et al. (2011) considered that under the HALF regime, the fluctuations of temperature and pressure signals were not driven by the growth of confined bubbles along the individual channels because synchronized peaks of temperature were observed between channels with and without boiling. Instead, the fluctuations of temperature and pressure were primarily attributed by the compressibility effects in the inlet and outlet manifolds. With further intensification of boiling and the transition to the LAHF regime, uncorrelated disturbances

developed in individual channels, suggesting that the perturbations of LAHF regime were induced by the confined growth and expansion of bubbles inside the channels.

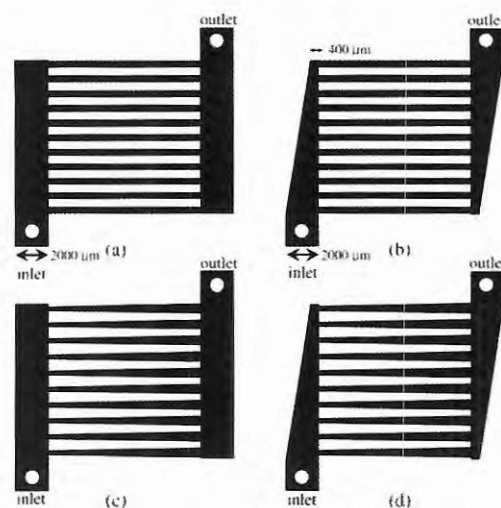
Figure 3.7 – Illustration of the differential pressure signal transition from high-amplitude low frequency to low amplitude high frequency fluctuations for increasing heat flux at the downstream hotspot region



Source: Bogojevic et al. (2011)

Cho et al. (2010) evaluated the performance of four different combinations of plenum and channel geometries for cooling transverse hotspots (upstream, central and downstream) and uniform heating for flow boiling inside microchannels. In their study, straight and diverging channels with rectangular and trapezoidal plenums were etched to silicon waffles, as shown in Fig. 3.8.

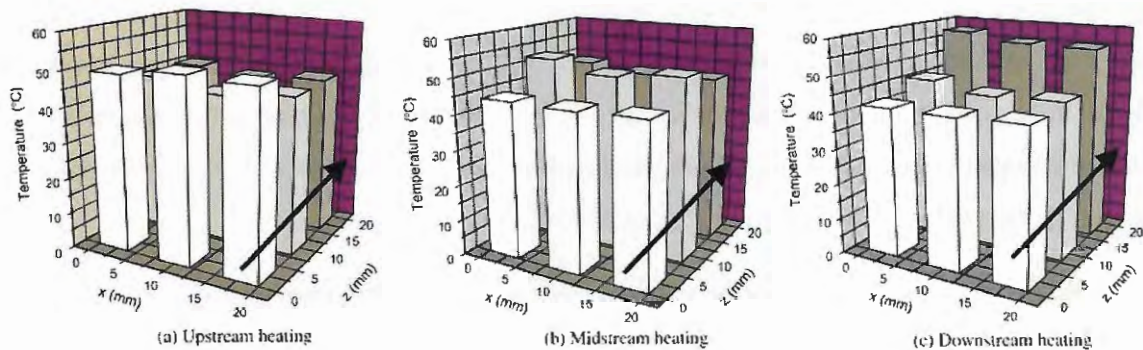
Figure 3.8 – Heat sink configurations evaluated by Cho et al. (2010) under non-uniform heating conditions



Source: Cho et al. (2010)

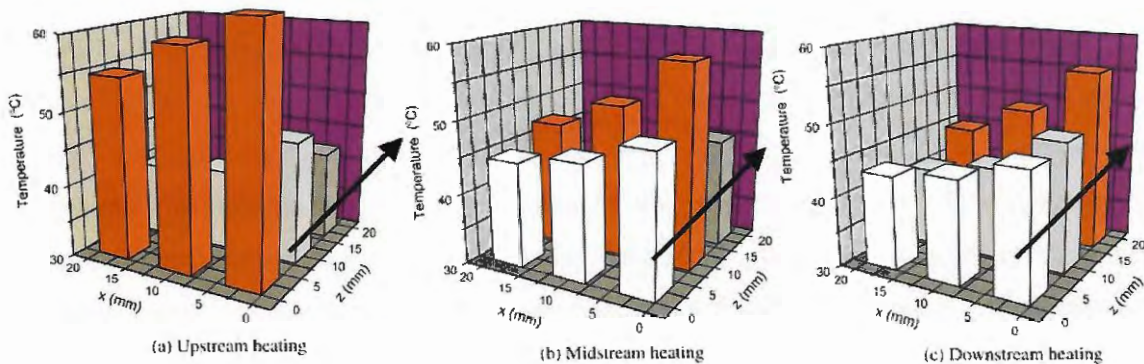
Under uniform heating conditions, the diverging microchannels heat sink with trapezoidal headers exhibited the smallest pressure drop, but the temperature uniformity was the poorest one and the maximum temperature the highest. For non-uniform heating, Cho et al. (2010) also verified that the diverging channels configuration led to the poorest temperature uniformity. Figures 3.9 and 3.10 illustrate the differences of temperature distribution across the heat sink according to the hotspot position for the configurations composed of trapezoidal headers with straight and diverging microchannels, respectively. From these figures, it is seen that the degree of uniformity of the wall temperature is higher for straight microchannels (Fig. 3.9). Moreover, Fig. 3.9 reveals that the greatest temperature peaks occur for downstream transversal hotspots. Additionally, the results of Fig. 3.9 corroborate the recommendation of Costa-Patry et al. (2012) to position transverse hotspots at the upstream portion for minimizing wall temperature differences.

Figure 3.9 – Wall temperature distribution for the heat sink with straight microchannels and trapezoidal headers according to different hotspot positions



Source: Cho et al. (2010)

Figure 3.10 – Wall temperature distribution for the heat sink with diverging microchannels and trapezoidal headers according to different hotspot positions



Source: Cho et al. (2010)

Revellin et al. (2008) developed a 1-D numerical model to predict the maximum suitable heat flux at the hotspot region without achieving critical heat flux (CHF) conditions. These authors considered that the CHF occurs when the liquid film thickness reaches a critical size for annular flow derived based on a Kelvin-Helmholtz instability analysis. These authors validated their model based on experimental data for uniform heating, and then performed a parametric analysis of the CHF considering the effects of the refrigerant type, saturation temperature, mass velocity, channel diameter, heated length, size, location and number of hotspots as well as the distance between two consecutive hotspots.

Revellin et al. (2008) concluded that, under fixed saturation temperature, R245fa is the best refrigerant for dissipating high heat fluxes without inducing CHF, followed by R134a and R236fa. Additionally, these authors indicated reductions of the maximum safe heat flux at the hotspot region as the saturation temperature increases. Increments of the mass velocity improved the maximum allowed hotspot heat flux. An increase in the number of local hotspots lowered the maximum safe heat flux on the hotspot region. For multiple hotspots configuration, the influence of a hotspot on the others decreases with increasing the distance in between the hotspots, and, as a result, the maximum allowed heat flux at hotspots increases. As expected, Revellin et al. (2008) noted that, the closer the hotspot was positioned to the microchannels inlet, the higher is the maximum allowed heat flux at the hotspot because the liquid film is much thicker at the channels inlet, a low vapor quality region.

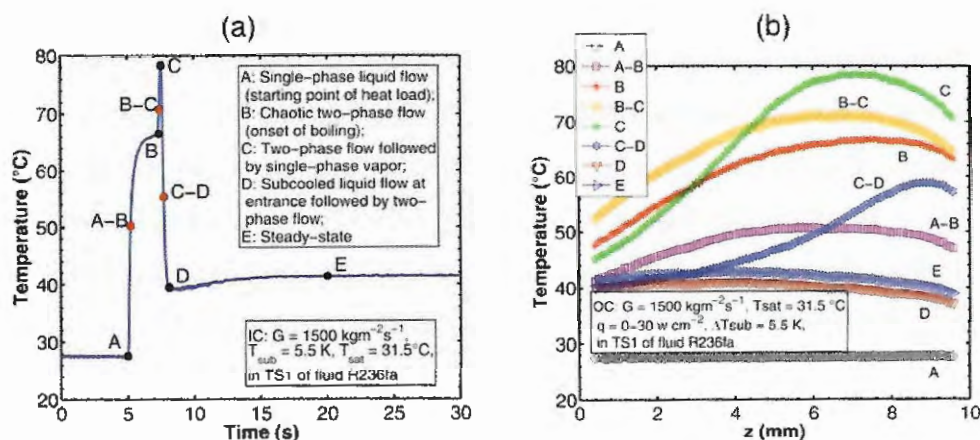
3.4. Transient Heat Loads to Flow Boiling in Microchannels

Besides the need to understand the impact of the transient heat loads at the cooling efficiency, only a few studies are devoted to this topic, as revealed by a thorough search the literature. In this section, only the studies found in literature pertinent to flow boiling under transient heat loads in microchannels are presented.

Huang et al. (2016) studied the thermal response of a multi-microchannel evaporator under conditions of cold startups (step change in the heat flux from a null power) and periodic step variations of the heat flux within two levels. These authors employed infrared thermography (1.1 ms time response and 83 μm per pixel) to measure the wall temperature variations on the evaporator footprint and a high-speed camera for flow visualization. Fig. 3.11 (a) obtained by Huang et al. (2016) shows the transient behavior of the wall temperature for a fixed position at the centerline of the heat sink where the maximum temperature occurred, and Fig. 3.11 (b) displays the corresponding evolution of the centerline wall temperature according

to the flow direction. These authors observed that the temperature variations occurring during the cold startup tests were related to a progression of different flow scenarios (A to E in Fig. 1.11). At time A, a sudden uniform heat load is imposed to the previously undisturbed liquid flow and the wall temperature rises abruptly from 28 to 67°C. At time B, the boiling process is established. From B to C, the “explosive boiling” phenomenon is present. The abrupt confined growth of bubbles caused the vapor to expand towards the channel inlet and outlet directions, pushing the liquid away to the plenums and yielding to further increments of the wall temperature up to point C. As soon as the pumping power is increased by the frequency inverter controller to meet the new condition of inlet pressure and pressure drop for maintaining the initial mass velocity, the subcooled liquid flow is pushed back to the channels and the temperature drops from C to D. At point E, steady-state flow boiling is achieved.

Figure 3.11 – Temporal variations of the wall temperature for a fixed position at the heat sink centerline (a) and temperature profile along the heat sink centerline (b) during a cold startup of a silicon microchannels-based heat sink composed of 67 channels, $D_H = 0.1$ mm, R236fa, $G = 1500$ kg/m²s, $\Delta T_{sub} = 5.5^\circ\text{C}$, $T_{sat} = 31.5^\circ\text{C}$ and $q''_{max} = 300$ kW/m²



Source: Huang et al. (2016)

A parametric analysis of the maximum base temperature and the time required to trigger boiling during the cold startup tests was performed by Huang et al. (2016). These authors found that reducing the inlet orifice width, heat flux magnitude, inlet subcooling and outlet saturation temperature but increasing the mass velocity decreased the maximum base temperature occurring during cold startups. On the other hand, the time required to trigger boiling increased with increasing the inlet orifice width, inlet subcooling, mass velocity and outlet saturation temperature but decreased with the heat flux magnitude.

The influence of the heating pulse period (2, 4 and 8 seconds) on the thermal response of the evaporation process under uniform heat flux periodic variations from 200 to 300 kW/m² was also investigated by Huang et al. (2016). The authors did not observe significant changes of the maximum and minimum wall superheat temperature with increasing heating pulse period. Moreover, the wall temperature oscillations induced by the step changes of the heat load were damped out along the tube axial direction. At the channels inlet, single-phase and subcooled boiling prevailed while at the downstream portion, annular flow was typically present. Hence, the oscillations were damped out along the tube mostly because the establishment of annular flow along the axial direction.

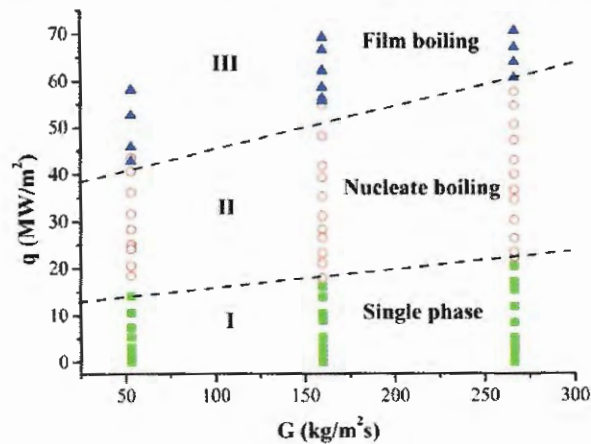
Miler et al. (2010) studied the two-phase flow response in single microchannels under square heating pulses. Their study focused on understanding the effects of pulsed heating on governing physics of bubble nucleation and expansion using a channel of 250 μm width (the channel height was not informed) etched to a silicon beam of 32 mm length. In their study, heaters and temperature sensors were micro fabricated at the bottom surface. Three independent heaters, each covering one-third of the channel length were installed, but only the microheater furthest from entrance was used to impose an average heat flux of approximately 450 kW/m². Ten temperature sensors were distributed along the microchannel. A syringe pump promoted the circulation of deionized (DI) water at a flow rate of 0.015 g/min and a high-speed camera provided flow visualizations. Square wave heating pulses of 25% duty cycle were tested at 8 Hz and 11 Hz. The heating pulses frequencies were selected as to be marginally above and below the bubble departure frequency recorded under steady heating conditions.

The results obtained by Miler et al. (2010) indicated that, for fixed time-averaged heat flux, the average wall temperature under heating pulsed at 8 Hz was 8 °C higher than steady heating. Miler et al. (2010) observed that this augmentation was caused by the matching of the heating pulses to the bubble dynamics. Under heating pulses, the higher heat flux level corresponded to the bubble incipience and the lower heat flux level to the bubble expansion and departure. Hence, the highest heat flux is applied when the heat transfer coefficient is lowest, and vice-versa. The disagreement between the high heat flux and high heat transfer coefficient periods explained the increment of average wall temperature under heating pulses when compared to steady heating.

Chen and Cheng (2009) studied the “explosive boiling” of water inside a single rectangular microchannel of $D_h = 0.215$ mm under subcooled conditions. These authors employed a platinum microheater (60 x 100 μm²) to impose heating pulses of 2 ms while the

local wall temperature was monitored through the variations of the heater electrical resistance. The bubble diameter was inferred from the images captured through a high-speed camera. Depending on the heat flux and the mass velocity, single-phase, nucleate and film boiling heat transfer were observed by the authors, as shown in Fig. 3.12. Under nucleate boiling regime, a collapse of the bubble was registered immediately after its incipience and rapid growth, followed by subsequent bubble oscillations. Chen and Cheng (2009) noted that the pressure waves induced by the quick bubble growth were reflected by the microchannel walls, thus suppressing further growth and promoting wall temperature oscillations. Under high enough heat flux, a stable vapor blanket was formed over the microheater and the temperature kept rising while the heat flux was maintained over 2 ms period.

Figure 3.12 – Flow boiling map of water under pulse heating in a microheater within a microchannel



Source : Chen and Cheng (2009)

3.5. Conclusions

A restrict but increasing number of studies was found in literature covering the outcomes of spatial and/or temporal variations of the heat load during flow boiling inside microchannels. Moreover, the pioneering studies in this field are relatively recent as they date back to the beginning of the last decade. Hence, the investigations pertinent to this topic seems to be at its earlier stages. This observation elucidates the potential of original contribution to the literature by the present study. The experimental data analysis performed in this study revealed interesting conclusions that served as the foundations for the proposal of a novel methodology for estimating wall temperature variations caused by heating pulses during flow boiling in microchannels.

The following specific conclusions were drawn from the studies analyzed in this section:

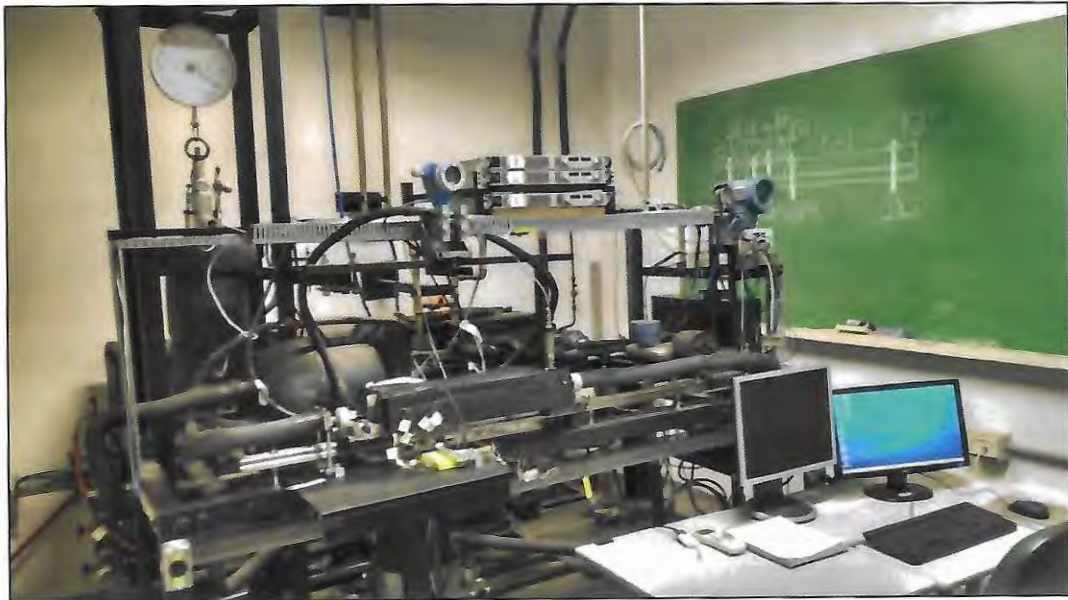
- To achieve optimal cooling performance, long hotspots should be oriented transversally to the flow direction and positioned at the channels inlet, as this increases the overall heat transfer coefficient across the heat sink and the maximum allowed hotspot heat flux without CHF occurrence. Also, long streamwise-oriented hotspots should be avoided when possible, as this would further exacerbate the flow maldistribution among the channels. Local hotspots induce flow maldistribution, hence the severity of this effect needs to be evaluated to avoid CHF occurrence in the channels experiencing lower mass flow rate;
- The flow instabilities diminish by positioning a transverse-oriented hotspot at the downstream portion of the channel. Moreover, a transition of the wall temperature and pressure fluctuations from high amplitude low frequency to low amplitude high frequency is expected under increasing heat flux at the hotspot region;
- Diverging channels are not suitable for cooling non-uniform heat loads as they exacerbate the temperature non-uniformity when compared to rectangular channels;
- Cold startup experiments in a multi-microchannels heat sink reveals a great temperature overshoot before the stabilization of flow boiling. The influence of the mass velocity, inlet orifice width, heat flux magnitude, inlet subcooling and outlet saturation temperature at the maximum temperature and the boiling delay time were identified. Step variations of uniform footprint heat flux between two levels showed that the temperature oscillations were damped out along the flow direction. Unfortunately, experiments were performed for only few conditions and the results were inconclusive. Hence, further tests are necessary to fully characterize the influence of the mass velocity and heating pulses period at the dynamics of wall superheat temperature;
- Matching the heat load dissipation with the lifecycle of a bubble during flow boiling can greatly change the average wall superheat temperature under fixed time-averaged heat flux;
- When compared to conventional channels, “explosive boiling” in microchannels is affected by the reflection of pressure waves at the channel walls, which contributes to early collapse of bubbles and great oscillations of temperature.

4. EXPERIMENTAL APPARATUS

4.1. Test Bench

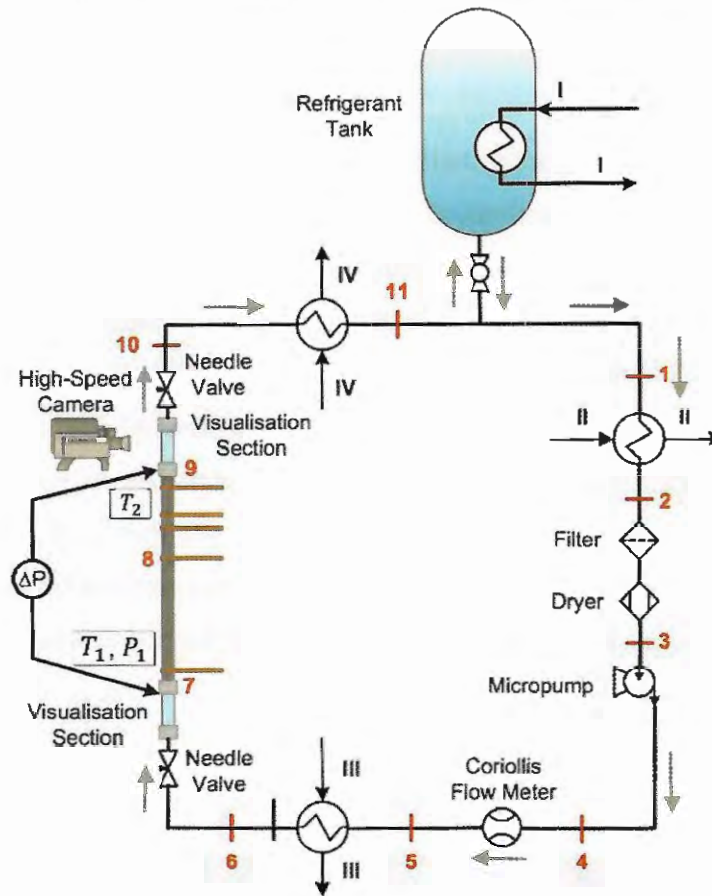
A multi-purpose test bench built in 2011 at the Heat Transfer Research Group – EESC/USP to support investigations of convective boiling inside single small diameter channels was used in the experimental campaign of the present study. Previously, the test bench has been employed successfully to investigate flow pattern (Sempértegui-Tapia, Alves and Ribatski, 2013), critical heat flux (Tibiriçá, Czelusniak and Ribatski, 2015), pressure drop and heat transfer coefficient experimental assessment for different small channels geometries (Sempértegui-Tapia and Ribatski, 2013), diameters and materials such as stainless steel and polyamide tubes (Marzoa, Ribatski and Thome, 2016). For this work, the test bench was modified to support an investigation on hotspot effects on convective flow boiling inside small diameter channels. Figure 4.1 shows a picture of the experimental test bench described in this chapter.

Figure 4.1 – Multipurpose experimental test bench located at Heat Transfer Research Group – EESC/USP (Nov/2016)



The experimental setup was composed of a main circuit containing the test fluid and an auxiliary ethylene-glycol/water circuit. The closed-loop main circuit is schematically illustrated in Fig. 4.2.

Figure 4.2 – Schematic diagram of the refrigerant circuit

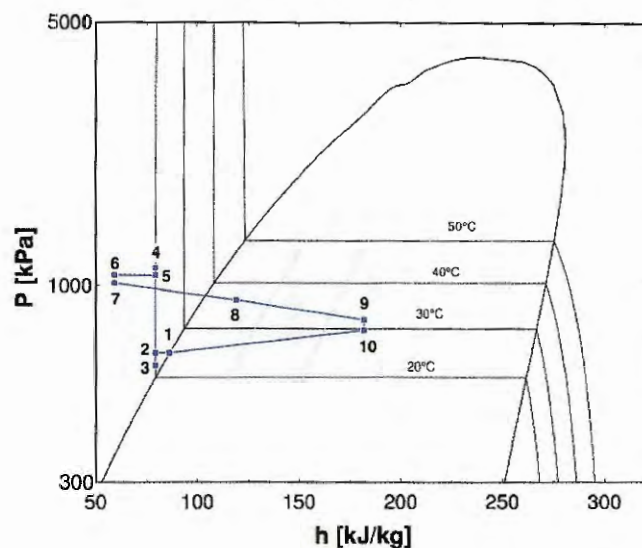


In the main circuit, a self-lubricating oil-free micropump was used to drive the refrigerant. A mass flow meter operating based on the Coriolis principle was located downstream of the micropump. The mass flow was set by a proportional-integral control system acting on a variable-frequency drive that powered the pump. An absolute pressure transducer and a thermocouple immersed within the fluid, both located at the pre-heater entry, were used to evaluate the thermodynamic state of the refrigerant at the pre-heater inlet. Needle valves placed upstream of the pre-heater and downstream of the test section were used to minimize two-phase flow oscillations due to confined bubble growth. Also, two transparent quartz tubes were installed upstream to the pre-heater and downstream to the test section. The first visualization section was used to check the presence of vapor bubbles at the pre-heater inlet, while at the second tube, flow patterns were visualized.

The operational pressure in the main circuit was set by the refrigerant tank, which contained a saturated mixture of vapor and liquid. The saturation pressure at the tank was thermally regulated by a serpentine coil placed inside the tank, which was fed with fluid from reservoir II. Figure 4.3 illustrates the thermodynamic states of refrigerant along the main circuit

in a pressure vs. enthalpy diagram. A supply line connected the bottom of the tank to the closed-loop circuit. From the supply line, the refrigerant flowed through a heat exchanger, where it is subcooled (1→2), and then through a filter/dryer (2→3) located downstream to the micropump. At the micropump, the pressure was raised (3→4) and then the refrigerant flowed through the Coriolis mass flow meter (4→5). A second heat exchanger, located downstream of the mass flow meter, was used to subcool the fluid (5→6) and ensure that no vapor bubbles were present at the preheater inlet. A needle valve, placed upstream of pre-heater inlet, imposed a local pressure drop (6→7) to reduce the propagation of fluid instabilities from the heated sections to the remaining circuit and vice-versa.

Figure 4.3 – Pressure vs. enthalpy diagram of the refrigerant thermodynamic states along the main circuit (R134a)



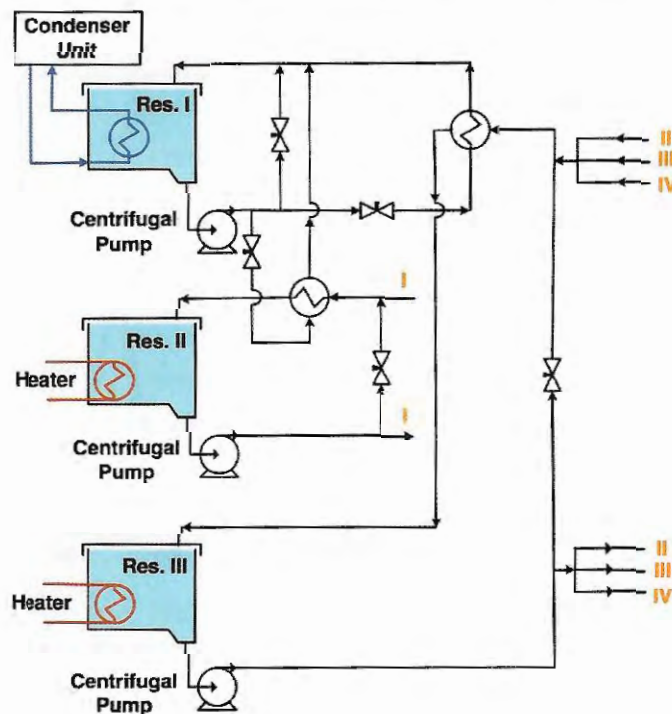
Downstream of the needle valve, a visualization section allowed to check the presence of vapor bubbles at the pre-heater inlet. Just upstream of the pre-heater inlet, the subcooled liquid enthalpy was estimated from its temperature T_1 , evaluated through a 76 μm type K thermocouple immersed within the fluid, and its pressure p_1 , evaluated through an absolute pressure transducer. In the pre-heater, the fluid was heated up to the desired condition at the test section inlet through Joule effect (7→8) by applying direct current (DC) across the tube walls. The heating effect at the test section was also obtained through Joule effect (8→9). Once the refrigerant left the test section, its temperature T_2 was determined from a 76 μm Type K thermocouple in direct contact with the fluid. The absolute pressure at the exit was estimated based on the absolute pressure at the pre-heater inlet p_1 and the pressure drop Δp , measured by a differential pressure transducer. A second visualization section, placed downstream of test section exit, allows visual inspection of the flow patterns. Again, a needle valve was installed

downstream of the visualization section to reduce instability propagation (10). A tube-in-tube heat exchanger was used to condense and subcool all the vapor generated at the heated sections (10→11). The refrigerant state at the condenser exit (11) coincides with the refrigerant state at refrigerant tank exit (1) when the closed-loop circuit operates under steady-state.

4.1.1. Auxiliary Circuit

The auxiliary circuit shown in Fig. 4.4 was used to control the saturation pressure in the main circuit refrigerant tank (I), to subcool the refrigerant entering the micropump (II) and the pre-heater (III) and to condense and subcool the test fluid in the condenser (IV).

Figure 4.4 – Schematic diagram of the auxiliary circuit



A centrifugal pump circulated an anti-freezing solution of 60% ethylene-glycol/water in the auxiliary circuit, which was composed of electrical heaters controlled by PID modules, three reservoirs, two heat exchangers and a vapor compression refrigeration system operating with R404a. The vapor compression refrigeration system was used to cool the solution in the reservoir I. In reservoirs II and III, the desire temperature was adjusted by either cooling and heating the fluid according to the experimental requirements. If reservoir temperatures lower than ambient temperature were required, then the solution from reservoir I was circulated through the two heat exchangers shown in Fig. 4.4 to cool the ethylene-glycol/water solution of the reservoirs II and III. The rate of heat exchange between reservoirs II and III and reservoir

I was regulated by controlling the mass flow rate of coolant solution from reservoir I through manually manipulating the respective needle valves. If reservoir temperatures higher than the ambient temperature were demanded, electrical resistances controlled by PID modules were used to heat the fluid contained in the reservoirs II and III. Centrifugal pumps promoted the circulation of the anti-freezing solution of the reservoirs.

4.1.2. Pre-heater and Test Section

The pre-heater and the test section were 355 and 90 mm long, respectively, and formed by a 495 mm straight horizontal stainless steel (AISI-316L) single channel. Tubes with internal diameters of 0.5 and 1.1 mm and outer diameters of 0.7 and 1.3 mm, respectively, were employed during the experimental investigations. Both tubes were manufactured by Unimed®, a Swiss-based company. Figure 4.5 illustrates a schematic diagram of the pre-heater and test section. The test section was composed of a single tube containing a 10 mm long hot spot section, which was located in between two 40 mm long tube segments, as shown in Fig. 4.6.

Figure 4.5 – Schematic diagram of the pre-heater and test section (Dimensions in mm)

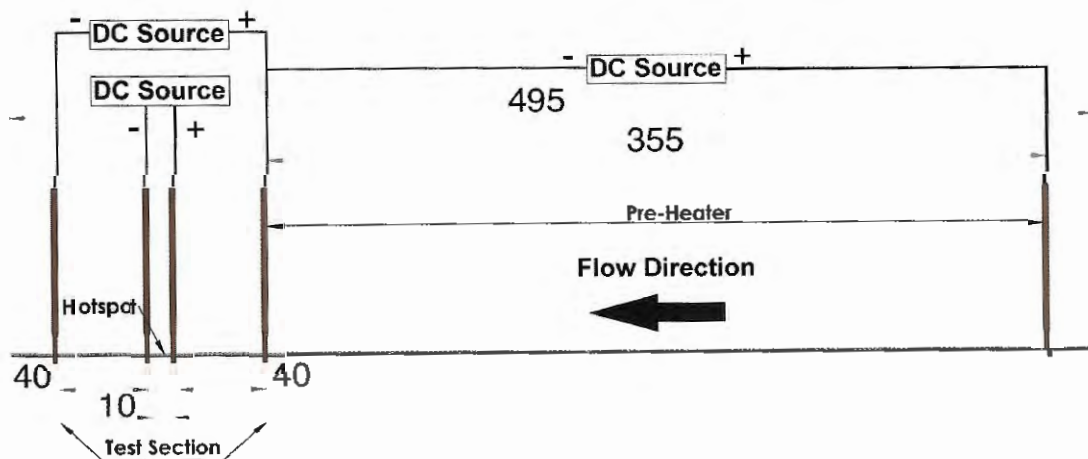
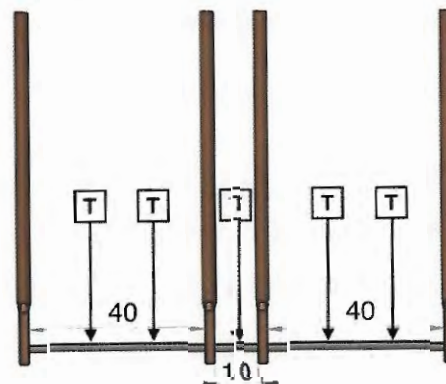


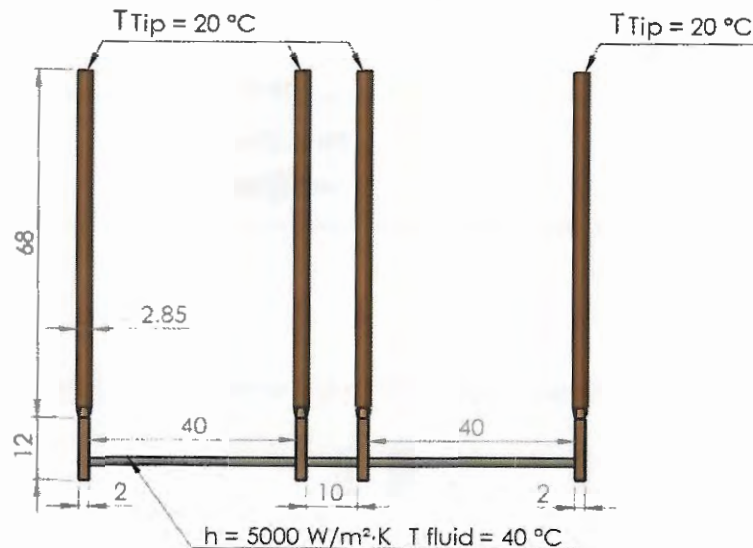
Figure 4.6 – Schematic diagram of the test section (Dimensions in mm)



The heating effect along the tube was obtained through Joule effect by directly powering its surface through copper electrodes. One DC power source powered the pre-heater, while two DC power sources supplied electrical current to the test section. As shown in Fig. 4.5, one of them was connected to the external terminals and powered uniformly all the test section length. The second one powered only the hot spot, delivering extra heat to this region. The DC source powering the hot spot was controlled analogically and was able of delivering sinusoidal, saw tooth and square power waves by means of a LabVIEW script acting as a function generator.

The copper electrodes soldered to the tube external walls behave like fins, disturbing the temperature field near their proximities. Therefore, to avoid measurement errors due to fin influence, the surface temperature measurement locations along the test section were chosen based on a tridimensional steady-state solid heat conduction simulation performed with Ansys®. The computational tool was used to determine the size of the zone affected by the presence of electrodes and ensure that the thermocouples were fixed far enough from the disturbed zone. Figure 4.7 shows the simulated geometry.

Figure 4.7 – Simulated geometry and boundary conditions adopted for the evaluation of fin effect in the test section due to copper electrodes presence (Dimensions in mm)



In this analysis, the following boundary conditions were adopted: (i) uniform internal heat transfer coefficient of 5 kW/m² and fluid bulk temperature of 40°C, (ii) uniform volumetric heat generation within the tube walls providing a heat flux of 100 kW/m² referred to the tube internal surface, (iii) copper electrodes and tube with adiabatic external surfaces, (iv) perfect thermal contact between electrodes and the tube and (v) temperature of 20°C at the copper

electrodes tips. A thermal conductivity of 401 W/mK was adopted for the copper and 16.2 W/mK for the stainless steel. Figure 4.8 illustrates an isometric view of the 3D temperature field of the test section according to the simulated condition. A convergence and mesh independence analysis was performed and the accuracy of the results were guaranteed.

Figure 4.8 – Illustration of the fin effect of the soldered copper electrodes on the test section temperature field

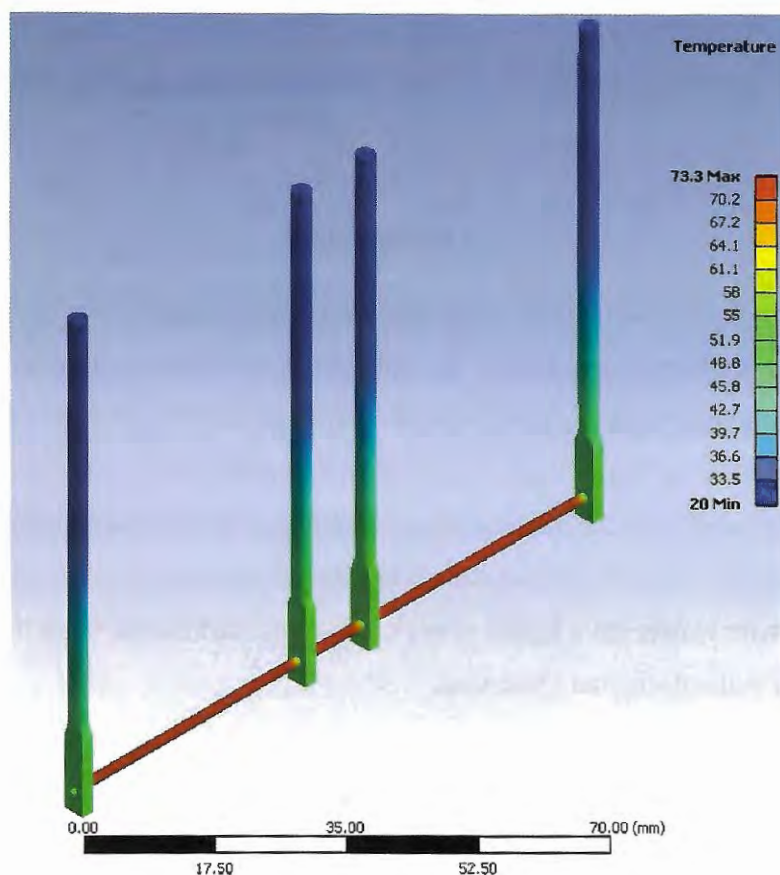
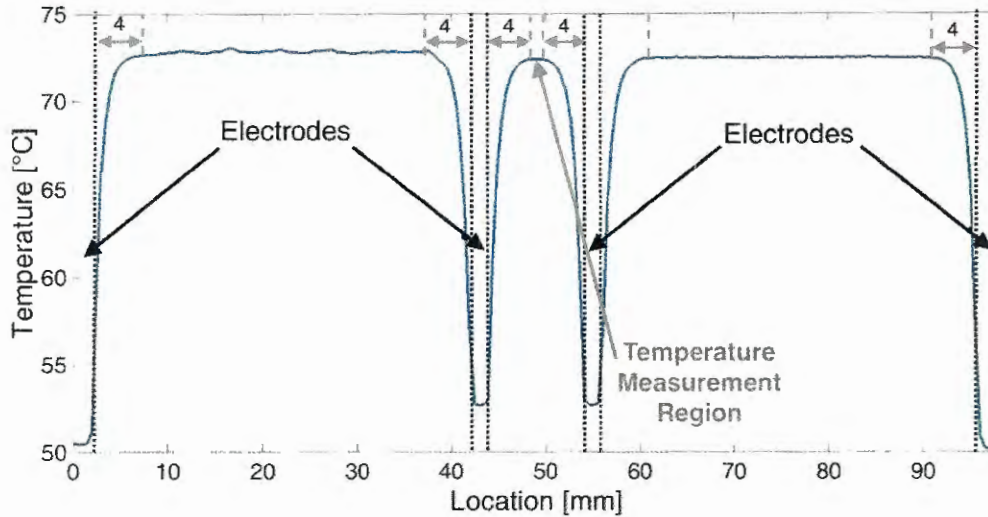


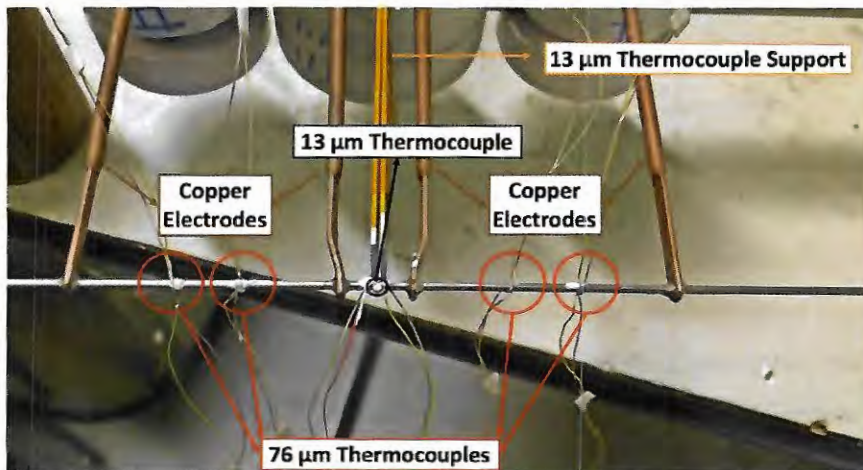
Figure 4.9 shows the numerical results for the external wall temperature profile along the longitudinal direction of the tube. From this figure, it is possible to verify severe temperature gradients in the region near to the electrodes. Based on this result, it can be concluded that the transition length between disturbed and undisturbed temperature field regions is equal to 4 mm apart from the electrodes. Therefore, to ensure appropriate temperature measurements, a minimum distance of 5 mm from electrodes was adopted for the whole test section. It is worth mentioning that, ideally, the hotspot should be as short as possible, but unfortunately the fin effect limits its minimum value to 10 mm length.

Figure 4.9 – External wall temperature profile along the test section



A type K thermocouple composed of wires with diameter of $13\ \mu\text{m}$ was used for transient temperature measurements at the hot spot section. For the remaining sections, four pairs of type K thermocouples made of wires with diameters of $76\ \mu\text{m}$ were placed 15 mm apart from the electrodes. A thermal adhesive made of alumina oxide and boron nitride (Arctic Alumina™) was used to fix the thermocouples, improving the thermal contact and keeping their electrical insulation. To minimize heat losses to the environment, the pre-heater and test section were covered with consecutive layers of rock wool and elastomeric foam. Figure 4.10 shows the test section without thermal insulation.

Figure 4.10 – Test section assembly without thermal insulation.



4.1.3. Instrumentation and Apparatus

In this section, detailed descriptions of the main components of the test bench such as sensors, actuators and data acquisition system are presented.

Micropump and Variable-Frequency Drive

A magnetic drive gear pump manufactured by Micropump® model GA-V21J8KS4 was employed to drive the refrigerant in the main circuit. The pump was controlled by varying the electric motor input frequency with a variable-frequency drive (VFD) from ABB® model ACS150 of 0.5 HP/ 220V. Table 4.1 summarizes the main characteristics of the micropump.

Table 4.1 – Micropump operational parameters

Maximum ΔP	880 kPa
Maximum Rotation Speed	6000 rpm
Maximum Volumetric Flow Rate	2.52 L/h
Maximum Temperature	260°C
Average Efficiency	61.9%
Maximum Fluid Viscosity	2.5 kg/m.s

Refrigerant Tank

A refrigerant tank with an internal volume of approximately 0.01 m³ was used. The tank was supported by a dynamometer, allowing the evaluation of the refrigerant inventory. The dynamometer presented a full scale of 20 kgf and scale divisions of 0.1 kgf.

Mass Flow Meter

A mass flow meter operating according to the Coriollis principle was placed downstream of the micropump to assure subcooled conditions and, therefore, to avoid bubbles presence due to eventual cavitation inside the meter. The mass flow meter used in the test bench is manufactured by Emerson® model Micro Motion 2700, covering mass flow rates from 0 to 84 kg/h with an associate absolute error of 0.1% of full scale (± 0.084 kg/h). The meter output signal was an electrical current ranging from 4-20 mA, linearly proportional to the measurement range of the sensor.

DC Power Sources and Waveform Generator

Three DC power sources manufactured by Lambda/Genesys® model GEN 20-38 with maximum power of 760W/220V were employed to supply electrical current to the pre-heater and test section. The DC sources are able to deliver electric potential difference from 0 to 20V and electrical currents up to 38A. All DC sources contain remote sensing to compensate voltage

drop at the power leads. The DC sources connected to the pre-heater and background communicates to the computer through a RS-485 digital interface.

Analog communication (I/O) was adopted in the hotspot DC source because the jitter of digital communication was nonviable. A waveform generator was implemented in Lab VIEW and the generated signal was sent from the DAQ system analog output port to the 0–5V electrical current input port of the DC source. The range of DC source electrical current (0–38A) was linearly proportional to the signal input range (0–5V). In the Lab VIEW interface, the heat flux waveforms (square, saw tooth and sinusoidal waves) and its average and half amplitude were set.

Pressure Transducers

Two piezoresistive absolute pressure transducers manufactured by Endress Hauser® model PMP 131 were employed to the pressure measurements at the pre-heater inlet and refrigerant tank. Both pressure transducers have a full scale of 1 MPa and maximum error of 0.5% of full scale (5 kPa). A piezoresistive differential pressure transducer with pressure taps located at the pre-heater inlet and test-section exit was used to determine the pressure drop across the small diameter channel full length. The ceramic differential pressure transducer was manufactured by Endress Hauser® model Deltabar S with a full range of 0-300 kPa and maximum error of 0.075% of the full scale (225 Pa). The output signal of the absolute and differential pressure transducers was an electrical current ranging from 4 to 20 mA.

Thermocouples

For the pre-heater and test-section, type K thermocouples (chromel/alumel) which wires were manufactured by Omega® were employed for fluid and surface temperature measurements. All thermocouples employed to the surface temperature measurements were fixed by a thermal adhesive made of alumina oxide and boron nitride (Arctic Alumina™). Before fixing the thermocouple beads to the tube wall, a thin layer of thermal adhesive was applied to the measurement region to provide electrical insulation from the DC sources and lower contact thermal resistance. The thermocouple beads were tensioned against the tube wall during the cure time of the thermal adhesive to guarantee a good thermal contact.

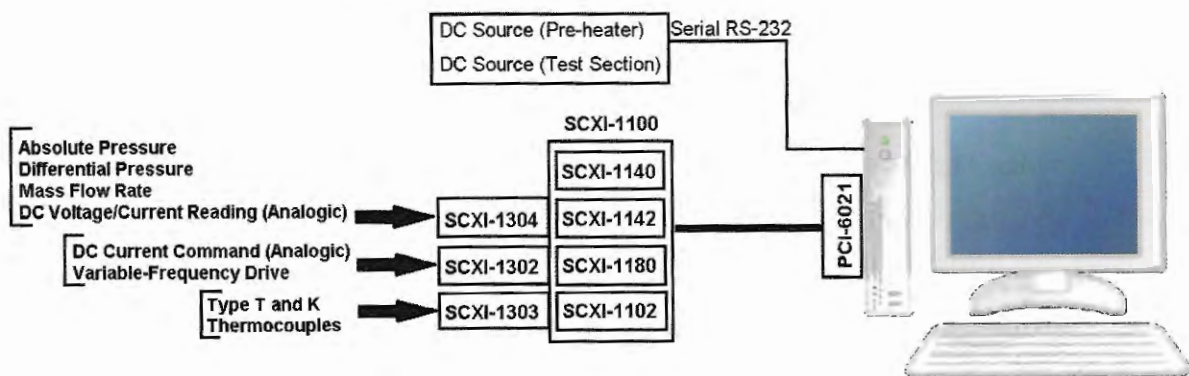
Thermocouples of 76 μm wire diameter within the tube were used to measure fluid temperature at the pre-heater inlet and test section exit. For outer tube wall temperature measurements other than the hotspot region, thermocouples of 76 μm wire diameter were used.

In the hotspot region, a thermocouple of 13 μ m wire diameter was placed in the middle of the section as shown in Fig. 4.10. All thermocouples were connected to extension cables made of the same material and with wire diameters 254 μ m through type K connectors, both manufactured by Omega®. Type T thermocouples of 1 mm wire diameter were placed in the reservoirs I, II and III for temperature monitoring.

Data Acquisition System and Test Bench Control

The SCXI-1100 module, manufactured by National Instruments®, was employed as the data acquisition and control system in the test bench. A multifunction PCI-6221 acquisition board was connected to the computer through a 32-bit PCI slot. The SCXI-1100 bundle was composed of the following signal conditioners: SCXI-1140 (8-channel simultaneous-sampling differential amplifier module), SCXI-1142 (8-channel low-pass Bessel filter module), SCXI-1180 (direct connection with terminals) and SCXI-1102 (32-channel thermocouple/voltage input module). The SCXI-1142 module was connected in cascade with SCXI-1140 for signal noise filtering. Terminal blocks SCXI-1302, SCXI-1303 and SCXI-1304 were connected to signal conditioners according to the scheme shown in Fig 4.11.

Figure 4.11 – Schematic diagram of data acquisition system components interconnections



Shunt resistors with thermal precision of $249\Omega \pm 0.1\%/^{\circ}\text{C}$ were used to convert electrical current to voltage drop measurements for the transducers whose output signal was an electrical current. A LabVIEW procedure, designed to serve as the interface between the user and data acquisition system, was used to monitor, control and record the experimental conditions during the tests. Figure 4.12 shows the front panel of LabVIEW code developed for this work. Table 4.2 summarizes the main specifications and associated errors of all sensors and actuators employed in the test bench.

Figure 4.12 – Front panel of LabVIEW interface

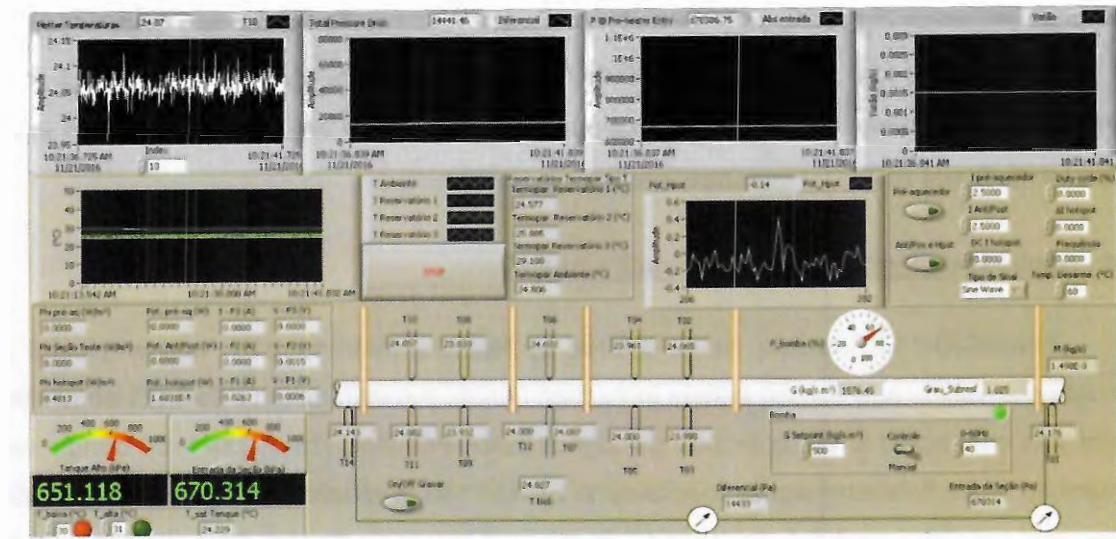


Table 4.2 – Main specification and associated errors of the sensors and actuators installed in the test bench

Sensor/Actuator	Operational and Measurement Ranges	Associated Error
Absolute Pressure Transducer (Sensor)	0 – 1000 kPa	0.5% of full scale
Differential Pressure Transducer (Sensor)	0 – 300 kPa	0.075% of full scale
Mass Flow Meter (Sensor)	0 – 84 kg/h	0.1% of full scale
DC Power Sources (Sensor/Actuator)	$V_{max} = 20 \text{ V}$, $I_{max} = 38 \text{ A}$	0.015% of full scale
Frequency Inverter (Actuator)	0.5 to 5 HP	–
Pump (Actuator)	$\Delta p_{max} = 880 \text{ kPa}$, $\dot{m}_{max} = 2.52 \text{ L/h}$	–

5. EXPERIMENTAL PROCEDURE AND DATA REDUCTION

5.1. Introduction

In this chapter, the procedures adopted for the tests during the experimental campaign and the data regression analysis are described. An analytical expression for estimating the heat losses during the tests was derived based on the data from diabatic single-phase experiments. Then, the heat losses expression was employed for determining the heat flux profile along the pre-heater and test section.

In the data regression procedure, the conservation of momentum and energy equations were discretized and solved for every time instant according to an upwind scheme considering quasi-steady flow. The vapor quality and fluid temperature profiles were derived from the local pressure and enthalpy. A discussion of the experimental uncertainties and the validation of the experimental apparatus and data regression analysis is also presented at the end of this chapter.

5.2. Energy Balance and Heat Losses Estimation

In this section, the experimental procedure performed to evaluate the heat losses from the heated sections is detailed. An analytic expression for estimating heat losses is derived from the experimental data. Also, the method adopted for estimating the heat losses during flow boiling tests is presented.

5.2.1. Heat Losses Evaluation

Diabatic single-phase experiments under uniform heating along the at preheater and test section were performed to estimate the heat losses to the environment. The range of tested experimental conditions for single-phase flow is shown in Tab. 5.1. The test conditions were carefully set to provide outer wall temperatures close to those occurring during flow boiling experiments. The room temperature was kept almost constant during the experiments (21 to 23°C). The relative heat losses to the environment (σ) for each test were estimated as the total power provided by the pre-heater (\dot{P}_{pre}) and test-section (\dot{P}_{bg}) DC sources minus the rate of fluid sensible heat variation, as follows:

$$\sigma = \frac{(\dot{P}_{pre} + \dot{P}_{bg}) - [(\pi D_{int}^2)/4]G(h_{out} - h_{in})}{\dot{P}_{pre} + \dot{P}_{bg}} \quad (5.1)$$

where h_{in} and h_{out} are the fluid enthalpy estimated at the pre-heater inlet and test section outlet, respectively, based on the corresponding local temperature and pressure measurements.

To support the development of a correlation for the relative heat losses, the average Nusselt number over the heated length (\overline{Nu}) was estimated for each test based on the method of Gnielinski (1976) considering fluid average temperature and pressure. The average fluid temperature is taken as the arithmetic average between inlet and outlet temperatures and the average pressure is calculated as the mean value between inlet and outlet local pressures. The range of average Nusselt number and relative heat losses is presented in Tab. 5.1 for the two tube diameters evaluated in the present study.

Table 5.1 – Range of experimental conditions and main results of the diabatic single-phase tests for estimating the relative heat losses to the environment

	D = 0.5 mm	D = 1.1 mm
Reynolds Number	2500 to 10000	4000 to 14500
Uniform Heat Flux	3 to 19 kW/m ²	8 to 28 kW/m ²
Average Nusselt Number	10 to 60	20 to 80
Relative Heat Losses	13 to 40%	8 to 28%
Number of Data Points	27	18

5.2.2. Analytical Expressions for the Heat Losses

The relative heat losses were correlated as functions of the average internal Nusselt number according to a power law relationship $\sigma = a \overline{Nu}_D^{-b}$, where the coefficients a and b were determined through the least squares method. Figures 5.1 and 5.2 display the experimental results and the corresponding curve fits based on the analytical expressions for relative heat losses against the average Nusselt number. According to the figures, the relative heat losses are correlated reasonably well as functions of the average Nusselt number within an absolute error range of only $\pm 3\%$ and correlation coefficients higher than 85%. The analytical expressions indicate that the heat losses are inversely proportional to the average Nusselt number ($b < 0$). Therefore, low heat losses are associated to high Nusselt numbers (heat transfer coefficients).

The experimental results for the $D = 0.5$ mm tube suggests that a linear relationship between the relative heat losses and the average Nusselt number holds true. Conversely, the data for $D = 1.1$ mm signposts for a power law dependency of the relative heat losses upon the average Nusselt number. Although a linear function yields higher correlation coefficient for D

= 0.5 mm ($R^2 = 0.95$) than obtained under power law approximation ($R^2 = 0.85$), the power law was still considered because it captures the asymptotic stabilization of the heat losses as the Nusselt number is increased. Moreover, a linear approximation would eventually yield to negative heat losses under high enough Nusselt numbers, which is non-realistic.

Figure 5.1 – Relative heat losses to environment vs. average Nusselt number for the 0.5 mm internal diameter tube

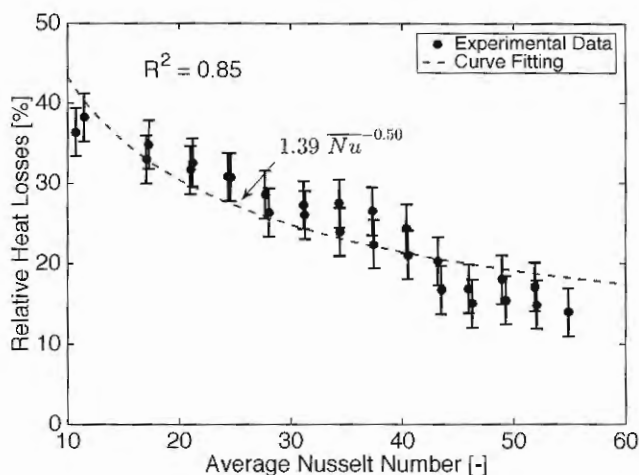
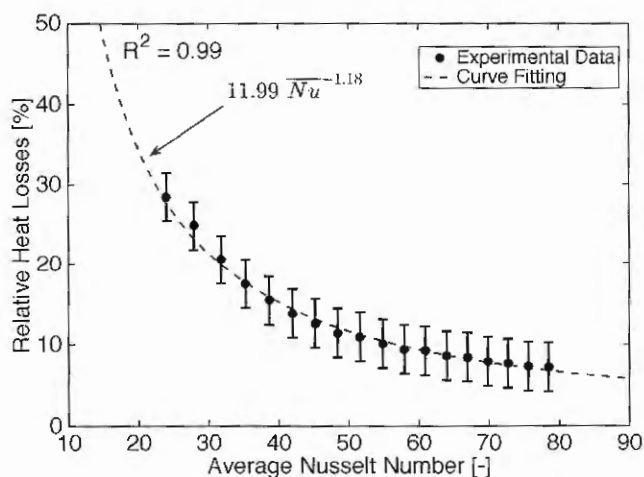


Figure 5.2 – Relative heat losses to environment vs. average heat transfer coefficient for the 1.1 mm internal diameter tube



5.2.3. Procedure for Estimating Heat Losses During Flow Boiling Tests

The heat losses along the tube were evaluated considering the local Nusselt number and based on the one-dimensional discrete model described in Section 5.3. In this evaluation, the method of Gnielinski (1976) was used for calculating the local Nusselt number for single-phase forced convection and the method of Kanizawa et al. (2016) was employed for estimating

the flow boiling heat transfer coefficient. No distinctions were made between the thermally developing and fully-developed single-phase flow regions. This simplification does not compromise the accuracy of the heat losses estimation because the entrance length corresponds to a portion of less than 15% of total heated length. The methods of Gnielinski (1976) and Kanizawa et al. (2016) were chosen because they provided the predictions of the steady-state experimental data, as shown in Section 5.5. The theoretical local Nusselt numbers along the pre-heater and test section are used to estimate the local relative heat losses according to the expressions shown in Figs. 5.1 and 5.2.

Figure 5.3 shows the Nusselt number profile along the tube during a flow boiling test based on the methods of Gnielinski (1979) and Kanizawa et al. (2016). The results indicate four different *plateaus* (dashed red line) where the heat transfer coefficient can be assumed as constant. As a consequence, the relative heat losses can also be assumed constant along each of the four *plateaus*. The lowest local heat transfer coefficient (lowest *plateau*) occurs along the single-phase flow region. The step increase in the local heat transfer coefficient along the pre-heater (second lowest *plateau*) indicates the transition from single to two-phase flow. The highest heat transfer coefficients (highest *plateau*) occurs at the hotspot, where the heat flux dissipation is maximum. Along the background region (second highest *plateau*), the average heat transfer coefficient is higher than the values displayed for the two-phase flow region along the pre-heater mainly due to higher heat flux dissipation along this region.

Figure 5.3 –Nusselt number profile along the tube axial direction during flow boiling for $D = 1.1$ mm, $T_{sat} = 31^\circ\text{C}$, $G = 600$ kg/m²s, $\Delta T_{sub} = 8^\circ\text{C}$, $q''_{pre} = 6$ kW/m², $q''_{bg} = 40$ kW/m² and $q''_{hot} = 80$ kW/m² (Heat losses included)

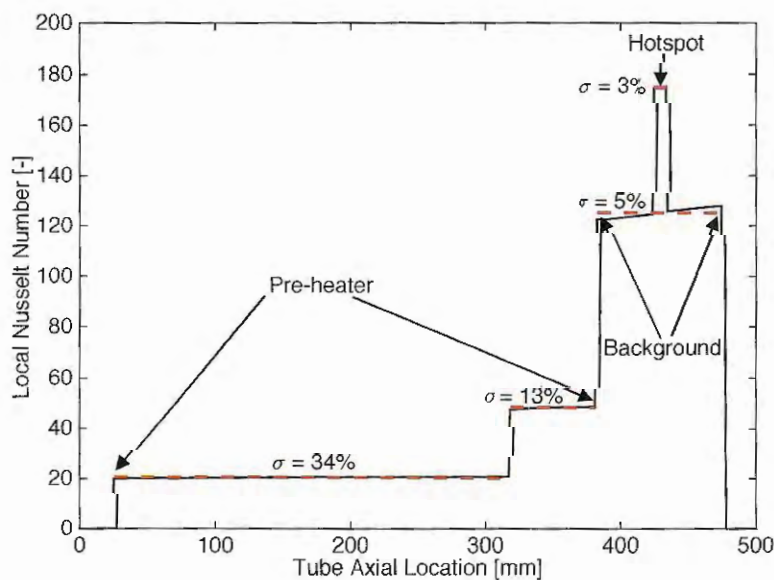


Figure 5.3 also displays the local relative heat losses for each of the four regions with uniform heat flux distribution. In this figure, great variation of the local relative heat losses among the zones (from 34% to 3%) is noted. Therefore, a non-uniform heat losses profile is assumed and the following relative heat losses coefficients are considered according to the heating zones: single-phase flow at the pre-heater ($\sigma_{1\theta-pre}$), two-phase flow at the pre-heater ($\sigma_{2\theta-pre}$), background (σ_{bg}) and hotspot (σ_{hpot}). An iterative scheme is necessary to estimate the heat losses. For the first iteration, uniform relative heat losses of 10% was assumed and the local heat transfer coefficient profile was estimated. Then, the four relative heat losses coefficients ($\sigma_{1\theta-pre}$, $\sigma_{2\theta-pre}$, σ_{bg} and σ_{hpot}) were calculated based on the average Nusselt number of the respective region. The current values are used as the initial guesses for the next iteration. Numerical convergence was assumed when the differences between the results of the current and the previous iteration was smaller than 0.1% for the four relative heat losses coefficients. The validation of the heat losses estimation procedure is shown in Section 5.5.

5.3. Data Reduction Procedure

In this section, the data reduction procedure employed for estimating the experimental transient behavior of the local heat transfer coefficient at the five different locations where thermocouples are fixed at the tube outer wall (see Fig. 4.6) is detailed. The first step consisted on importing the data gathered during the experimental campaign from a lvm file using MATLAB. Each lvm file contains the discrete time series vectors for the following parameters: mass flow rate, absolute and differential pressures, temperatures and electrical current and voltage difference.

The method described in this section assumed quasi-steady 1-D flow to model the time changes of local fluid pressure, temperature, enthalpy and thermodynamic vapor quality along the tube axial coordinate i . The tube length was divided into N_{max} discrete elements and the time domain in t_{max} discrete time steps. An upwind finite-difference scheme was adopted for solving fluid 1-D conservation of momentum and energy equations for every time instant j . The simplifying assumptions and closure relationships are presented and briefly discussed. The model was implemented in a MATLAB (2014b) code with the thermodynamic and transport properties of the fluid evaluated according to CoolProp (V4.0). The experimental validation of this model is performed in Section 5.5.

5.3.1. Presentation of the Model

For a given time instant j , the mass velocity G_j was calculated as the ratio between the instantaneous mass flow rate \dot{m}_j and the internal cross sectional area of the tube as follows:

$$G_j = \frac{4\dot{m}_j}{\pi D_{int}^2} \quad (5.2)$$

where D_{int} is the tube internal diameter.

As illustrated in Fig. 4.6, the test section was composed of a 10 mm hotspot region in between two 40 mm segments, one upstream and other downstream of the hotspot. The instantaneous electrical power delivered to the preheater \dot{P}_{pre_j} was determined from the product of measured voltage drop V_{pre_j} and electrical current I_{pre_j} , as follows:

$$\dot{P}_{pre_j} = V_{pre_j} I_{pre_j} \quad (5.3)$$

The background and hotspot DC sources are connected in parallel at hotspot region (see Fig. 4.5). In this region, the electrical currents supplied by the two DC sources I_{bg_j} and I_{hpot_j} sum up. The corresponding voltage drop is the value measured by the hotspot DC source, V_{hpot_j} . Then, the instantaneous electrical power delivered to the hotspot region \dot{P}_{hpot_j} was estimated as follows:

$$\dot{P}_{hpot_j} = V_{hpot_j} (I_{hpot_j} + I_{bg_j}) \quad (5.4)$$

In the background region of the test section, the instantaneous delivered power \dot{P}_{bg_j} was calculated as the product of the measured voltage drop V_{bg_j} and the electrical current I_{bg_j} discounted the parcel of power delivered by the background DC source to the hotspot region $V_{hpot_j} I_{bg_j}$, as follows:

$$\dot{P}_{bg_j} = V_{bg_j} I_{bg_j} - V_{hpot_j} I_{bg_j} \quad (5.5)$$

Uniform heat dissipation was assumed along heated sections. The internal superficial area was considered as the internal area of the tube comprised by the two electrodes connected to the DC source. The instantaneous heat flux at each heated region was evaluated as the ratio of the effective electrical power and the internal superficial area of the channel. The effective

electrical power was estimated by discounting the relative heat losses σ from the total power supplied to the heat sections. The relative heat losses were estimated according to the procedure described in Section 5.2.3. The instantaneous heat fluxes at the pre-heater $q''_{1\theta-pre}$ and $q''_{2\theta-pre}$, background test section q''_{bg} and hotspot q''_{hpot} were given as follow:

$$q''_{1\theta-prej} = \frac{\dot{P}_{prej}(1 - \sigma_{1\theta-pre})}{\pi D_{int} L_{pre}} \quad (5.6)$$

$$q''_{2\theta-prej} = \frac{\dot{P}_{prej}(1 - \sigma_{2\theta-pre})}{\pi D_{int} L_{pre}} \quad (5.7)$$

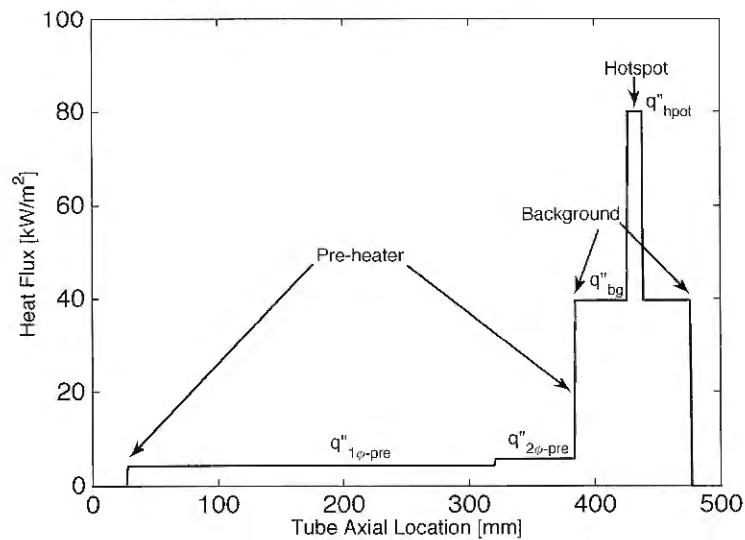
$$q''_{bgj} = \frac{\dot{P}_{bgj}(1 - \sigma_{bg})}{\pi D_{int} L_{bg}} \quad (5.8)$$

$$q''_{hpotj} = \frac{\dot{P}_{hpotj}(1 - \sigma_{hpot})}{\pi D_{int} L_{hpot}} \quad (5.9)$$

where L is the corresponding heated lengths.

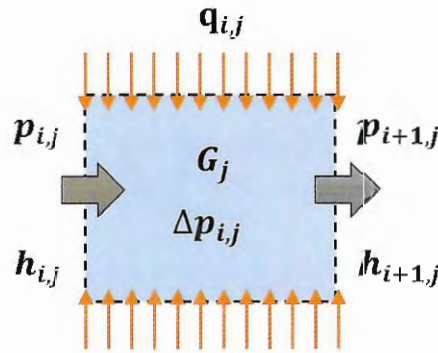
For a given time instant j , the heat flux profile along the tube axial direction i was determined based on the local heat flux (Eqs. 5.6 to 5.9) and the respective heated portion of the tube, as depicted in Fig. 5.4.

Figure 5.4 – Instantaneous heat flux profile along the tube axial direction during flow boiling tests for $D = 1.1$ mm, $T_{sat} = 31^\circ\text{C}$, $G = 600$ kg/m²s, $\Delta T_{sub} = 8^\circ\text{C}$, $q''_{pre} = 6$ kW/m², $q''_{bg} = 40$ kW/m² and $q''_{hpot} = 80$ kW/m²



After estimating the local heat flux throughout the axial direction of the tube, the instantaneous fluid properties along the small diameter channel were evaluated. Spatial variations of pressure and enthalpy were assumed across each discrete element and the local vapor quality and fluid temperature were derived from the local pressure and enthalpy based on thermodynamic state functions. A generic discrete element is schematically illustrated in Fig. 5.5.

Figure 5.5 – 1-D Fluid discrete element



The equations governing the local enthalpy and pressure variations across a control volume of Fig. 5.5 were obtained considering the following simplifying assumptions:

- One-dimensional quasi-steady flow along the axial direction;
- First order upwind finite difference discretization of pressure and enthalpy;
- Uniform heat dissipation within an element;
- Constant pressure gradient within an element;
- The pressure gradient is composed of frictional and momentum (assumed null for single-phase flow) parcels;
- Uniform length elements with $\Delta L = \text{constant}$.

For the first element ($i = 1$) at time instant j , the local pressure was given by the measurement of the absolute pressure transducer p_1 , shown in Fig. 4.2. The fluid was subcooled at the tube entry, therefore the local enthalpy for $i = 1$ was estimated from the fluid inlet pressure p_1 and temperature T_1 (see Fig. 4.2). The fluid local thermodynamic vapor quality $x_{i,j}$ of every discrete element was estimated from the fluid local pressure $p_{i,j}$ and enthalpy $h_{i,j}$ and was evaluated according to CoolProp (V4.0), as follows:

$$x_{i,j} = \text{Vapor quality } (p = p_{i,j} \text{ and } h = h_{i,j}) \quad (5.10)$$

where $x_{i,j} < 0$ for subcooled and $0 < x_{i,j} < 1$ for saturated conditions.

An energy balance across the discrete element illustrated in Fig. 5.5 provided the fluid enthalpy at its outlet $h_{i+1,j}$, as follows:

$$h_{i+1,j} = h_{i,j} + \frac{q''_{i,j} \pi D_{int} \Delta L}{\dot{m}_j} \quad (5.11)$$

where $q''_{i,j}$ is the instantaneous local heat flux and ΔL is the discrete element length.

The pressure at the control volume exit $p_{i+1,j}$ was estimated from the inlet pressure $p_{i,j}$ and the pressure drop along the element $\Delta p_{i,j}$:

$$p_{i+1,j} = p_{i,j} - \Delta p_{i,j} \quad (5.12)$$

The pressure drop across a discrete element $\Delta p_{i,j}$ was estimated by different methods depending upon the flow condition. For single-phase flow ($x_{i,j} < 0$), the pressure drop $\Delta p_{i,j}$ was calculated as shown:

$$\Delta p_{i,j} = \left[\frac{2 f G^2}{D_{int} \rho_l} \right]_{i,j} \Delta L \quad \text{when } x_{i,j} < 0 \quad (5.13)$$

where the fanning friction factor f is given according to the correlation of Churchill (1977) for smooth tubes and ρ_l is the fluid liquid density calculated based on local pressure and enthalpy at i .

For two-phase flow ($0 < x_{i,j} < 1$), the total pressure drop was estimated from the sum of the contributions of frictional and momentum parcels, as follows:

$$\Delta p_{i,j} = \Delta p_{i,j \ 2\phi\text{-}fric} + \Delta p_{i,j \ 2\phi\text{-}accel} \quad \text{when } 0 < x_{i,j} < 1 \quad (5.14)$$

The frictional pressure drop parcel $\Delta p_{i,j \ 2\phi\text{-}fric}$ was estimated according to the method of Sempertégui-Tápia and Ribatski (2017) for small diameter channels:

$$\Delta p_{i,j,2\phi-fric} = \left[F(1-x)^{1/\lambda} + \left(\frac{2 f_{lo} G^2}{D_{int} \rho_l} \right) x^\lambda \right]_{i,j} \Delta L \quad (5.15)$$

where the two constants F and λ are determined based on the local fluid conditions and the liquid friction factor f_{lo} was estimated from Churchill (1977) considering the liquid-vapor mixture as only liquid. It is worth to note that the procedure developed by Sempertégui-Tápia and Ribatski (2017) relies on experimental data that was obtained in the same test bench of the present work for the same hydraulic diameter and refrigerant, thus great accuracy was ensured.

For calculating the momentum pressure drop parcel, backward difference scheme was adopted. In this case, a forward difference scheme will require iterative calculations of the element outlet void fraction $\varepsilon_{i+1,j}$ and pressure $p_{i+1,j}$ because these parameters are related to each other. Therefore, the backward difference scheme was preferred because it leads to an explicit expression for the pressure drop due to fluid acceleration $\Delta p_{i,j,2\phi-accel}$, as shown:

$$\Delta p_{i,j,2\phi-accel} = G_j^2 \left\{ \left[\frac{(1-x)^2}{\rho_l(1-\varepsilon)} + \frac{x^2}{\rho_v \varepsilon} \right]_{i,j} - \left[\frac{(1-x)^2}{\rho_l(1-\varepsilon)} + \frac{x^2}{\rho_v \varepsilon} \right]_{i-1,j} \right\} \quad (5.16)$$

where the local void fraction $\varepsilon_{i,j}$ is null for subcooled conditions and for saturated flow, is estimated based on the method of Kanizawa and Ribatski (2016) for horizontal tubes.

During the tests, the transition from single-phase to two-phase flow occurred at the preheater. The single-phase length $L_{1\phi}$ was assumed equal to the distance between the preheater inlet and the first discrete element where $x_{i,j} > 0$. The fluid local temperature along the single-phase region was estimated from the local pressure and enthalpy, as follows:

$$T_{f,i,j} = \text{Temperature}(p = p_{i,j} \text{ and } h = h_{i,j}) \quad (5.17)$$

For the two-phase region, saturated mixture of liquid and vapor was assumed and the fluid temperature was estimated directly from the local saturation pressure:

$$T_{f,i,j} = \text{Saturation Temperature}(p = p_{i,j}) \quad (5.18)$$

The local internal wall temperature of the tube was assumed as equal to thermocouple reading (fixed at outer wall) because the Biot number was smaller than 0.1 for every tested condition. In fact, the greatest Biot number was found to be 0.06, estimated based on the lowest

average heat transfer coefficient recorded during flow boiling tests. Moreover, the 1-D radial transient conduction equation governing the heat transport across the tube walls was numerically solved using experimental data as the boundary conditions. The results from the numerical solution showed that the greatest difference between inner and outer wall temperatures were smaller than 0.08°C , hence, lower than the temperature uncertainty. Therefore, the heat diffusion time through tube walls was fast enough to allow to assume uniform temperature across the radial direction without significant errors.

Finally, the instantaneous heat transfer coefficient was estimated for the five different locations where thermocouples were fixed on the tube outer wall (see Fig. 4.6). Therefore, according to the Newton's Law of Cooling, the instantaneous heat transfer coefficient is given by:

$$\alpha_{i,j} = \frac{q''_{i,j}}{T_{tc_{i,j}} - T_{f_{i,j}}} \quad (5.19)$$

where $T_{tc_{i,j}}$ is the instantaneous reading of the corresponding thermocouple.

Figure 5.6 summarizes the data reduction procedure. The procedure starts by importing the .lvm file generated by the LabVIEW interface. The calculations proceed for the first time instant. For every time instant iteration (data acquisition rate of 25 points per second), heat losses of 10% were initially assumed. Then, the instantaneous heat flux profile was determined based on the power output of DC sources and the relative heat losses. The procedure continues by determining the pressure and enthalpy of the first discrete element. The solution proceeds by marching forward across the discrete elements and calculating respective local pressure and enthalpies according to the proper relationships. When the iteration reached the last element, the heat transfer coefficient profile was determined and new heat losses coefficients were calculated. If the difference between the initial values for heat losses coefficients and the result obtained from the current iteration was small enough, convergence was assumed and the procedure goes to the next time step. Otherwise, the heat losses coefficients for the next iteration were estimated based on the data from the current iteration. The procedure repeated itself for every time instant j until the time length chosen for analysis was reached.

After performing the procedure indicated in Fig. 5.6, the wall superheat temperature and heat transfer coefficient time-averaged values were calculated as follows:

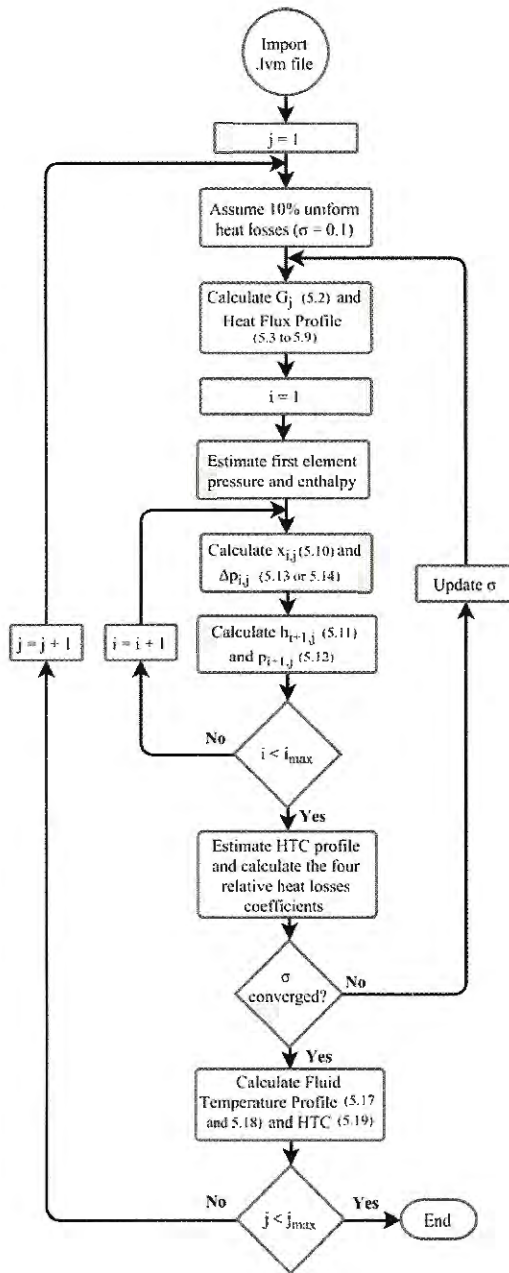
$$\overline{\Delta T_w} = \text{mean}\{\Delta T_w(t)\} \text{ for } 0 \leq t \leq t_{cycle} \quad (5.20)$$

$$\bar{\alpha} = \text{mean}\{\alpha(t)\} \text{ for } 0 \leq t \leq t_{cycle} \quad (5.21)$$

The half amplitude of the wall superheat temperature was also estimated by the following expression:

$$\Delta T_w \text{ Amp.} = \frac{1}{2} [\max\{\Delta T_w(t)\} - \min\{\Delta T_w(t)\}] \text{ for } 0 \leq t \leq t_{cycle} \quad (5.22)$$

Figure 5.6 – Algorithm for the 1-D Discrete element procedure



5.4. Experimental Uncertainties

Table 5.2 summarizes the measurement uncertainties related to the measured and estimated parameters. The measurement uncertainties associated to the absolute/differential pressure transducers, mass flow meter and DC source voltage/current readings were obtained from the datasheet provided by the manufacturer. For estimating the heated length of the pre-heater, background and hotspot regions, the distance between a given pair of electrodes was measured according to two different instruments. Because of its large length, the pre-heater was measured by a stainless-steel ruler with 1 mm divisions and total length of 500 mm. The uncertainty associated to the pre-heater heated length is assumed as the rounding error, or 0.5 mm. A digital caliper of 150 mm total length and 10 μm resolution was used for measuring the length of hotspot and background regions and its measurement error was assumed as equal to its resolution. Regarding the tube diameter, the digital caliper was used to check if the tube diameter matches the nominal specifications. The tube diameter uncertainty is assumed as the tolerance reported by the manufacturer of $\pm 20 \mu\text{m}$.

Table 5.2 – Experimental uncertainties associated with measured (left) and estimated (right) parameters

Measured Parameter	Uncertainty	Estimated Parameter	Uncertainty
D	20 μm	x	2 to 6%
L_{pre}	1 mm	G	4 to 8%
L_{hpot}	20 μm	T_f	0.22°C
p_{entry}	4.5 kPa	q''	3 to 6%
ΔP_{diff}	150 Pa	$\alpha_{2\phi}$	7 to 10%
T_{tc}	0.14 °C		
V	0.01 V		
I	0.01 A		
\dot{m}	0.1 %		

The errors associated to the temperature readings by the type K thermocouples were determined by a curve calibration procedure for a temperature range of 15 to 65°C, using a thermostatic bath and a bulb thermometer. The uncertainty related to each of the thermocouples

was estimated similarly to the procedure suggested by Abernethy and Thompson (1973) using five different curves for each temperature sensor channel. The maximum and average uncertainty of the 15 calibrated thermocouples was 0.14°C and 0.13°C , respectively. Thus, an absolute uncertainty of 0.14°C was assumed for all temperature measurements. The uncertainties associated with estimated parameters were calculated using the method proposed by Moffat (1988) and their estimatives are detailed in Appendix A.1.

5.5. Experimental Validation of the Test Apparatus and Data Reduction Procedure

In this section, the validation of the test apparatus and data reduction procedure is presented for both tube diameters ($D = 0.5\text{ mm}$ and $D = 1.1\text{ mm}$). To evaluate the accuracy of heat losses estimation procedure presented in Section 5.2.3, single-phase heat transfer experiments were performed. The experimental Nusselt numbers at the hotspot region for both test sections were compared to seven methods for predicting the Nusselt number for single-phase turbulent flow, as shown in Figs. 5.7 and 5.8. From those figures, it is seen for high Reynolds numbers that there was a reasonable agreement between the experimental results and most of the prediction methods displaying deviations within a range of $\pm 20\%$. For low Reynolds number, the experimental results agree reasonably well with the Gnielinski (1976) predictions, a well reputed method from literature. Based on this result, the data for single-phase heat transfer experiments were considered accurate enough and the heat losses estimation procedure is assumed to be valid.

Figure 5.7 – Comparison between predictions for the single-phase Nusselt according to seven methods from literature and the experimental results number of $D = 0.5\text{ mm}$ test section.

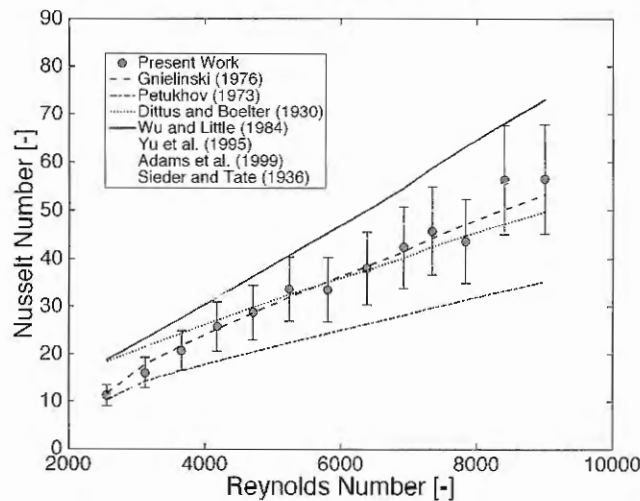
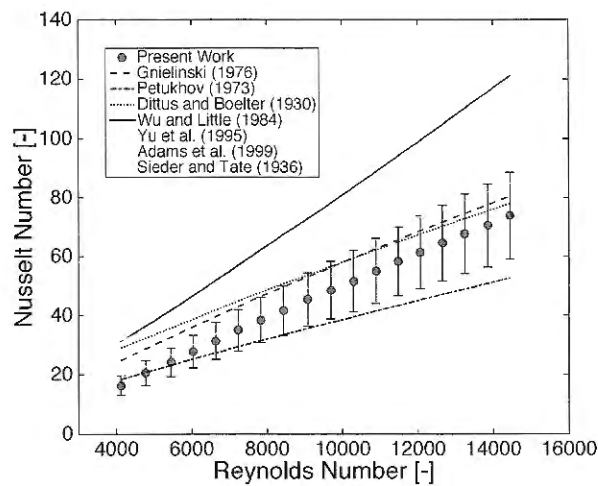
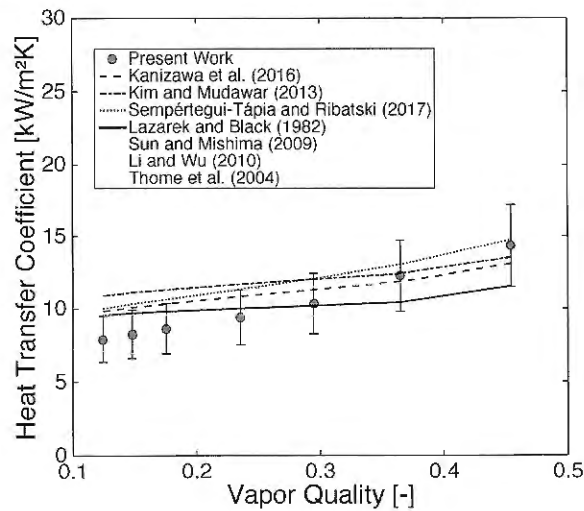


Figure 5.8 – Comparison between predictions for the single-phase Nusselt according to seven methods from literature and the experimental results number of $D = 1.1$ mm test section.



Flow boiling experiments under steady heating were also performed to ensure that the data reduction procedure described in Section 5.3 is accurate enough to estimate the experimental heat transfer coefficient not only for single-phase flow conditions. Figures 5.9 and 5.10 compare the results for the local heat transfer coefficient at the hotspot region to seven methods from literature for $D = 0.5$ mm and 1.1 mm, respectively.

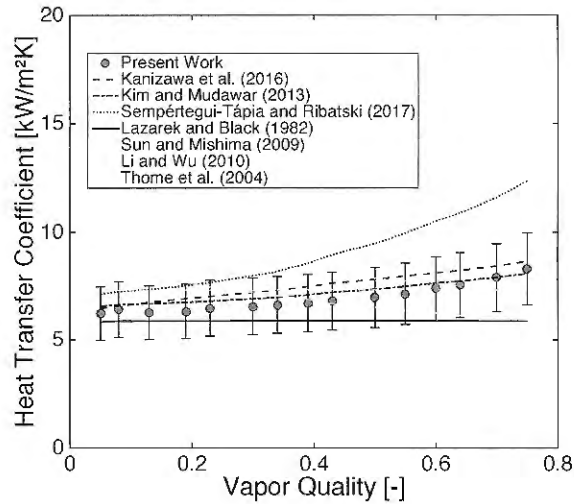
Figure 5.9 – Comparison of flow boiling heat transfer coefficient for steady-state conditions for $D = 0.5$ mm, $T_{sat} = 31^\circ\text{C}$, $G = 600$ kg/m²s and $q''_{hot} = 40$ kW/m²



Both figures indicate good agreement between the experimental data and the results provided by most of the correlations. In this comparison, it is important to emphasize that the heat transfer coefficient according to different methods can deviate in some cases more than 100%, as seen in Figs. 5.9 and 5.10 under high vapor quality conditions. Therefore, as the

experimental results of present work agrees with the majority of prediction methods within an uncertainty of $\pm 20\%$, the results were considered as satisfactory and the data reduction procedure was taken as accurate enough.

Figure 5.10 – Comparison of flow boiling heat transfer coefficient for steady-state conditions for $D = 1.1$ mm, $T_{sat} = 31^\circ\text{C}$, $G = 400$ kg/m²s and $q''_{hpot} = 25$ kW/m²



The calculation of the pressure profile across the tube requires an accurate model, as the fluid temperature profile at the saturation region was determined based on the local pressure. Inaccuracy of local pressure estimation directly translates into heat transfer coefficient errors. The validation of the pressure drop model was performed by comparing the differential pressure transducer readings with the pressure difference between the tube inlet and outlet given by the data reduction procedure summarized in Fig. 5.6. The same database presented in the results section, which contemplates flow boiling tests under transient heating, was used to verify the accuracy of the model. This database comprises 216 experimental points for each of the two tested tube diameters. It is important to note that single-phase and two-phase diabatic regions were present during the flow boiling tests, thus the validation performed here evaluates the accuracy of a combination of single-phase/two-phase friction factor and void fraction estimations.

Figures 5.11 and 5.12 display the comparison of experimental and estimated pressure drop for the entire tube length for $D = 0.5$ and $D = 1.1$ mm, respectively. These figures suggest that most of the pressure drop estimates presented an associated error within a range of ± 5 kPa. According to the Clausius-Clapeyron equation, an error of ± 5 kPa for R134a at 31°C saturation temperature translates into errors of $\pm 0.22^\circ\text{C}$ in the fluid temperature. Hence, the errors associated to saturation temperature were slightly greater than wall temperature measurements

($\pm 0.15^\circ\text{C}$). The errors of fluid pressure and temperature were considered as acceptable and the pressure drop calculation algorithm shown in Fig. 5.6 was considered to be accurate enough for the experimental conditions of this study.

Figure 5.11– Assessment of the pressure drop model accuracy for the $D = 0.5$ mm test section

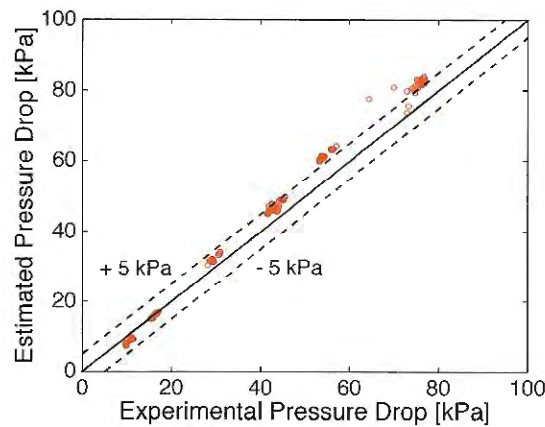
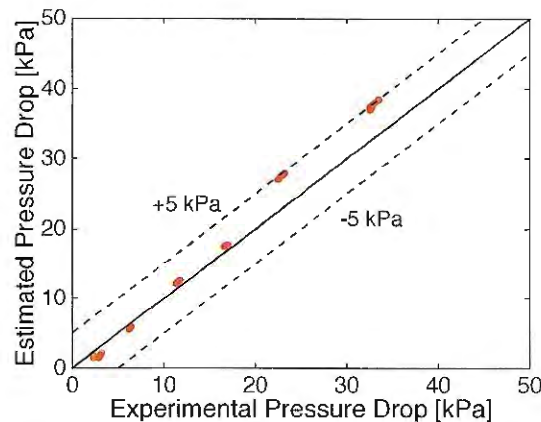


Figure 5.12 – Assessment of the pressure drop model accuracy for the $D = 1.1$ mm test section



5.6. Experimental Procedure

5.6.1. Transient Heating Flow Boiling Tests

The tests were initiated by turning on the condenser unit and the centrifugal pumps of the reservoirs I, II and III. Then, the target temperatures at reservoirs II and III were set by the PID modules which control the heating rate supplied by the cartridge electrical resistances. The anti-freezing solution from reservoir II was circulated through a serpentine coil within the refrigerant tank to exchange heat with the test fluid, establishing the desired saturation pressure in the tank and, consequently, in the main circuit. Then, the micro pump was turned on and the mass flow rate was adjusted by a proportional-integral controller actuating on the variable

frequency driver that powers the pump. Once the mass flow rate reaches steady-state, the DC sources were turned on. After this, the electrical power delivered to the pre-heater DC source was gradually adjusted until achieving the desired vapor quality at the test section inlet. Next, the two DC sources connected to the test section were set and power was supplied to the hotspot and background regions of the test section according to a pre-defined experimental condition. Data points were logged when stable conditions were verified. Transient heating tests were considered under stable condition when steady-state oscillation of hotspot wall temperature was verified. Steady-state oscillation was assumed when the average, maximum and minimum wall temperature variations were within deviations lower than 0.05°C .

5.6.2. Uniform Heating Single-Phase Flow

The single-phase experiments were initiated by turning on the micropump and by circulating subcooled liquid refrigerant through the microtube. When the mass velocity was stabilized according to the desired condition, the pre-heater DC source and the DC source connected to the external terminals of the test section were turned on and set to dissipate the same electrical current. This practice provides uniform heat flux dissipation along the length of the tube comprised by the first electrode of the pre-heater and the last electrode of the test section (see Fig. 4.5). The heat dissipation rate was set as to keep a subcooling degree of 4°C at the tube outlet in order to assure the exchange of only sensible heat. The visualization sections at the tube inlet and outlet were used to guarantee the absence of subcooled flow boiling.

In order to cover a broad interval of Reynolds and Nusselt numbers, the mass velocity and heat flux were gradually increased from the lowest to the highest tested values, always maintaining fixed the subcooling degree of 4°C at the tube outlet. For each test, the local single-phase Nusselt Number was measured at the five different locations where thermocouples were attached to the tube walls (see Fig. 4.6). Hydrodynamically and thermally fully developed flow was assumed at the test section inlet since $L/D > 300$ at this region for both tube diameters. The experimental results for the single-phase Nusselt number were presented in Section 5.5 and were used to validate the energy balance estimation procedure as described in Section 5.2.3.

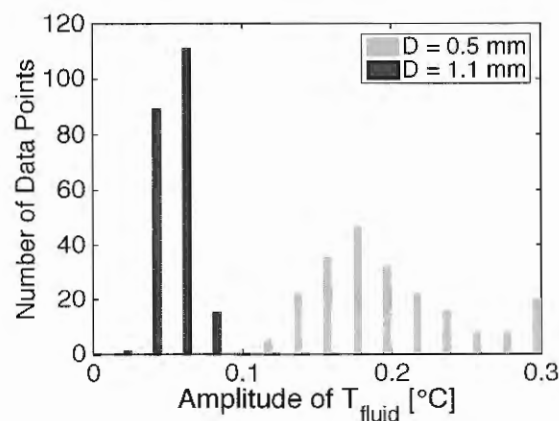
5.7. Influence of the Fluid Saturation Temperature on the Wall Superheat Temperature Dynamics

During the transient heating experiments, the pressure drop across the tube varied cyclically with the heating pulses. The variations of the heat load at the hotspot region

introduces perturbations to the tube outlet vapor quality, which implies on oscillations of the pressure gradient profile, evaluated through the cyclical variations of the pressure drop measured by the differential pressure transducer. However, the mass velocity was verified to be nearly constant and undisturbed during these tests. Hence, the variation of the tube hydraulic resistance due to the heating pulses were not high enough to affect the mass flow rate delivered by the micropump. Because the fluid is saturated at the hotspot region, variations of the fluid local pressure are associated to changes in the fluid local temperature. Therefore, it is reasonable to assess the level of fluid temperature fluctuations during the experiments, as this procedure permits to check if the fluid temperature fluctuations influence significantly on the behavior of the wall superheat temperature.

In the present analysis, the level of oscillations of the local fluid temperature at the hotspot central portion was quantified by the peak-to-peak amplitude of the local fluid temperature. The local fluid temperature of hotspot central region is obtained from reduction of the experimental data according to the procedure described in Fig. 5.6. Figure 5.13 displays the frequency distribution of the peak-to-peak fluid temperature amplitude occurring during the tests.

Figure 5.13 – Distribution of fluid temperature oscillations during transient flow boiling tests



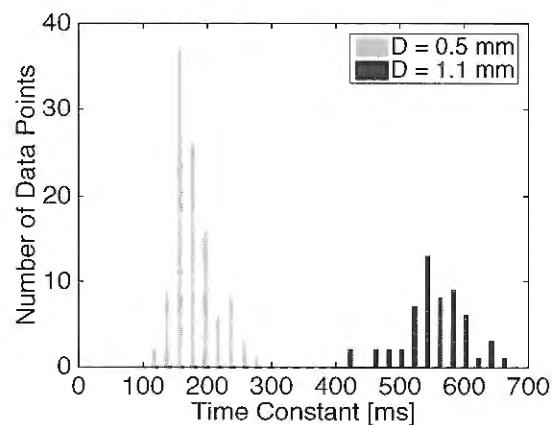
According to Fig 5.13, the fluid temperature amplitude for $D = 1.1$ mm is lower than 0.1°C while for $D = 0.5$ mm, its value is within the interval from 0.1 to 0.3°C . It is reasonable to expect greater fluid temperature fluctuations for the smallest diameter tube, as the pressure gradient monotonically increases with the reduction of the channel diameter. The peak-to-peak wall superheat temperature amplitude ranged from 1 to 4°C during the transient heating tests. Hence, the wall superheat temperature was assumed to be marginally affected by the variations of fluid temperature, independently of the tube diameter.

5.8. Characterization of the Temperature Sensor Dynamic Response

It is essential to know the thermal time constant of temperature fluctuations measurement at the central hotspot region as this parameter indicates the minimum time-scale of phenomena that the temperature sensor is able to capture. According to Bradley and Matthews (1968), thermocouples with a length to diameter ratio $L/D > 200$ present negligible axial-direction heat conduction, thus, they can be assumed as a first-order lag system. A lumped thermal capacitance model can be assumed for the tube walls; hence, its dynamics could be also represented by a first-order differential equation. Consequently, it is reasonable to consider that the association of the thermocouple bead and the tube walls can be approximated and represented by a single lumped thermal capacitance. In this case, the time constant is related to the combined effects of thermal inertia of the tube walls, thermal interface resistance between thermocouple bead and the tube, the thermal inertia of thermocouple bead and the local heat transfer coefficient.

For the present study, the time constant of a given data set was estimated using the System Identification Toolbox 9.1 from MATLAB 2014b based on the instantaneous heat flux as the input and the hotspot thermocouple readings as the output signal. The normalized root mean square error was employed as an indicator of how well the response of the model fits the data. Only results with normalized root mean square error smaller than 20% were considered, resulting in 108 and 56 data points for $D = 0.5$ and 1.1 mm, respectively. Figure 5.14 shows the frequency distribution for the estimated time constant segregated according to the tube diameter.

Figure 5.14 – Frequency distribution of estimated time constant based on experimental data for the two tested tube diameters



The results displayed in Fig. 5.14 indicate average time constants of 181 and 552 ms for $D = 0.5$ and 1.1 mm, respectively, corresponding to cut-off frequencies of 0.88 and 0.29 Hz. The lowest time constant is recorded for the smallest diameter tube. This result was expected as the characteristic length of the tube cross section is lower for the smallest tube diameter. Since the maximum cutoff frequency is close to 1 Hz, at a rough estimate, one can assume that only temperature variations lower than 10 Hz will be captured by measurement method employed in this work. In fact, some tests revealed that the temperature fluctuations reduce to a level within the measurement uncertainty (0.15°C) for frequencies higher than 6 Hz, in general. Accordingly, the heat pulses frequency was limited to 2 Hz during the flow boiling transient tests. As abovementioned, the cutoff frequency is approximately three times greater for $D = 0.5$ mm when compared to $D = 1.1$ mm. Therefore, for a given frequency of heating pulses and fixed fluid conditions, the effects of thermal inertia are more pronounced for $D = 1.1$ mm. This consideration should be taken into account when comparing the results between the two tube diameters for fixed test conditions.

It is also worth to mention that, while the order of magnitude of the temperature sensor time constant is around 100 ms, the heat transfer mechanisms during flow boiling inside the small diameter channels can have a much smaller time-scale. This can be illustrated by considering that the elongated bubble passage frequency for a 2.32 mm diameter tube is 40 bubbles per second (1 bubble every 25 ms) for R134a, $T_{sat} = 31^\circ\text{C}$, $x = 4\%$ and $G = 300 \text{ kg/m}^2\text{s}$, as experimentally observed by Arcanjo, Tibiria and Ribatski (2010). Under the same fluid conditions and constant heat flux, the temperature measurement employed in this work would not be able to capture the variations of wall temperature due to the intermittent passage of elongated bubbles and liquid pistons. Instead, the temperature signal would be nearly constant. The heat transfer mechanisms related to nucleation effects occur at even smaller time-scales. Tibiria and Ribatski (2014) based on their own experimental results proposed an expression for estimating the bubble departure diameter and frequency in microscale channels given by $f_{bubbles} = 7.07 \cdot 10^{-10} Re^2 D_h^{-2}$. According to this expression, the bubble departure frequency is 3400 Hz (1 bubble detaching every 0.3 ms) for R134a, $T_{sat} = 31^\circ\text{C}$, $G = 400 \text{ kg/m}^2\text{s}$ and $D = 0.5$ mm.

From the analysis of the time-scale order of magnitude pertinent to the temperature sensor employed in this work (100 ms) and the heat transfer mechanisms (approximately 10 ms for convective effects and 0.1ms for nucleation effects), it is clear that the characteristic time of the heat transfer mechanisms are much lower than the temperature sensor time constant.

Therefore, the temperature measurement technique employed in this work are limited to capture variations of temperature lower than 5 Hz. For temperature oscillations frequencies above 10 Hz, only the time-averaged effects of heat transfer mechanisms modifications at smaller time scales will be captured by the temperature sensor employed in this study.

6. RESULTS

6.1. Introduction

In the first part of this Chapter, the experimental matrix is presented. Then, the characteristics of the transient behavior of the HTC observed under the square, sinusoidal and saw tooth waveforms are outlined. The discussions proceed to a parametric analysis of the instantaneous behavior of the ΔT_w under transient heating conditions. The parametric analysis is performed by tracking the changes of the amplitude and the average value of ΔT_w under different fluid and heating conditions. The influences of the tube diameter, mass velocity, vapor quality, average heat flux and heat flux amplitude, its waveform and frequency on the ΔT_w amplitude and its average value are addressed. Then, the results obtained under transient heating conditions are compared with predictions based on eight methods from literature developed for steady heating. The accuracy of each prediction method is assessed and the most accurate methods are indicated. At the end of the chapter, a methodology for estimating the wall superheat temperature behavior under cyclical and transient heat loads is presented.

6.2. Experimental Database Description

Experimental results for the transient behavior of the local ΔT_w and HTC at the hotspot region were obtained for sinusoidal, square and saw tooth heat pulses. The refrigerant R134a was employed as the working fluid. The experiments were performed for 0.5 and 1.1 mm ID stainless steel tubes, mass velocities of 400 and 600 kg/m²s and saturation temperature of 31°C. The test section background heat flux was kept at 20 and 40 kW/m² during the tests for $D = 0.5$ and 1.1 mm, respectively. The duty cycle of square heating pulses was fixed at 50%. Average local vapor qualities of 8, 40 and 60% were set at the hotspot central region for time-averaged heat dissipation of 80 and 120 kW/m² and half amplitudes of 20 and 40 kW/m². Heat flux oscillation according to frequencies of 0.5, 1 and 2 Hz were evaluated. Higher frequencies were not evaluated because the combined thermal inertia of tube walls and thermocouple bead damps the fluctuations of ΔT_w to a level within the uncertainty of the temperature measurement. Table 6.1 presents the experimental matrix evaluated in the present study. Data for a total of 432 transient flow boiling conditions were obtained during the experimental campaign.

Table 6.1 – Experimental conditions evaluated in the present study

Experimental Parameter	Experimental Condition
Fluid	R134a
T_{sat}	31°C
D	0.5 and 1.1 mm
G	400 and 600 kg/m ² s
\bar{x}_{hpot}	8, 40 and 60 %
Waveform at Hotspot	Sinusoidal, Square and Saw Tooth
\bar{q}''_{hpot}	80 and 120 kW/m ²
$\Delta q''_{hpot}$ (Half Amplitude)	20 and 40 kW/m ²
Heating Pulses Frequency at Hotspot	0.5, 1 and 2 Hz

6.3. Characteristic Behavior of the Wall Superheat Temperature and the Heat Transfer Coefficient According to the Heating Pulses Waveforms

Figures 6.1 (a) and 6.1 (b) show the instantaneous heat flux, ΔT_w and the corresponding HTC for square heating pulses. According to Fig. 6.1 (a), ΔT_w rises exponentially as the heat flux is abruptly increased. Similarly, ΔT_w drops exponentially as the heat flux steeply changes from the upper to the lower level. According to Fig. 6.1 (b), the heat transfer coefficient curve presents discontinuities. Step changes of the local HTC are registered as the heat flux alternates between the two levels of the square wave. The heat transfer coefficient peaks are associated to the sudden increase of the heat flux to its upper level. This behavior is due to the combination of the maximum heat flux and the minimum wall superheat temperature. Then, as the heat flux is kept constant at the upper level, the heat transfer coefficient rapidly decreases as a result of exponential rise of wall superheat temperature. A period of constant HTC is not achieved because the heat flux is reduced to the lowest level before the stabilization of ΔT_w . As soon as the heat flux is reduced, the heat transfer coefficient reaches its minimum value. From this point, the HTC increases as the heat flux is kept constant at its lowest level and the wall superheat temperature reduces exponentially.

Figure 6.1 –Transient behavior of the wall superheat temperature (a) and heat transfer coefficient (b) for square heating pulses. R134a, $D = 1.1$ mm, $T_{sat} = 31^\circ\text{C}$, $G = 400$ kg/m²s, $\bar{x}_{hpot} = 8\%$, $\bar{q}''_{hpot} = 80$ kW/m², $\Delta q''_{hpot} = 40$ kW/m² and $f = 0.5$ Hz

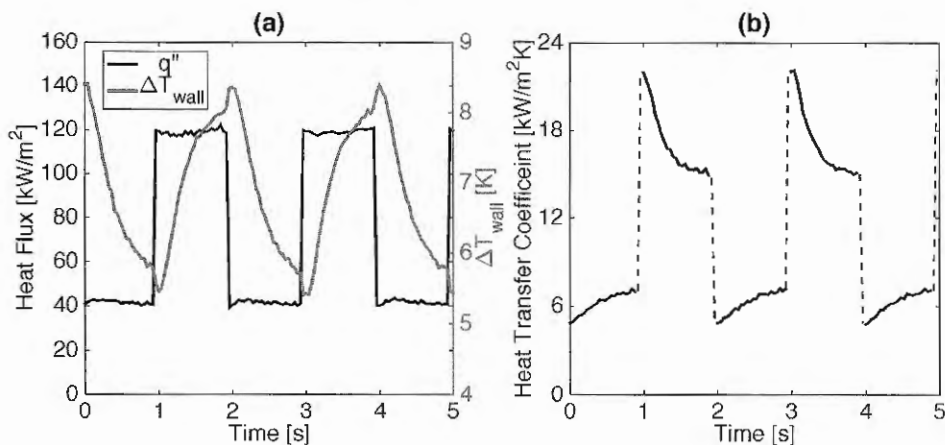


Figure 6.2 (a) shows results for the wall superheat temperature and Fig. 6.2 (b) displays the corresponding instantaneous HTC for sinusoidal heating pulses. Figure 6.2 (a) reveals a time delay between the heat flux and the wall superheat temperature. Figure 6.3 indicates the augmentation of the magnitude of the phase angle between the peaks of heat flux and wall superheat temperature as the heating pulses frequency is increased for the same experimental conditions of Fig. 6.2. Therefore, it can be concluded that the time delay shown in Fig. 6.2 (a) is associated to the thermal inertia effects of the tube wall and thermocouple bead.

Figure 6.4 shows the Fourier transform of the heat flux, ΔT_w and HTC for the conditions of Fig. 6.2. The Fourier transform of ΔT_w and heat flux revealed pure harmonic oscillations of these signals. Conversely, the Fourier transform of the heat transfer coefficient signal exposes the presence of two harmonics, a main harmonic at the same frequency of the heat flux and a second harmonic at double frequency and 7.2% of the magnitude of the main harmonic. The secondary harmonic of the heat transfer coefficient signal arises from the quotient between the heat flux and wall superheat temperature, two pure harmonic waves with a phase-shift between them. In general, the second harmonic of HTC was found to be smaller than 10% of the main harmonic. Also, the second harmonic would not be present if the temperature response of the sensor was instantaneous. Therefore, under sinusoidal heating pulses, both wall superheat temperature and HTC can be assumed as sinus waves oscillating around an average value.

Figure 6.2 –Transient behavior of the (a) wall superheat temperature and (b) HTC under sinusoidal heating pulses. R134a, $D = 1.1$ mm, $T_{sat} = 31^\circ\text{C}$, $G = 400$ kg/m²s, $\bar{x}_{hpot} = 60\%$, $\bar{q}''_{hpot} = 120$ kW/m², $\Delta q''_{hpot} = 40$ kW/m² and $f = 1$ Hz

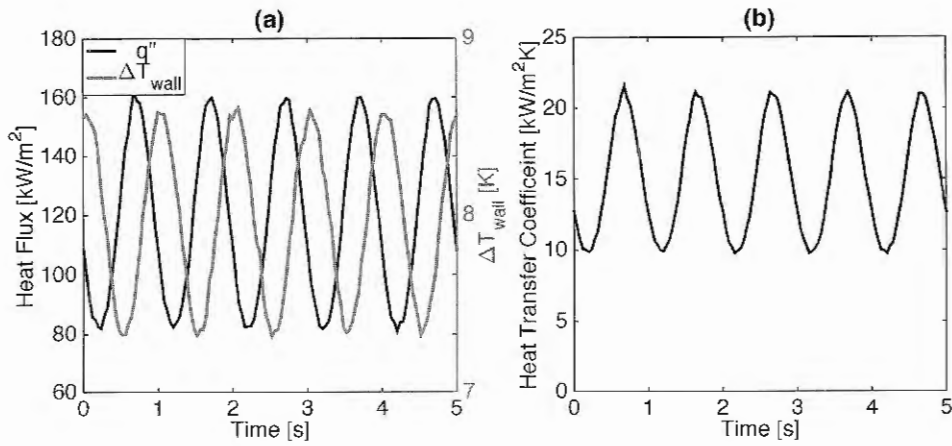


Figure 6.3 – Variation of the phase angle according to the sinusoidal heating pulses frequency. R134a, $D = 1.1$ mm, $T_{sat} = 31^\circ\text{C}$, $G = 400$ kg/m²s, $\bar{x}_{hpot} = 60\%$, $\bar{q}''_{hpot} = 120$ kW/m², $\Delta q''_{hpot} = 40$ kW/m² and $f = 1$ Hz

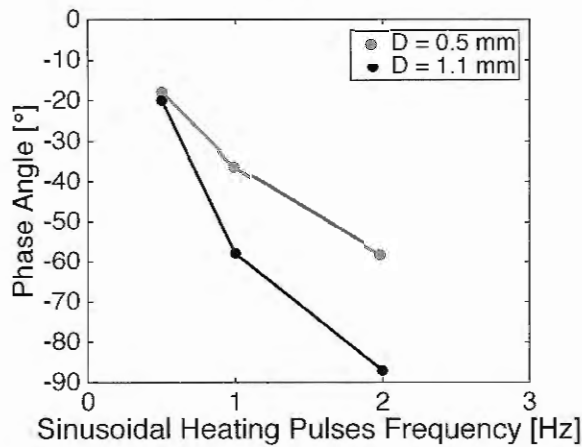
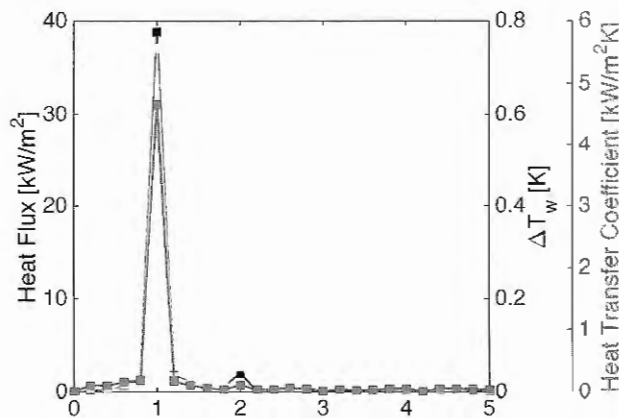
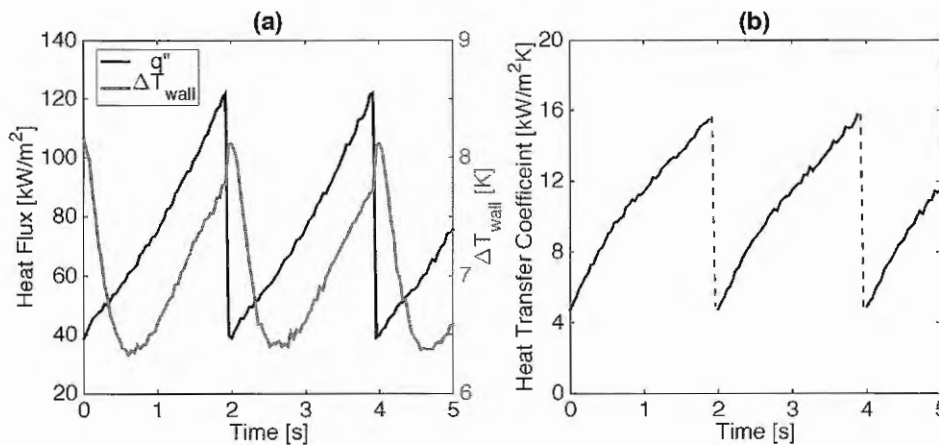


Figure 6.4 – Fourier transform of the zero-mean heat flux, ΔT_w and HTC signals for R134a, $D = 1.1$ mm, $T_{sat} = 31^\circ\text{C}$, $G = 400$ kg/m²s, $\bar{x}_{hpot} = 60\%$, $\bar{q}''_{hpot} = 120$ kW/m², $\Delta q''_{hpot} = 40$ kW/m² and $f = 1$ Hz



The results shown in Fig. 6.5 (a) and 6.5 (b) exemplify the typical transient behavior of the ΔT_w and HTC, respectively, for saw tooth heating pulses. The discontinuities observed in the heat transfer coefficient behavior are associated to the sudden drop of the heat flux. The peak of wall superheat temperature occurs right after the heat flux peak. As the heat flux sharply drops to its lowest value, ΔT_w promptly reduces. From this point, the heat flux rises linearly while ΔT_w keeps decreasing until reaches its minimum. The minimum of the heat flux and ΔT_w does not occur concomitantly because of the thermal inertia of tube wall and thermocouple bead. After ΔT_w achieve a minimum value, both the heat flux and ΔT_w rises linearly up to their respective maximum values. This cycle is maintained with the heating pulses. Figure 6.5 (b) indicates that the heat transfer coefficient rises alongside with the heat flux at almost constant rate.

Figure 6.5 –Transient behavior of the (a) wall superheat temperature and (b) HTC under sinusoidal heat pulses. R134a, $D = 1.1$ mm, $T_{sat} = 31^\circ\text{C}$, $G = 400$ kg/m²s, $\bar{x}_{hpot} = 60\%$, $\bar{q}''_{hpot} = 120$ kW/m², $\Delta q''_{hpot} = 40$ kW/m² and $f = 1$ Hz



6.4. Parametric Analysis of the Transient Behavior of the Wall Superheat Temperature

In this section, a parametric analysis of the experimental data is performed to determine the influence of the heat load main parameters (heat flux waveform, frequency, amplitude and average value) and the fluid conditions (vapor quality and mass velocity) on the transient behavior of the wall superheat temperature and HTC.

For this parametric analysis, histograms are used to represent the variations of mean and amplitude values of the wall superheat temperature. Histograms permit to evaluate the main trends of the results as well as if the results are statistically significant, i.e. if the differences are

higher than the experimental uncertainties. The behavior of the wall superheat temperature is computed among tests performed under similar conditions varying only one experimental parameter at a time.

6.4.1. Waveform Effects

Figure 6.6 exhibits the frequency distribution of the average ΔT_w difference between square and sinusoidal heating pulses from the saw tooth waveform, assumed as the baseline condition for comparison. The results revealed that the average ΔT_w is marginally affected by changes in the heating pulses waveform, as the frequency distributions mean values are close to zero. Also, the standard deviation of the frequency distributions shown in Fig. 6.6 are around 0.15°C , thus the majority of the average ΔT_w changes are not significant as they are lower than the measurement uncertainty. Based on this evidence, it is possible to conclude that the average ΔT_w is independent of the waveform for the experimental conditions of the present study.

The results displayed in Fig. 6.7 show that the mean value of the frequency distributions are greater than zero, indicating that the amplitude of ΔT_w was smallest for saw tooth heating pulses. Additionally, the highest frequency distribution mean value is recorded for the comparison between square and saw tooth waveforms, independently of the tube diameter. Based on these facts, it can be concluded that the greatest amplitudes of wall temperature fluctuations occur under square heating pulses, followed by sinusoidal and saw tooth waveforms.

Figure 6.6 – Illustration of the effect of the heat flux waveform on the frequency distribution of the average wall superheat temperature

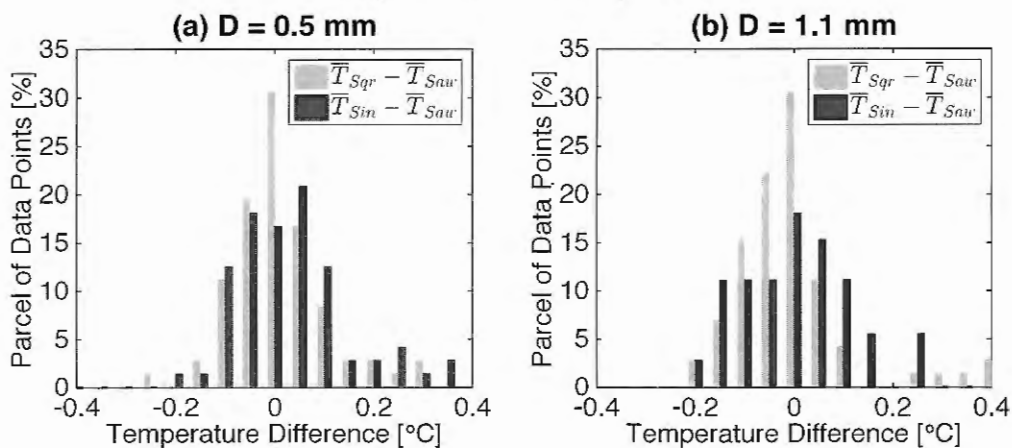
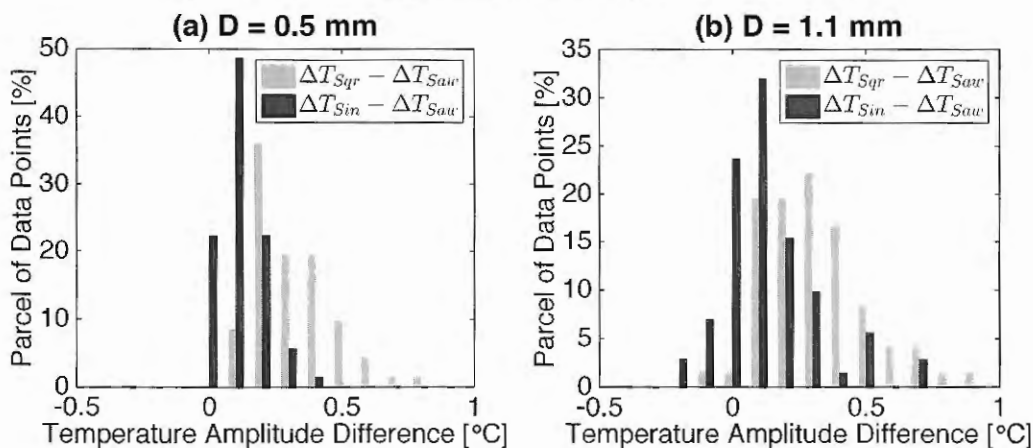


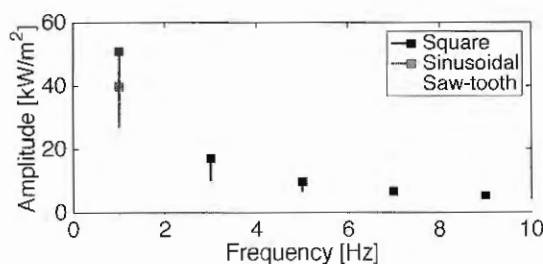
Figure 6.7 – Illustration of the frequency distribution of the difference of amplitude of wall superheat temperature adopting the saw tooth heating pulses as the baseline



As previously mentioned in Section 5.8 (time constant analysis), the heat flux signal can be related to the wall superheat temperature by a first-order lag transfer function $\frac{K}{\tau s + 1}$ using the system identification toolbox from MATLAB. The regression of the constants K and τ to the experimental results indicates that, under fixed fluid conditions (T_{sat} , G and x), K and τ remain constant independently of the heat flux waveform. Therefore, the wall superheat temperature is given by the transient response of a low-pass filter to the heat flux signal, and, the level of wall superheat temperature fluctuations is linked to the amplitude of the lowest heat flux harmonic.

Figure 6.8 shows the Fourier transform of the heat flux signal for square, sinusoidal and saw tooth waveforms with a period time of 1 second, amplitude of 40 kW/m^2 and zero DC offset. From this figure, it is seen that, for the lowest harmonic frequency (1 Hz), the ranking of amplitudes from greatest to smallest (square, sinusoidal and then saw tooth) is exactly the same ranking previously derived based on the parametric analysis of the data. Therefore, to predict the ranking of greater oscillations of wall superheat temperature for different waveforms, an evaluation of the magnitude of the lowest heat flux harmonic is recommended.

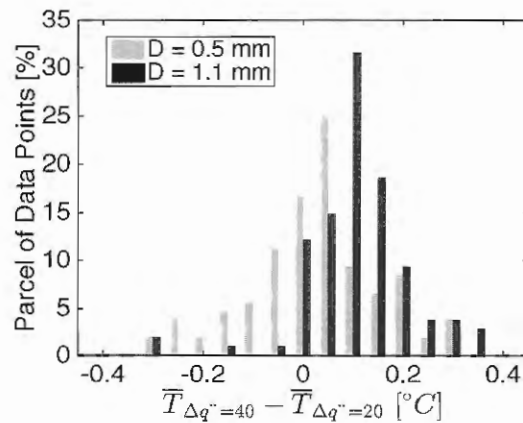
Figure 6.8 – Fourier transform of the heat flux signal for $\Delta q''_{hpot} = 40 \text{ kW/m}^2$ under different waveforms



6.4.2. Heat Flux Amplitude Effects

The outcomes of an increment of the heating pulses amplitude from $\Delta q'' = 20$ to 40 kW/m^2 on the average ΔT_w are shown in Fig. 6.9. The frequency distribution of the average ΔT_w difference between the lowest (20 kW/m^2) and the highest (40 kW/m^2) tested amplitudes is displayed according to this figure. The average ΔT_w seems to be marginally affected by changes of the heating pulses amplitude, as most of the ΔT_w variations are lower than the temperature measurement uncertainty of $\pm 0.15^\circ\text{C}$. Furthermore, the mean value of the frequency distributions also falls within the uncertainties of temperature measurements.

Figure 6.9 – Illustration of the effect of the heat flux amplitude on the frequency distribution of the average wall superheat temperature

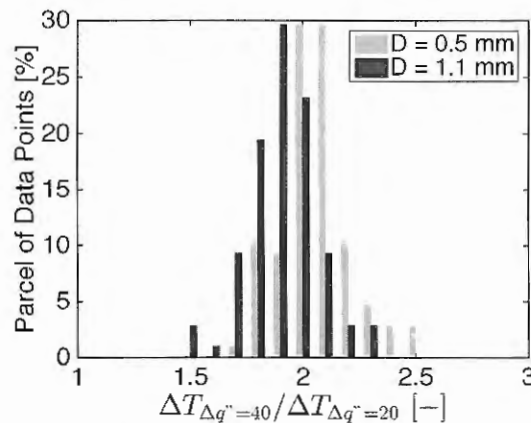


An analysis of Fig. 6.10 reveals that the relative level of ΔT_w oscillations rises as the amplitude of the heating pulses is increased. This result comes at no surprise as it is intuitive to reason that under fixed average heat flux, the ΔT_w oscillations should monotonically increase with increasing the amplitude of the heat flux variations. The remarkable part about the results of Fig. 6.10 is that the frequency distributions medians were very close to two, indicating that the ΔT_w amplitude approximately doubled as the heat flux amplitude is doubled, independently of the tube diameter. An analysis of the HTC amplitude also revealed that this quantity doubles when the heating pulses amplitude is doubled.

The facts abovementioned suggest that there is a linear proportionality between the amplitude of the heat flux and the amplitudes of ΔT_w and HTC. Because only two heat flux amplitudes were tested, there is no guarantee that this linear relationship holds true under more severe heat load oscillations. Also, the results from Fig. 6.10 corroborate the advantage of using flow boiling for cooling transient loads due to its self-enhancing effect, i.e. the instantaneous

HTC increases/decreases with the heat load, damping out the temperature oscillations and favoring temperature uniformity.

Figure 6.10 – Illustration of the effect of heat flux amplitude on the frequency distribution of the amplitude of wall superheat temperature



6.4.3. Effects of Heat Flux Frequency

Figure 6.11 shows the histogram of the average ΔT_w differences between the results for the heating pulses frequencies evaluated in the present study. For this parametric analysis, the experimental data for $f_{q''} = 0.5$ Hz is taken as the baseline condition. According to Fig. 6.11, it seems that the differences in the average ΔT_w among heating frequencies of 1 and 2 Hz and the baseline condition are not substantial because most of the average temperature variations among tests were within the measurement uncertainty. Hence, the average ΔT_w is said to be independent of $f_{q''}$. This result suggests that no significant modifications of the heat transfer mechanisms take place with varying $f_{q''}$.

Figures 6.12 (a) and 6.12 (b) shows the effect of $f_{q''}$ on the amplitude of ΔT_w oscillations. These figures reveal that the amplitude of oscillations of ΔT_w decreases as $f_{q''}$ is increased. This effect is more pronounced for $D = 1.1$ mm, as larger deviations between the results for different frequencies are displayed. This observation agrees with the results for the average time constant shown in Fig. 5.14, according to which the average time constant for $D = 1.1$ mm is three times greater than the time constant for $D = 0.5$ mm. Therefore, it can be concluded that for a given frequency, larger damping of temperature oscillations is expected to occur for the greatest tube diameter.

Figure 6.11 – Illustration of the heat flux waveform frequency on the frequency distribution of the average wall superheat temperature

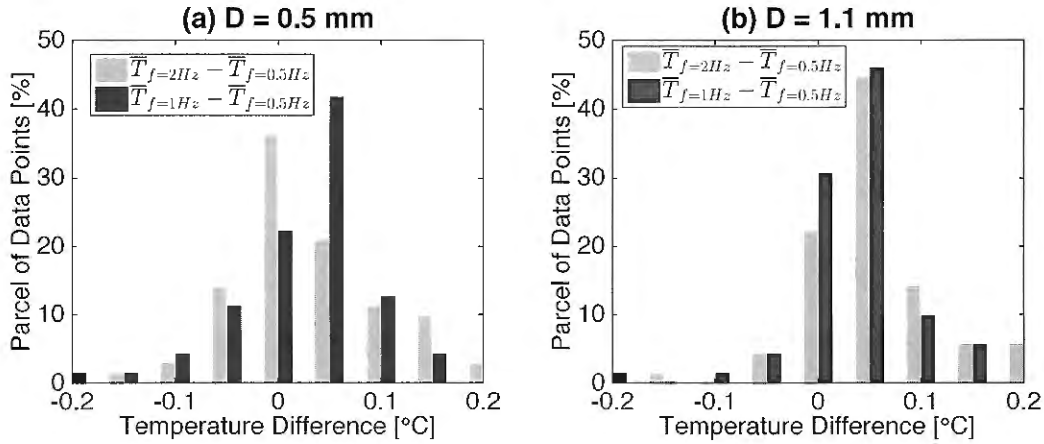
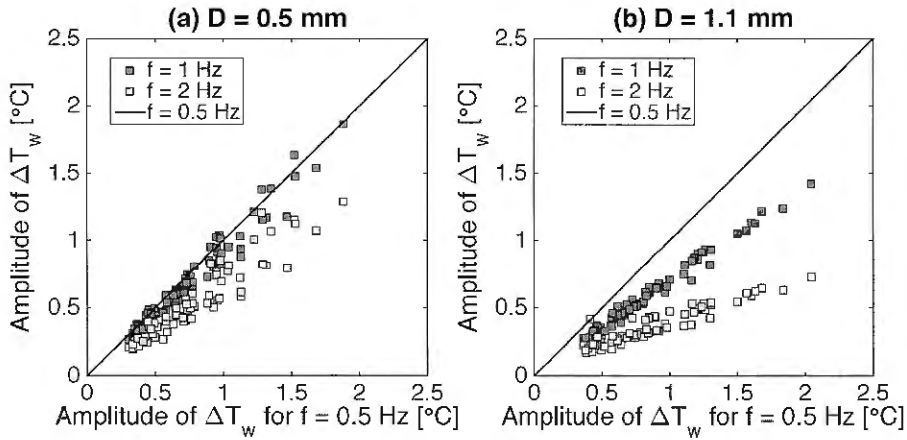


Figure 6.12 – Illustration of the influence of heat flux frequency on the amplitude of the wall superheat temperature oscillations



It is also seen from Fig. 6.12 (b) that when the results for $f_{q''} = 1$ and 2 Hz are plotted as functions of the results for $f_{q''} = 0.5$ Hz, the data points are distributed according to a almost straight line. A linear curve fitting indicates that the amplitude of oscillations at 2 Hz is approximately 60% lower than for $f_{q''} = 0.5$ Hz. For $f_{q''} = 1$ Hz, the oscillations are 30% lower than for $f_{q''} = 0.5$ Hz. These constants of proportionality (0.4 and 0.7) suggest that the attenuation of the temperature fluctuations is strongly associated to thermal inertia effects of tube walls and thermocouple bead. This occurs because, independently of the fluid conditions (G and x) and the heating pulses waveform, \bar{q}'' and $\Delta q''$, the amplitude of ΔT_w under $f_{q''} = 1$ and 2 Hz is uniquely related to the amplitude of ΔT_w under 0.5 Hz through a constant of proportionality. This observation permits to speculate that the reduction of temperature oscillations with increasing $f_{q''}$ is not associated to changes of the boiling mechanisms. It is expected that at high enough $f_{q''}$, ΔT_w becomes nearly constant due to severe damping of

fluctuations. In this scenario, the effects of cyclic variations of heat load becomes negligible, as the thermal inertia damps out temperature fluctuations and the heat transfer rate delivered to the fluid is analogous to steady heating conditions under time-averaged heat flux dissipation.

6.4.4. Effects of the Average Heat Flux Level

Figures 6.13 and 6.14 display the frequency distributions of the variations of the average ΔT_w and HTC, respectively, as the mean dissipated heat flux is increased from 80 to 120 kW/m². The results show that the average ΔT_w and the HTC rise as the average heat flux is increased. This behavior is verified independently of the heat flux waveform. It is speculated that the increment of the HTC with the elevation of the average heat flux is linked to the enhancement of nucleate boiling effects, as the density of nucleation sites increases with increasing heat flux. The mean increment of average wall superheat temperature was lower for $D = 0.5$ mm (0.75°C) than for $D = 1.1$ mm (1.2°C). Consequently, the average improvement of the HTC was greater for $D = 0.5$ mm (34%) when compared to $D = 1.1$ mm (28%), as shown in Fig. 6.14.

Figure 6.13 – Illustration of the influence of the average heat flux level on the frequency distribution of the average wall superheat temperature

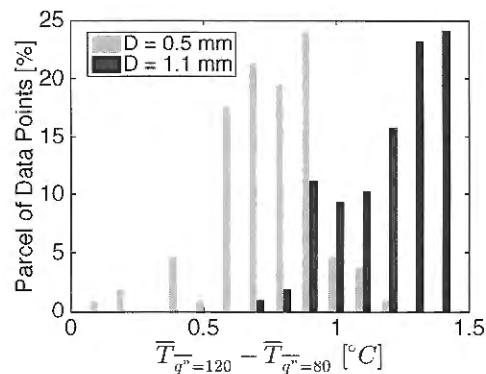
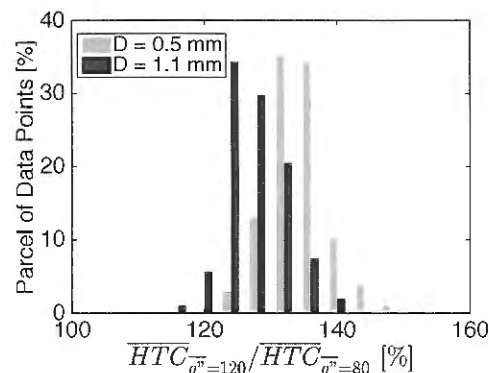
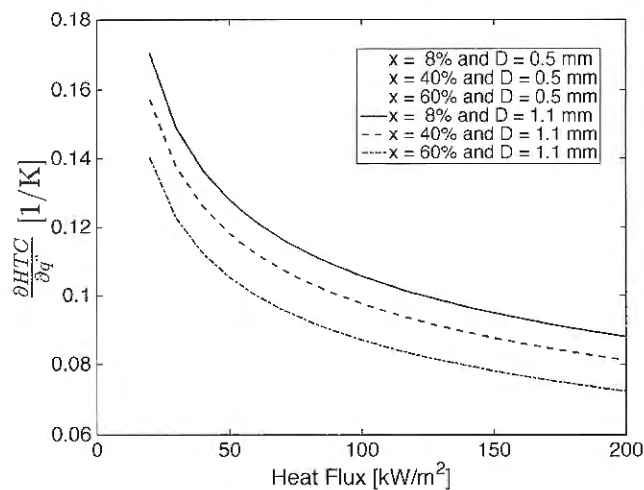


Figure 6.14 – Illustration of the effect of the average heat flux level on the frequency distribution of the average heat transfer coefficient



The results displayed in Figs. 6.13 and 6.14 reveal that the HTC sensitivity to variations of the heat flux average level was greater for the smallest tube diameter. Figure 6.15 illustrates the behavior of the partial derivative of the heat transfer coefficient with respect to the heat flux (or the HTC sensitivity to the heat flux) based on the method of Kanizawa et al. (2016) for three vapor qualities and two tube diameters.

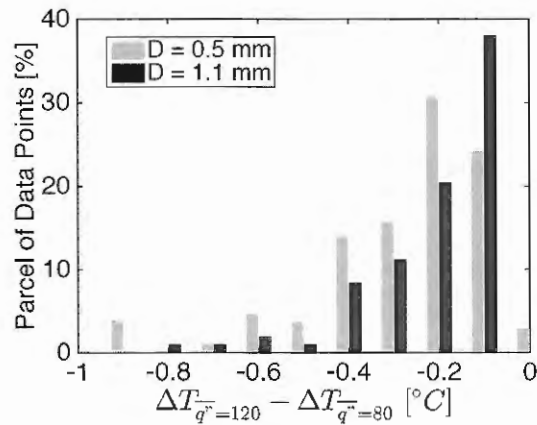
Figure 6.15 – First partial derivative of the heat transfer coefficient with respect to the heat flux (or the heat transfer coefficient sensitivity to the heat flux) according to the method of Kanizawa et al. (2016), R134a and $T_{sat} = 31^\circ\text{C}$



According to Fig. 6.15, the first derivative is always positive, indicating that the average HTC increases monotonically with augmenting the average heat flux. Also, the HTC sensitivity to the heat flux according to the prediction method is greater for the smaller tube diameter, corroborating with the results shown in Fig. 6.13, according to which lower average ΔT_w differences are observed for $D = 0.5$ mm. Additionally, the curves of Fig. 6.15 reveal that the differences of HTC sensitivity to the heat flux between the two tube diameters become more pronounced as the vapor quality increases.

Figure 6.16 exhibits the difference of ΔT_w amplitude between the tests for average heat flux of 80 and 120 kW/m². From this figure, it is seen that the distribution presents only negative values, indicating that temperature oscillations with higher amplitude occurs for the lowest average heat flux, independently of the tube diameter. This result reveals that the increment of average heat flux reduces the level of ΔT_w fluctuations. In other words, the effectiveness of the self-enhancing cooling effect exhibited by flow boiling under transient loads strengthen as the average level of heat dissipation is increased.

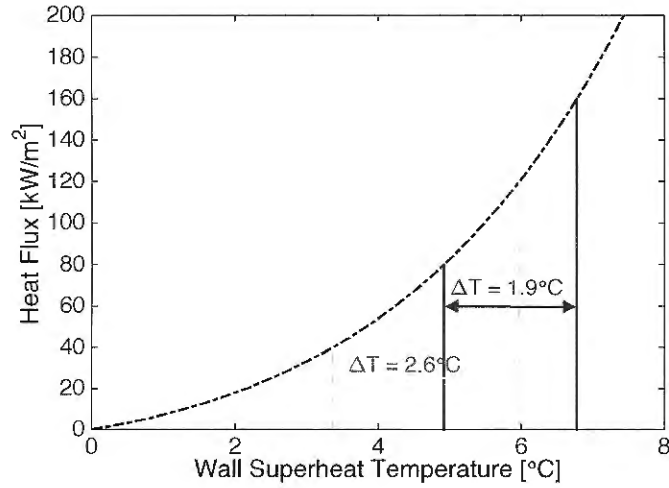
Figure 6.16 – Illustration of the influence of the average heat flux level on the frequency distribution of the amplitude of wall superheat temperature variation



It is worth to note that, even though the average HTC increases with increasing the heat flux level (and consequently the time constant of the temperature sensor), the amplitude of the oscillations of ΔT_w decreases, as shown in Fig. 6.16. Therefore, the reduction of the amplitude of the oscillations of ΔT_w with increasing average heat flux should be linked to modifications associated to the boiling mechanisms, favoring efficient heat transfer. It is well known that the increment of the average heat flux activates a wider range of sizes of nucleation cavities under conditions when nucleate boiling effect is the dominant heat transfer mechanism. This behavior implies on the augmentation of the self-enhancing cooling effect, and, consequently, on the reduction of the ΔT_w amplitude.

Figure 6.17 shows a boiling curve estimated according to the method of Kanizawa et al. (2016) for $D = 0.5$ mm, $T_{sat} = 31^\circ\text{C}$, $G = 400$ kg/m²s and $x = 60\%$. This curve permits to visualize the differences of the amplitude of ΔT_w as the average heat flux is increased while the half-amplitude is kept constant. When the heat flux oscillates between 40 and 120 kW/m², the ΔT_w amplitude is 2.6°C. As the average heat flux is increased and set to oscillate from 80 to 160 kW/m², the corresponding ΔT_w amplitude decreases to 1.9°C. This reduction of temperature oscillation can be associated to the fact that the boiling curve becomes steeper as the heat flux increases due to the activation of smaller cavities. Moreover, for higher heat fluxes, the rate of change of the slope of the boiling curve (its second derivative) becomes small as most of the nucleation cavities are already activated. This observation implies that, under high heat fluxes, further augmentation of the average heat flux marginally reduces the ΔT_w amplitude for fixed heat flux half-amplitude when compared to low heat fluxes.

Figure 6.17 – Boiling curve for R134a at $G = 400 \text{ kg/m}^2\text{s}$, $D = 0.5 \text{ mm}$, $T_{sat} = 31^\circ\text{C}$ and $x = 60\%$ according to Kanizawa et al. (2016), illustrating the reduction of wall superheat temperature amplitude with the increment of the average heat flux



6.4.5. Vapor Quality Effects

Figures 6.18 (a) and 6.18 (b) exhibit the effects of the vapor quality on the frequency distributions of the average ΔT_w difference. In these figures, the results for $x = 40$ and 60% are compared to the baseline condition of $x = 8\%$. According to Fig. 6.18 (a), for $D = 0.5 \text{ mm}$, the frequency distribution of the average ΔT_w differences is bimodal. The two main modes were found to be linked to the different mass velocities, as indicated in the figure. For a given vapor quality, the mode with greatest negative value corresponds to the highest mass velocity. Notable average ΔT_w reductions up to 1.5°C were observed for $D = 0.5 \text{ mm}$ with vapor quality increasing from 8 to 60% and $G = 600 \text{ kg/m}^2\text{s}$. For $D = 1.1 \text{ mm}$, the frequency distribution depicted in Fig. 6.18 (b) reveals that the effect of vapor quality on the average ΔT_w is less pronounced, as the majority of the data is within the temperature measurement uncertainty. The comparison between the results obtained for the two tube diameters suggests that the heat transfer coefficient sensitivity to the vapor quality diminishes as the tube diameter increases.

Figure 6.19 (a) and 6.19 (b) depict the variation of the average HTC with vapor quality for $D = 0.5$ and 1.1 mm , respectively. The results for the average HTC agree with the trends of the data for the average ΔT_w displayed in Fig. 6.18. For $D = 0.5 \text{ mm}$, the average HTC progressively increases with increasing vapor quality. Two modes corresponding to mass velocities of 400 and $600 \text{ kg/m}^2\text{s}$ are also noted for $D = 0.5 \text{ mm}$, as indicated in Fig. 6.19 (a). The parcel of the data revealing an increment of the average HTC is higher for the greatest mass velocity. Also, average HTC increments higher than the uncertainties of the HTC measurements

(up to 30%) are observed for $D = 0.5$ mm. For $D = 1.1$ mm, the results of Fig. 6.19 (b) suggest that the HTC improves only marginally with increasing the vapor quality from 8 to 40%, as most of the differences are within the uncertainties of HTC. However, the majority of the results suggests that the average HTC slightly decreases when the vapor quality varies from 8 to 60%. For $D = 1.1$ mm, most of the average HTC variations are within the range of experimental uncertainties, hence, for this tube diameter, the average HTC was found to be almost independent of the vapor quality.

Figure 6.18 – Illustration of the influence of vapor quality on the frequency distribution of the difference of the average wall superheat temperature

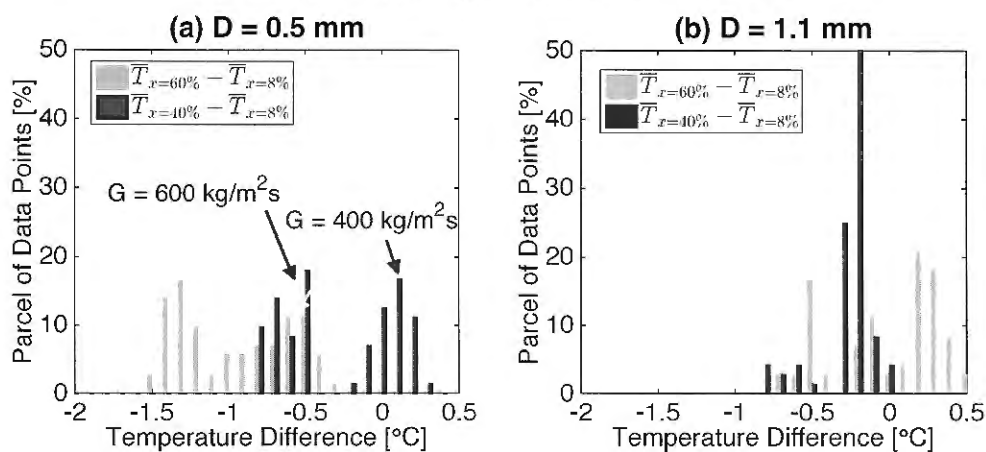
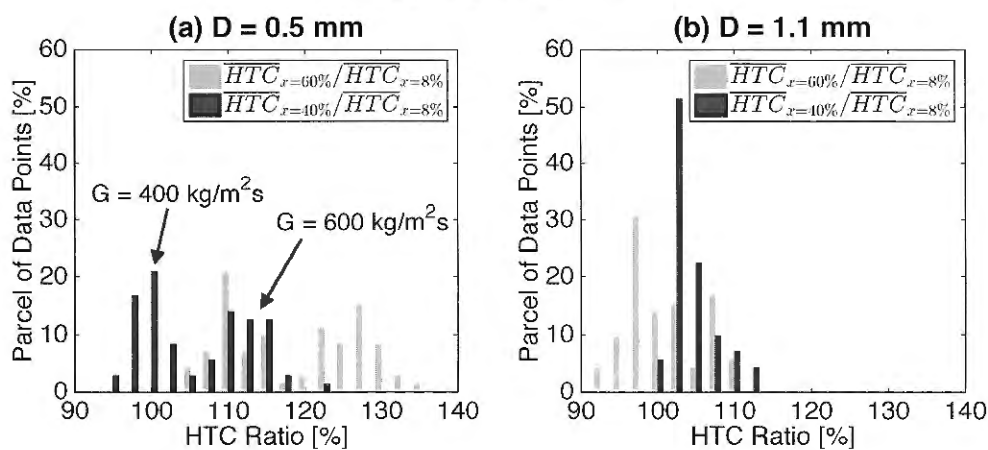


Figure 6.19 – Illustration of the influence of the vapor quality on the frequency distribution of the average heat transfer coefficient



According to Fig. 6.20, the prediction method of Kanizawa et al. (2016) is capable of capturing the main experimental data trends of the average HTC with increasing vapor quality. For $D = 0.5$ mm and according to this method, the heat transfer coefficient increases with increasing mass velocity, which translated into the bimodal distributions, as seen in Figs. 6.18 (a) and 6.19 (a). However, for $D = 1.1$ mm, the HTC is practically independent of the mass

velocity. Moreover, for $D = 1.1$ mm, the heat transfer coefficient is almost independent of the vapor quality for $5\% \leq x \leq 60\%$, as shown in Fig. 6.20. Also, according to this figure, the heat transfer coefficient decreases less than 10% by increasing the vapor quality from 8 to 70%. These behaviors agree with those illustrated in Fig. 6.19 (b), according to which marginal variations of the average HTC are displayed ($\pm 10\%$) with increasing vapor quality and a slight degradation of the average HTC is noted when the vapor quality changes from 8 to 60%. It can be speculated that this reduction of the average HTC from 8 to 60% could be linked to the gradually suppression of nucleate boiling effects caused by flow acceleration due to higher void fractions, which lowers the heat transfer efficiency. Also, for $D = 0.5$ mm in Fig. 6.20, the method of Kanizawa et al. (2016) also correctly predicts the monotonic improvement of the average HTC with increasing the vapor quality within the interval $5\% \leq x \leq 60\%$. In summary, the reduction of the tube diameter improves the average HTC because the augmentation of the convective effects is superior to the suppression of nucleate boiling effects caused by the flow acceleration, which causes the HTC to respond positively to increasing vapor quality and mass velocity for $D = 0.5$ mm.

Figure 6.20 – Heat transfer coefficient vs. vapor quality according to the method of Kanizawa et al. (2016) for R134a at $T_{sat} = 31^\circ\text{C}$

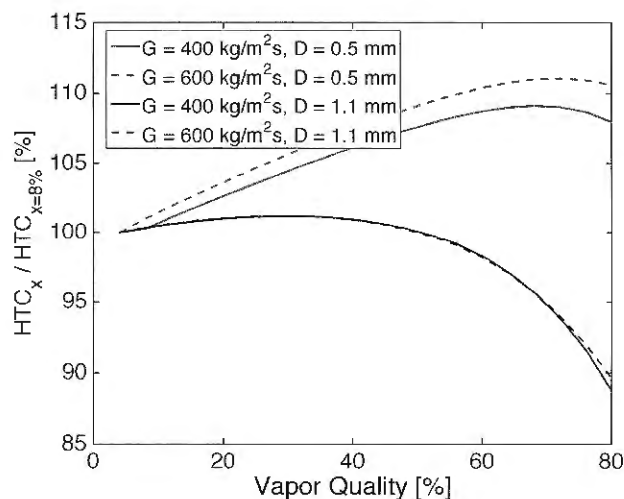
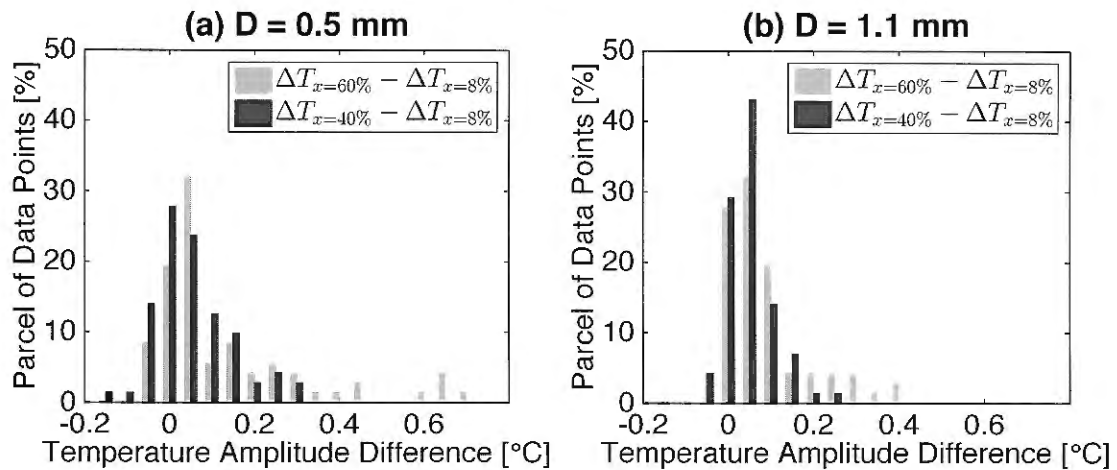


Figure 6.21 shows the effect of vapor quality on the fluctuations of the ΔT_w . The results of Fig. 6.21 revealed that, although the majority of the data indicate an improvement of the amplitude of ΔT_w , most of the variations are within the uncertainties of the measurements. The improvement of ΔT_w can be associated to the enhancement of the average HTC, which lessens the thermal inertia effects and favors higher amplitude of ΔT_w . Also, at higher vapor qualities, the two-phase flow velocity increases, which results in a gradual suppression of nucleate boiling

effects and should reduce the self-enhancing cooling effect, resulting in higher amplitudes of ΔT_w . Therefore, the reduction of thermal inertia and gradual suppression of nucleate boiling effects influence concomitantly the results of Fig. 6.21.

Figure 6.21 – Influence of vapor quality on the frequency distribution of the amplitude of fluctuations of the wall superheat temperature

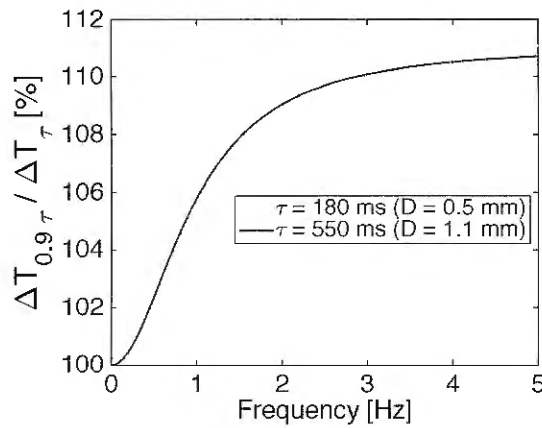


The effects of the enhancement of average HTC (and consequently the time constant reduction) on the ΔT_w oscillation level can be assessed by considering sinusoidal oscillations of the wall superheat temperature (or pure harmonic oscillation). Under this condition, the magnitude of the temperature attenuation due to thermal inertia effects is proportional to $\frac{1}{\sqrt{1+(2\pi f\tau)^2}}$, similarly to the classical theory of first-order lag systems. Also, the time constant is assumed to be inversely proportional to the average HTC, analogously to the lumped heat capacity method.

Figure 6.22 illustrates the ratio of temperature amplitudes for a time constant of 0.9τ and the respective baseline condition τ calculated based on the expression $\frac{\Delta T_{w0.9\tau}}{\Delta T_{w\tau}} = \frac{\sqrt{1+(2\pi f\tau)^2}}{\sqrt{1+(2\pi f0.9\tau)^2}}$. In this figure, time constants of $\tau = 180$ and 550 ms are considered for $D = 0.5$ and 1.1 mm, respectively (see Section 5.8). According to Fig. 6.22 and based on this analysis, the ΔT_w amplitude increases with decreasing the time constant. Moreover, the improvement of ΔT_w increases with increasing the frequency until its value stabilizes asymptotically to a value close to 11% for both tubes. Because the maximum temperature half-amplitude registered during the tests was 2°C (see Fig. 6.12), the reduction of the time constant will lead to a maximum temperature amplitude improvement of 0.22°C for $D = 1.1$ mm. For $f = 0.5$ Hz and $D = 1.1$ mm, the improvement of ΔT_w is only 0.04°C . On the other hand, the results from Fig.

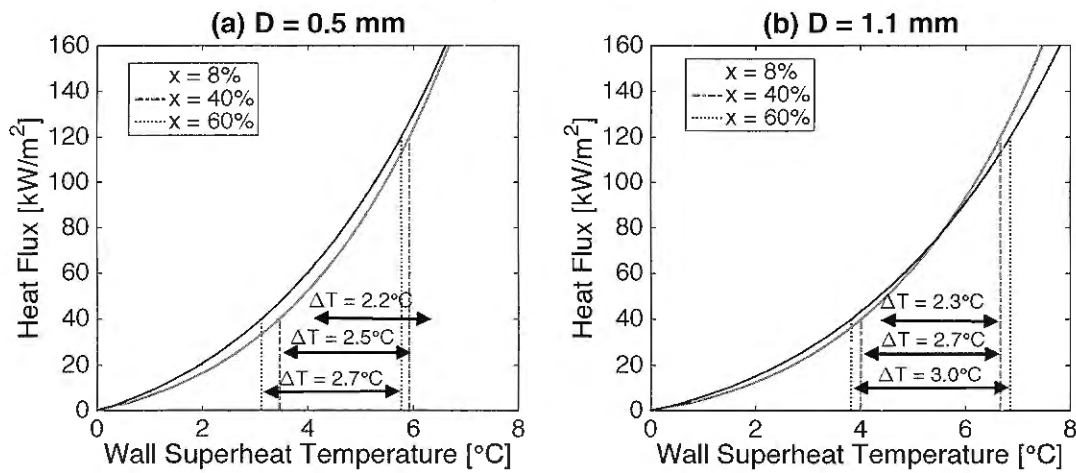
6.21 (b) indicate that temperature amplitude differences up to 0.4°C were recorded for $D = 1.1$ mm, therefore, higher than the values obtained from this analysis. Hence, it is considered that the slight reduction of the time constant due to the improvement of the average HTC is not sufficient itself to explain the enlargement of the intensity of temperature oscillations displayed in Fig. 6.21.

Figure 6.22 – Illustration of the influence of the increment of the average heat transfer coefficient (and consequently the slight reduction of the time constant) on the improvement of wall superheat temperature oscillations



Figures 6.23 (a) and 6.23 (b) illustrates the variation of ΔT_w under fixed heat flux half-amplitude (40 kW/m^2) and average value (80 kW/m^2) for vapor qualities of 8, 40 and 60% according to the method of Kanizawa et al. (2016).

Figure 6.23 – Illustration through boiling curves of the effect of vapor quality variations on ΔT_w under fixed heat flux average value and amplitude based on the method of Kanizawa et al. (2016) for R134a at $G = 600 \text{ kg/m}^2\text{s}$ and $T_{sat} = 31^\circ\text{C}$



Based on the results displayed in Fig. 6.23, it can be concluded that ΔT_w amplitude increases monotonically with vapor quality when the average heat flux and its half-amplitude

are maintained fixed, independently of the tube diameter. Based on the results displayed in Figs. 6.21 to 6.23, it is speculated that, although most of the experimental results exhibited variations of ΔT_w within the range of experimental uncertainties, the ΔT_w amplitude increases with increasing vapor quality, indicating a reduction of the self-enhancing cooling effect. Further tests are needed to confirm this premise. It is also speculated that the increment of ΔT_w amplitude (and reduction of self-enhancing effect) is linked to the gradual suppression of nucleate boiling effects caused by the increment of two-phase flow velocity with increasing vapor quality.

6.4.6. Effects of Mass Velocity

Figures 6.24 and 6.25 display the frequency distribution of the variation of the average ΔT_w and HTC, respectively, as the mass velocity is increased from 400 to 600 kg/m²s. According to these figures, the average ΔT_w drops and the average HTC increases with increasing the mass velocity, independently of the tube diameter. For $D = 0.5$ mm, the improvement of the average HTC with the mass velocity is consistent with the predictions provided by the method of Kanizawa et al. (2016) previously shown in Fig. 6.20. However, for $D = 1.1$ mm, the method of Kanizawa et al. (2016) predicts no changes of the average HTC while the experimental data of Figs. 6.24 and 6.25 reveals an increment of average HTC for increasing mass velocity, which demonstrates that this method was not able to capture the enhancement of convective effects for $D = 1.1$ mm. Moreover, the HTC improves because the contribution to the overall heat transfer to the enhancement of convective effects is greater than the heat transfer penalty associated to the suppression of nucleate boiling effects with both resulting from the higher two-phase flow velocity.

Figure 6.24 – Illustration of the influence of the mass velocity on the frequency distribution of the average wall superheat temperature

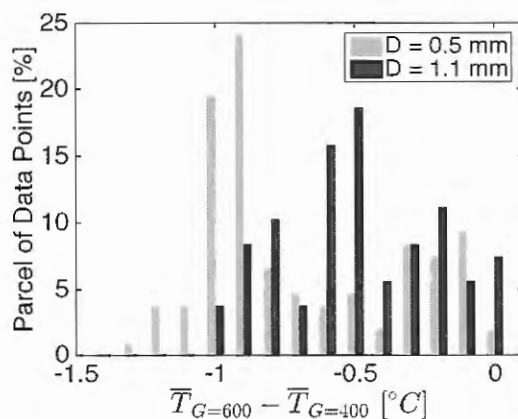
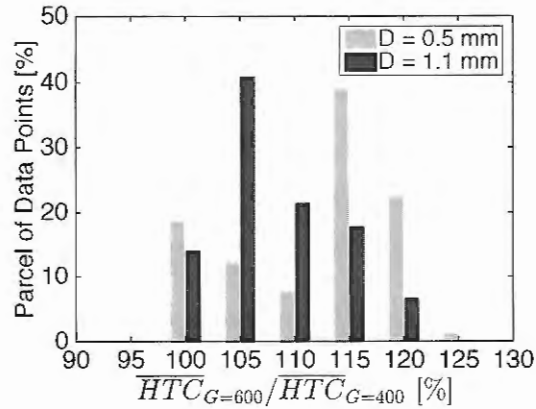


Figure 6.25 – Illustration of the effect of the mass velocity on the frequency distribution of the average heat transfer coefficient



The results shown in Fig. 6.26 reveal the differences of the amplitudes of the oscillations of ΔT_w as the mass velocity increases from $G = 400$ to $600 \text{ kg/m}^2\text{s}$. According to this figure, most of the results indicate variations within the range of experimental uncertainties. Even though the majority of the variations are lower than the uncertainties, most of the temperature differences are positive and the mean value of the frequency distributions is greater than zero, suggesting a marginal improvement of ΔT_w amplitude with increasing mass velocity. It is recognized that additional data is needed to confirm this behavior, however, it is speculated that the increment of flow velocity increases the magnitude of the suppression of nucleation effects and reduces the self-enhancing effect, leading to higher ΔT_w amplitude of fluctuations.

Figure 6.26 – Illustration of the effect of the mass velocity on the frequency distribution of the amplitude of the wall superheat temperature

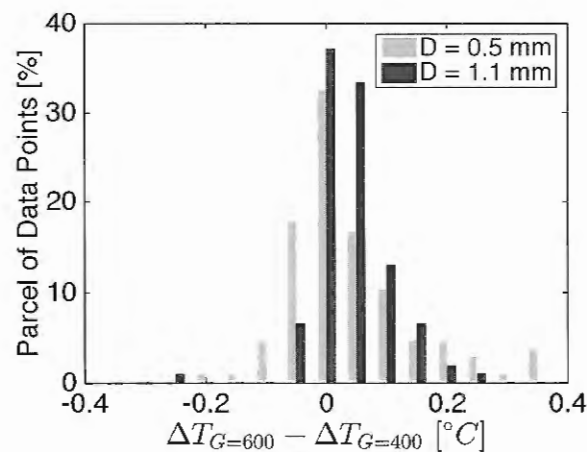
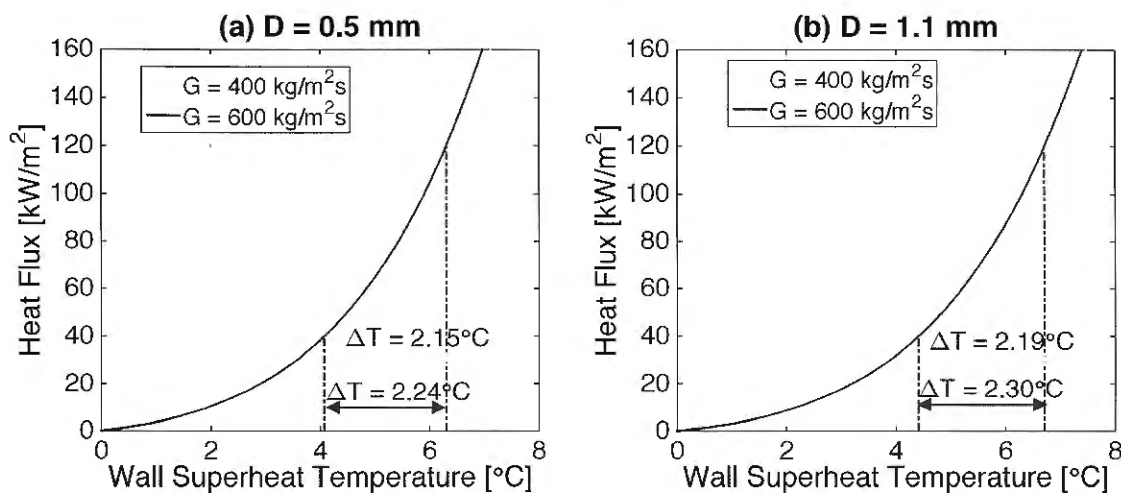


Figure 6.27 (a) and 6.27 (b) show the boiling curves based on the method of Kanizawa et al. (2016). According to these figures, ΔT_w improves only marginally within the range of its

uncertainty when the mass velocity raises from 400 to 600 kg/m²s, corroborating the results shown in Fig. 6.26.

Figure 6.27 – Illustration based on boiling curves of the effects of mass velocity on the variation of the wall superheat temperature based on the method of Kanizawa et al. (2016) for R134a at $T_{sat} = 31^\circ\text{C}$ and $x = 8\%$.



6.5. Assessment of Flow Boiling Prediction Methods to Transient Heating

In this section, the experimental results for transient heating obtained under the conditions listed in Tab. 6.1 are compared against eight methods from literature developed to predict the flow boiling HTC in small diameter channels under steady-state heating. These methods are described in Section 2.5 and a summary of them is given in Tab. 2.1. The objective of this comparison is to evaluate if the methods developed for steady heating conditions can accurately predict the average heat transfer coefficient under transient heat loads and the respective amplitude of wall superheat temperature oscillations.

It is important to properly estimate the amplitude of wall superheat temperature oscillations and its average value under transient and cyclical heat loads because this permits to evaluate the minimum and maximum wall temperatures, an important design constraint for heat sinks. To the best of present author's knowledge, there are no methods in literature for predicting ΔT_w under transient heat loads. Therefore, it is reasonable to assess if the current methods developed for steady-state heating conditions can be extrapolated to predict ΔT_w variations under transient heat loads.

To accomplish the comparison of the experimental data with prediction methods, the conditions corresponding to the experimental results are used as the input data and the heat transfer coefficient is estimated for every time instant according to each method. The

instantaneous local pressure, enthalpy, heat flux and mass velocity at the hotspot central region are used to estimate the local HTC for a given time instant. Through this procedure, the transients of the predicted HTC are an outcome of the transient boundary conditions, which comes from the experimental data. Then, the wall superheat temperature is calculated according to the Newton's law of cooling.

The accuracy of the methods from literature to predict the average heat transfer coefficient (and consequently the average ΔT_w) and the half-amplitude of ΔT_w oscillations is evaluated through the parcel of experimental results predicted within error bands of $\pm 20\%$, $\lambda_{20\%}$, and $\pm 30\%$, $\lambda_{30\%}$, and the mean absolute deviation Ψ , which is defined as follows:

$$\Psi_{\bar{\alpha}} = \frac{1}{N} \sum_{i=1}^N \left| \frac{\bar{\alpha}_{estimated_i} - \bar{\alpha}_{experimental_i}}{\bar{\alpha}_{experimental_i}} \right| \quad (6.1)$$

$$\Psi_{\Delta T_w} = \frac{1}{N} \sum_{i=1}^N \left| \frac{Amp. \Delta T_{w estimated_i} - Amp. \Delta T_{w experimental_i}}{Amp. \Delta T_{w experimental_i}} \right| \quad (6.2)$$

where N is the number of tests, $\bar{\alpha}$ is the average heat transfer coefficient calculated through Eq. 5.21 and the half-amplitude of the wall superheat temperature is estimated through Eq. 5.22.

6.5.1. Average Heat Transfer Coefficient

In the parametric analysis, it was shown under transient and cyclical heat loads, that the average HTC is independent of the heat flux waveform, its half-amplitude and frequency, hence it is reasonable to expect that the methods developed for steady heating can be extended to predict the average HTC for transient heating. Table 6.2 presents the mean absolute deviation, standard deviation and the parcel of the data predicted with deviations within $\pm 20\%$ and $\pm 30\%$ associated to the predictions of the average HTC. Figure 6.28 displays the experimental vs. estimated average HTC for the methods listed in Tab 6.2. From this table, it is verified that the method of Kanizawa et al. (2016) was able to predict 88.2% of the average HTC results within a deviation range of $\pm 20\%$ for both tube diameters, leading to the most accurate predictions among the eight methods compared in this section.

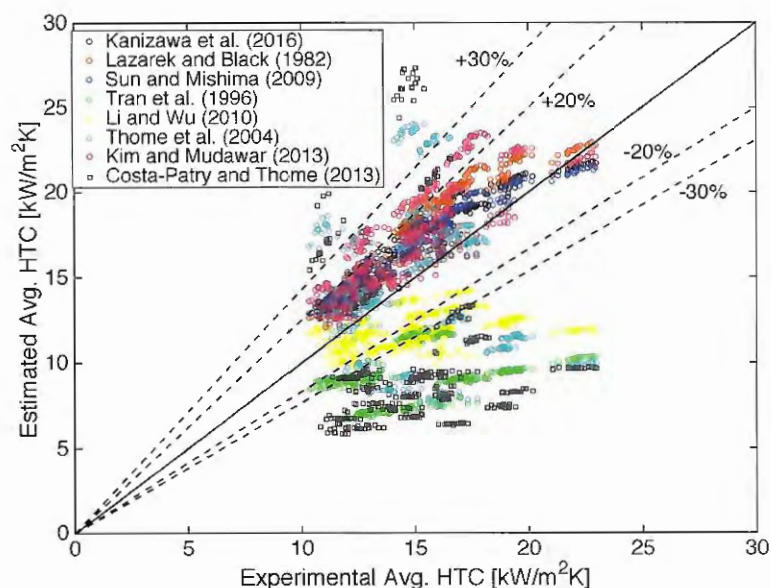
The method of Kanizawa et al. (2016) relies on an experimental database containing 80% of the data used in its regression analysis for R134a, which were obtained in the same test bench of this work for tube diameters very close to this work ($D = 0.38$ to 2.3 mm) and same saturation temperatures of 31°C . Thus, it is speculated that the proximity of the experimental

conditions of both studies favors satisfactory predictions by the method of Kanizawa et al. (2016). Furthermore, the mean average deviation reported by Kanizawa et al. (2016) with respect to its database used in their regression analyses containing 2047 data points is only 11%, therefore close to the mean average deviation obtained from the comparison with the present database given in Tab. 6.2 (13.6%).

Table 6.2 – Statistical parameters resulting from the comparison of the experimental data and the corresponding predictions for the average HTC under transient heat loads

	Mean Absolute Deviation (%)	Standard Deviation (%)	Deviation < 20% (%)	Deviation < 30 % (%)
Lazarek and Black (1982)	16.2	7.1	65.3	100
Tran et al. (1996)	36.2	12.3	3.2	46.5
Thome et al. (2004)	26.2	32.9	44.4	58.6
Sun and Mishima (2009)	13.6	6.8	87.5	100
Li and Wu (2010)	18.6	12.5	57.4	82.9
Costa-Patry and Thome (2013)	43.4	35.7	4.6	16.9
Kim and Mudawar (2013)	18.5	10.8	80.8	100
Kanizawa et al. (2016)	13.6	6.1	88.2	100

Figure 6.28 – Comparison among the predicted and the experimental average heat transfer coefficients



The predictions by the method of Sun and Mishima (2009) were nearly as precise as those given by Kanizawa et al. (2016), resulting in the second best accuracy among the eight methods. Also, the methods of Kim and Mudawar (2013), Lazarek and Black (1982) and Li and Wu (2010) lead to satisfactory estimations, providing $\lambda_{30\%} > 80\%$. It is worth noting that the method of Lazarek and Black (1982) does not include results for R134a in the database used for the adjustment of its empirical constants (see Tab. 2.1), although this method showed good agreement with experimental results.

An analyses of Tabs. 2.1 and 6.2 reveals that from the five methods that were able to predict more than 80% of the data within $\pm 30\%$, two methods are based on the superposition of convective and nucleate boiling effects (Kim and Mudawar, 2013; Kanizawa et al., 2016) and three methods are based on the assumption that the dominant heat transfer mechanism is nucleate boiling (Lazarek and Black, 1982; Sun and Mishima, 2009; Li and Wu, 2010). The less accurate predictions of the average HTC were given by the correlation of Tran et al. (1996) and the mechanistic models of Thome et al. (2004) and Costa-Patry and Thome (2013). The correlation of Tran et al. (1996) exhibited a tendency of underestimating the average HTC for all conditions, as shown in Fig. 6.28. The method of Thome et al. (2004) provide $\lambda_{30\%} = 67\%$ with respect to its own database (used for adjusting the empirical constants), as indicated by Dupont et al. (2004). Hence, a value of $\lambda_{30\%} = 58.6\%$ for the experimental data of this work is in agreement with the accuracy of this method with respect to its own database. Costa-Patry and Thome (2013) reported a mean absolute deviation of only 28% with respect to its own database, while the mean absolute deviation of this method with respect to the experimental data of this study is much higher (43.4%).

The accuracy of Thome et al. (2004) method varies significantly with changes in the vapor quality, which lead to great standard deviation, as observed in Tab. 6.2. For $D = 0.5$ mm, the method of Thome et al. (2004) provides $\lambda_{20\%} = 100\%$ for a vapor quality of 8% while it under predicts the HTC up to -60% for vapor qualities of 40 and 60%. For $D = 1.1$ mm, the method of Thome et al. (2004) overestimate the HTC by +60% for 8% vapor quality, while for vapor qualities of 40 and 60%, its predictions are within the range of $\pm 15\%$ of the experimental data of this study. It was observed that the method of Thome et al. (2004) always predicts a decrement of the HTC with increasing vapor quality while the experimental data suggests that the average HTC is almost constant with respect to the vapor quality. On the other hand, according to the experimental results for $D = 0.5$ mm, the HTC increases with increasing vapor quality (see Fig. 6.19).

Based on the present analysis, it is concluded that the method of Thome et al. (2004) does not capture correctly the heat transfer coefficient trends with respect to the vapor quality. Moreover, although the method of Thome et al. (2004) considers a three-zone approach (liquid slug, elongated bubble and dry zone) to model the time-averaged heat transfer coefficient, this model relies on experimental data for annular flow to adjust its empirical constants, hence other effects not pertinent to slug flow are expected to be absorbed by the empirical constants. Likewise, because this model relies on experimental data for multi-channels, the inherent interaction among the channels is also expected to be captured by the empirical constants.

Similarly to the method of Thome et al. (2004), the method of Costa-Patry and Thome (2013) incorrectly predicts the HTC behavior with respect to the vapor quality, explaining its great standard deviation given in Tab. 6.2. In fact, the method of Costa-Patry and Thome (2013) relies on the method of Thome et al. (2004) to estimate the heat transfer coefficient for isolated/coalescing bubbles flow pattern and the method of Cioncolini and Thome (2011) for estimating the HTC for annular flow. A smooth transition zone was included in the method of Costa-Patry and Thome (2013). The behavior of the estimated heat transfer coefficient by Costa-Patry and Thome (2013) correlation with respect to the heat transfer coefficient is a “V” shaped curve. In this method, the heat transfer coefficient monotonically decreases with vapor quality to a minimum corresponding to the transition between isolated and coalescing bubbles and then its value rises with additional increments of vapor quality as annular flow is established. The main trends of the experimental data reported in Fig. 6.19 (a) and 6.19 (b) does not present a “V” shaped curve as proposed by Costa-Patry and Thome (2013), what explains the low accuracy of this method to predict the present experimental results.

In general, satisfactory agreement was noted for the average heat transfer coefficient for the methods based on the superposition of convective and nucleate boiling effects and also for the methods based on the assumption that nucleate boiling is the dominant mechanism, with exception of the correlation of Tran et al. (1996). The mechanistic models of Thome et al. (2004), and Costa-Patry and Thome (2013) were not able to capture the trends of the heat transfer coefficient variations with vapor quality, resulting in the high mean absolute deviation and high standard deviation seen in Tab. 6.2. Considering that five of the eight methods analyzed in this section lead to satisfactory predictions (80% of the data within $\pm 30\%$), it is concluded that the methods developed for steady heating can be employed to estimate the average HTC under transient and periodic heat loads. The methods based on the superposition of effects (Kim and Mudawar, 2013; Kanizawa et al., 2016) are recommended over the methods

based only on nucleate boiling effects, as they are expected to be accurate for a wider range of conditions.

6.5.2. Wall Superheat Temperature Amplitude

In the analysis of the wall superheat temperature amplitude, it is important to note that the experimental data is biased towards attenuated oscillations. This occurs because of the thermal inertia effects inherent to experimental setup adopted in the present study, as discussed in Section 5.8. A compensation of the wall superheat temperature signal for the “low-pass filter effect” caused by the thermal inertia of the tube walls and thermocouple hot junction was attempted, but unfortunately the signal to noise ratio was not great enough to lead reasonable results. Consequently, the data for the wall superheat temperature amplitude presented here are not compensated. If the experimental data was compensated, larger values of ΔT_w amplitude were expected, particularly for the data under the highest heating pulses frequency contemplated in this study (2 Hz), which exhibited the greatest influence of the thermal inertia effects related to the tube wall and thermocouple bead.

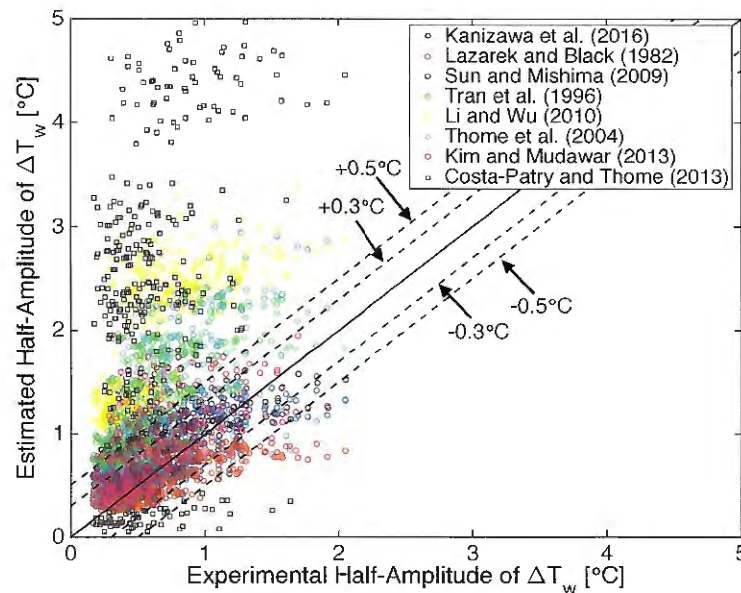
Table 6.3 presents the statistical parameters resulting from the comparison of the experimental ΔT_w half-amplitude and their respective predictions according to the methods from literature. Figure 6.29 depicts the experimental vs. estimated wall superheat temperature amplitudes for the entire database. According to Tab. 6.3 and as shown in Fig. 6.29, the majority of the methods over predicts the experimental data due to positive mean deviations. The influence of the thermal inertia effects on the measured wall superheat temperature can partially explain why most methods over predicted the ΔT_w , but it is not sufficient alone to explain the observed errors of ΔT_w amplitude up to 500% for some data points.

According to Tab. 6.3, the methods of Lazarek and Black (1982), Kanizawa et al. (2016), Kim and Mudawar (2013) and Sun and Mishima (2009) are able to predict more than 84% of the database for the ΔT_w half-amplitude within an error band of $\pm 0.5^\circ\text{C}$. On the other hand, the methods of Tran et al. (1996), Li and Wu (2010) and Costa-Patry and Thome (2013) exhibited unsatisfactory performance, predicting less than 30% of the results within a deviation range of $\pm 0.5^\circ\text{C}$.

Table 6.3– Statistical parameters resulting from the comparison of the predictions and experimental results for the wall superheat temperature half-amplitude

	Mean Absolute Deviation (°C)	Standard Deviation (°C)	Deviation < 0.3°C (%)	Deviation < 0.5°C (%)
Lazarek and Black (1982)	0.41	0.52	78.9%	92.1%
Tran et al. (1996)	1.46	0.75	10.2%	29.6%
Thome et al. (2004)	0.95	0.95	43.3%	60.6%
Sun and Mishima (2009)	0.57	0.57	62.3%	84.1%
Li and Wu (2010)	2.52	0.98	0.0%	0.7%
Costa-Patry and Thome (2013)	4.22	3.27	10.2%	18.1%
Kim and Mudawar (2013)	0.51	0.64	69.0%	85.7%
Kanizawa et al. (2016)	0.47	0.55	70.4%	88.7%

Figure 6.29 – Comparison of the predicted and the experimental wall superheat temperature half-amplitude for the entire database



To further investigate the cause of accuracy discrepancies among the methods of Tab. 6.3, the following consideration are made: during the tests the local pressure and vapor quality remained nearly constant at the hotspot central region and the only parameter changing significantly over the time was the local heat flux. This fact implies that the HTC transients are exclusively associated to the heat flux variations. Therefore, it is reasonable to assess the

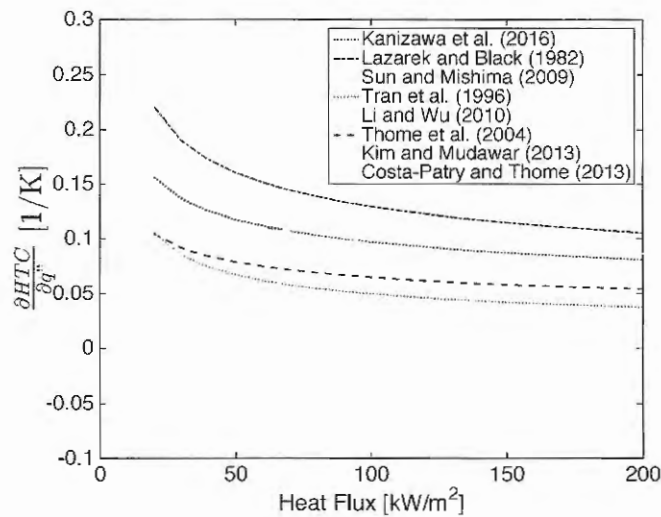
predicted sensitivity of the heat transfer coefficient to the heat flux variations to verify why some correlations are more accurate than others. The sensitivity (or the first partial derivative) of the heat transfer coefficient to heat flux changes is a useful parameter to characterize the level of self-enhancement effect exhibited by the flow boiling process. The hydrothermal mechanisms react to the increment/decrement of the local heat flux by increasing/decreasing the local HTC.

Figure 6.30 depicts the first partial derivative of the heat transfer coefficient with respect to the heat flux according to the eight methods listed in Tab. 6.3. According to this figure, the method of Lazarek and Black (1982) predicts the greatest sensitivity of the heat transfer coefficient to the heat flux variation. In agreement with this observation, the method of Lazarek and Black (1982) was the only one providing negative mean deviation, revealing that this method tends to overestimate the self-enhancing effect of the flow boiling mechanism. Consequently, this method underestimates the wall superheat temperature oscillations occurring during the experiments. This erroneous trend is also displayed in Fig. 6.29.

Figure 6.30 also reveals that the heat transfer coefficient sensitivity to the heat flux according to the methods of Kanizawa et al. (2016), Kim and Mudawar (2013) and Sun and Mishima (2009) are very close to each other for the range of heat flux evaluated in the present study (from 40 to 160 kW/m²). This result explains the similarity between the mean deviations among these three methods shown in Tab. 6.3. Because of their reasonable accuracy and the similarity of their predictions, the methods of Kanizawa et al. (2016), Kim and Mudawar (2013) and Sun and Mishima (2009) are considered in the present study as the best to estimate the wall superheat temperature amplitude, as they were able to capture the self-enhancing effect exhibited by the flow boiling mechanism with satisfactory precision.

Regarding the methods of Thome et al. (2004), Li and Wu (2010), Tran et al. (1996) and Costa-Patry and Thome (2013), the results shown in Tab. 6.3 indicate that these four methods over predict the wall superheat temperature amplitude, hence, these methods underestimate the self-enhancement effect of the flow boiling mechanism. Figure 6.30 confirms this hypothesis, demonstrating that these four methods present the lowest HTC sensitivity to the heat flux among the eight methods analyzed in this section. Moreover, the ranking from greatest to lowest heat transfer coefficient sensitivity from Fig 6.30 corresponds to the ranking from lowest to greatest mean deviations in Tab. 6.3.

Figure 6.30 – First partial derivative of the heat transfer coefficient with respect to the heat flux for the eight HTC methods, R134a at $T_{sat} = 31^\circ\text{C}$, $D = 0.5 \text{ mm}$, $G = 400 \text{ kg/m}^2\text{s}$ and $x = 60\%$



It is worth mentioning that the method of Costa-Patry and Thome (2013) does not predict any variations of the heat transfer coefficient with the heat flux fluctuations for annular flow, as shown in Fig. 6.30. This result contradicts the experimental observations of the present study and explains why this method leads to the greatest mean error of Tab. 6.3, as already mentioned. The method of Costa-Patry and Thome (2013) relies upon the model of Cioncolini and Thome (2011) for estimating the heat transfer coefficient under annular flow. The model of Cioncolini and Thome (2011) considers that the local Nusselt number is only a function of the dimensionless film thickness and the liquid Prandtl number. Hence, the method of Cioncolini and Thome (2011) does not include any dependency upon the heat flux because it only accounts for convective effects. Therefore, the explanation for the low accuracy of Costa-Patry and Thome (2013) under high vapor qualities should reside in the disregard of the contribution of nucleate boiling effects to the overall heat transfer. It is speculated that the nucleation effects should be significant under annular flow because the experimental data of this work revealed that the flow boiling self-enhancing effect of the refrigerant flow is still present under this flow pattern. This statement is corroborated by the work of Tibiriçá and Ribatski (2014), that observed active nucleation sites within the liquid film for annular flow for R134a, $G = 300 \text{ kg/m}^2\text{s}$ inside a $D = 0.4 \text{ mm}$ tube at saturation temperature of 31°C and heat flux of 70 kW/m^2 . Moreover, lower population of active nucleation cavities is expected to occur for smooth surfaces such as quartz when compared to stainless steel, hence, proper surface engineering is expected to improve the flow boiling self-enhancing effect.

6.6. Methodology for Estimating the Dynamic Behavior of Wall Superheat Temperature under Transient and Cyclical Heat Loads

The parametric analysis performed in Section 6.4 shed some light on how the transient behavior of the wall superheat temperature is affected by changes in the heating pulses characteristics (waveform, frequency, \bar{q}''_{hpot} and $\Delta q''_{hpot}$) and flow conditions (G , D , x). Additionally, the comparison of the experimental database of this study with prediction methods from literature in Section 6.5 revealed that some methods developed for steady-state heating conditions are suitable to be extrapolated for transient and cyclical heat loads, providing accurate predictions for the average heat transfer coefficient and the amplitude of ΔT_w . A thorough search of the relevant literature showed that, up to the present date, there are no methods for predicting ΔT_w under transient heat loads for flow boiling in microchannels. Therefore, in this section, a methodology for predicting the transient behavior of the ΔT_w is presented based on the results described in Sections 6.4 and 6.5.

6.6.1. Presentation of the Methodology

As the heat loads are cyclical, the wall superheat temperature is assumed to be composed of a mean and a fluctuating component. Therefore, ΔT_w can be written as follows:

$$\Delta T_w(t) = \overline{\Delta T_w} + \Delta T'_w(t) \quad (6.3)$$

where $\overline{\Delta T_w}$ is the mean wall superheat temperature and $\Delta T'_w$ is its fluctuating component.

To estimate the average wall superheat temperature, a method for predicting the average HTC needs to be employed. The method of Kanizawa et al. (2016) is recommended due to its reasonable accuracy, as demonstrated in Section 6.5.1. The average wall superheat temperature was shown to be independent of the heating pulses waveform, frequency and amplitude as found in Section 6.4. Thus, the time-averaged heat flux \bar{q}'' and the fluid time-averaged conditions (T_{sat} , G , D and x) are used for calculating the estimated $\overline{\Delta T_w}$ analogously to the steady-heating case.

The fluctuating component of the wall superheat temperature $\Delta T'_w(t)$ is modelled based on the following considerations:

- The modification of the nucleation effects magnitude is responsible for the self-enhancement effect exhibited by the flow boiling mechanism. Hence, $\Delta T'_w(t)$ is strongly linked to the heat flux oscillations $\Delta q''(t)$;

- The flow boiling reacts instantaneously to the variations of the heat load by increasing/decreasing the heat transfer coefficient as the heat load increases/decreases;

- $\Delta T'_w(t)$ is estimated by superposing the effects of the flow boiling mechanisms and the thermal inertia of the tube walls. The effects of the thermal inertia of tube walls are represented through a first-order lag system transfer function with known time-constant τ .

The flow boiling is considered to react instantaneously to variations of the heat load because the phenomena related to the nucleate boiling effects occur at a much smaller time scale than the heat pulses temporal variations, as discussed in Section 5.8. The fluctuation component of the wall superheat temperature related to flow boiling effects $\Delta T'_{wfb}$ is initially assumed to be a function of the saturation temperature, mass velocity, tube diameter, local vapor quality, average heat flux and heat flux amplitude, i.e. $\Delta T'_{wfb} = f(t, T_{sat}, G, D, x, q'')$. Expanding $\Delta T'_{wfb}$ according to a Taylor series and truncating at the first-order terms, it is found that:

$$\Delta T'_{wfb} = \frac{\partial \Delta T_w}{\partial T_{sat}} \Delta(T_{sat}) + \frac{\partial \Delta T_w}{\partial G} \Delta(G) + \frac{\partial \Delta T_w}{\partial x} \Delta(x) + \frac{\partial \Delta T_w}{\partial q''} \Delta(q'') \quad (6.4)$$

During the experiments, the only parameter changing significantly over the time was the local heat flux. Therefore, $\Delta(T_{sat}) = \Delta(G) = \Delta(x) = 0$. For cyclical heat loads $\Delta(q'') = \Delta q''$. The arithmetic simplification of Eq. (6.4) results in the following expression:

$$\Delta T'_{wfb}(t) = \frac{\partial \Delta T_w}{\partial q''} \Delta q''(t) \quad (6.5)$$

The expression for estimating $\Delta T'_{wfb}$ corroborates the experimental observations because it captures the doubling of wall superheat temperature amplitude of oscillation when the heating pulses amplitude is doubled, as previously shown in Fig. 6.10. From a dimensional analysis, the term $\frac{\partial \Delta T_w}{\partial q''}$ can be interpreted as the inverse of the heat transfer coefficient (or the thermal resistance) pertinent to the fluctuating component, hence $\frac{\partial \Delta T_w}{\partial q''} = \frac{1}{\alpha'}$.

The boiling curves estimated according to the method of Kanizawa et al. (2016) were able to capture the reduction of ΔT_w oscillations with the increment of time-averaged heat flux and the improvement of ΔT_w oscillations with increasing the mass velocity and vapor quality

(see Section 6.4). Therefore, it is reasonable to use the method of Kanizawa et al. (2016) for estimating $\frac{\partial \Delta T_w}{\partial q''}$, as this method is able to reproduce the main trends of the data.

The value of $\frac{\partial \Delta T_w}{\partial q''}$ is estimated based on the first partial derivative of the boiling curve calculated according to the method of Kanizawa et al. (2016). Because the value of $\frac{\partial \Delta T_w}{\partial q''}$ changes over the interval of q'' ($[q''_{min}, q''_{max}]$), an average value is adopted. Therefore, $\frac{\partial \Delta T_w}{\partial q''}$ is estimated for the average heat flux \bar{q}'' , as schematically illustrated in Fig. 6.31. A central finite difference scheme is chosen to calculate $\frac{\partial \Delta T_w}{\partial q''}$, thus:

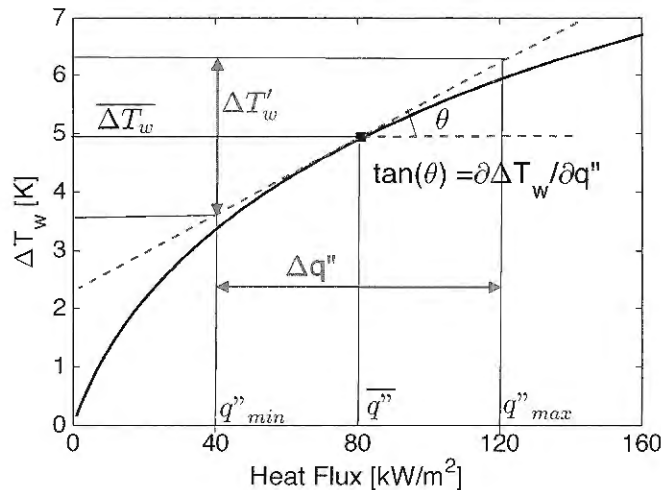
$$\frac{\partial \Delta T_w}{\partial q''} = \frac{1}{\alpha'} = \frac{\Delta T_w(T_{sat}, G, D, x, \bar{q}'' + \delta q'') - \Delta T_w(T_{sat}, G, D, x, \bar{q}'' - \delta q'')}{2\delta q''} \quad (6.6)$$

where $\delta q''$ is an infinitesimal increment of the heat flux

At this point, we have an expression that relates $\Delta T'_{w_{fb}}(t)$ to the $\Delta q''(t)$ by a constant factor, as follows:

$$\Delta T'_{w_{fb}}(t) = \frac{1}{\alpha'} \Delta q''(t) \quad (6.7)$$

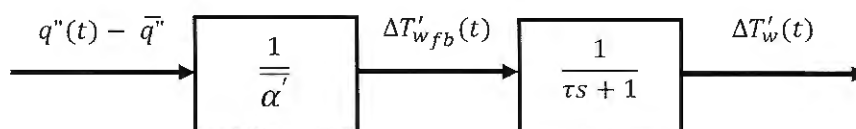
Figure 6.31 – Schematic illustration of the estimation of the thermal resistance related to the $\Delta T'_w$ from the boiling curve



The effect of the tube thermal inertia is accounted by considering that $\Delta T'_{w_{fb}}(t)$ is the input to a transfer function $\frac{1}{\tau s + 1}$ and the output signal is the final form of $\Delta T'_w(t)$. Therefore, the

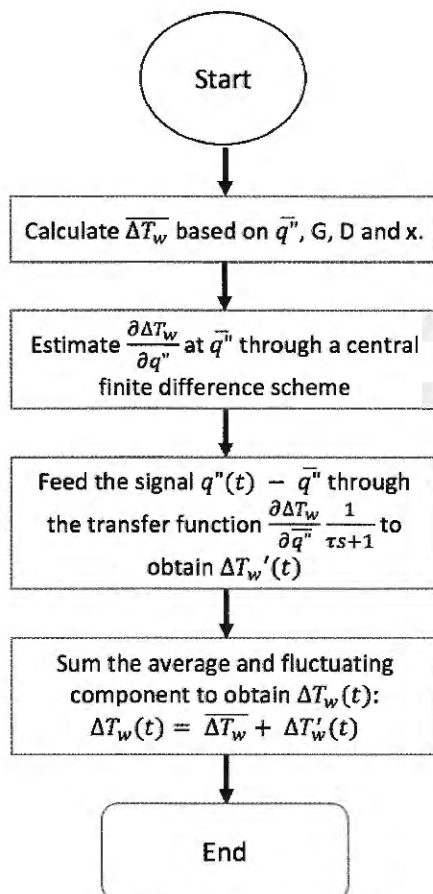
block diagram of Fig. 6.32 represents the procedure for estimating the $\Delta T'_w(t)$ considering the superposition of flow boiling effects and the thermal inertia of the tube walls.

Figure 6.32 – Block diagram illustrating the superposition of the effects of the flow boiling mechanisms and the thermal inertia of the tube walls for estimating the fluctuations of wall superheat temperature for transient heat loads



Finally, $\Delta T_w(t)$ is obtained by summing the fluctuating component $\Delta T'_w(t)$ to the estimated $\overline{\Delta T_w}$ (Eq. 6.3). Figure 6.33 summarizes the procedure for estimating $\Delta T_w(t)$.

Figure 6.33 – Summary of the methodology for estimating the wall superheat temperature dynamic behavior under transient and cyclical heat loads.



6.6.2. Validation of the Methodology

In this section, the validation of the methodology for estimating the ΔT_w behavior under transient and cyclical heat loads is performed. As previously mentioned, the ΔT_w oscillations are a combination of the flow boiling and thermal inertia effects. In this section, only results for $D = 0.5$ mm are presented because this tube diameter showed the lower influence of the thermal inertia effects (see Section 5.8), which permits to better evaluate if the methodology presented in this study is able to capture the ΔT_w fluctuations related to flow boiling mechanisms ($\Delta T'_{wfb}$).

Figures 6.34 (a), 6.34 (b) and 6.34 (c) shows the ΔT_w dynamic behavior for sinusoidal, square and saw tooth heating pulses when calculated through the use of experimental data as the boundary condition for estimating the HTC for every time instant (See Section 6.5.2) according to the method of Kanizawa et al. (2016), using the methodology proposed in this study and the experimental results, respectively. As seen in this figure, the shape of ΔT_w curves are closer to the experimental results for the estimatives based on the methodology proposed here. This occurs because, when the thermal inertia effects are included, the discontinuities of ΔT_w fluctuations are vanished.

Figure 6.34 – Comparison of the wall superheat temperature transient behavior for direct estimation through the use of experimental data for every time instant for estimating HTC (a), the methodology presented in this study (b) and experimental data (c) for $\tau = 180$ ms, R134a, $D = 0.5$ mm, $T_{sat} = 31^\circ\text{C}$, $G = 600$ kg/m²s, $\bar{x}_{hpot} = 40\%$, $\bar{q}''_{hpot} = 80$ kW/m², $\Delta q''_{hpot} = 40$ kW/m² and $f = 0.5$ Hz

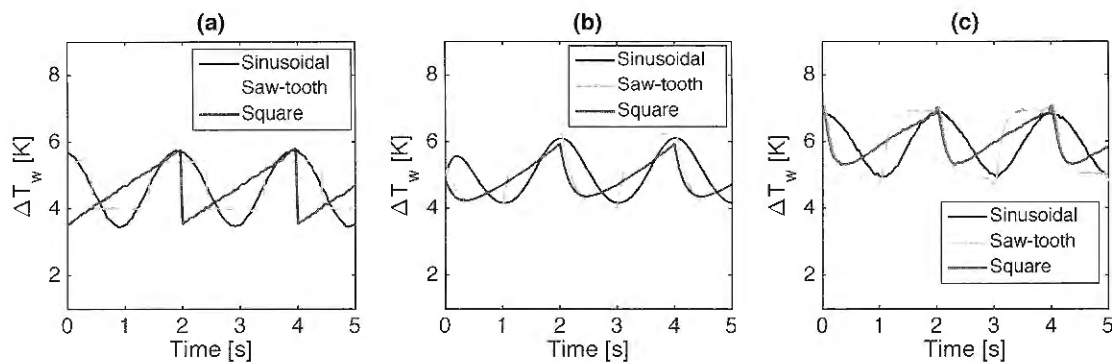


Figure 6.35 (a) shows the experimental data for ΔT_w and Fig. 6.35 (b) shows the estimated ΔT_w calculated through the procedure summarized in Fig. 6.33 and assuming $\tau = 180$ ms. The comparison of Figs. 6.35 (a) and 6.35 (b) reveals that the methodology proposed in this section was able to capture the differences of the ΔT_w curve shape according to the heat flux waveform. Moreover, the peaks of estimated ΔT_w occur at the same instant of the peaks of

experimental ΔT_w , showing that the method was also able to capture the time delay between the heat flux and wall superheat temperature signals. For the conditions of Fig. 6.35, the errors associated to the ΔT_w amplitude and mean value were found to be 0.14°C and 0.44°C , respectively.

Figure 6.35 – Experimental vs. estimated transient behaviors of the wall superheat temperature for $\tau = 180$ ms, R134a, $D = 0.5$ mm, $T_{sat} = 31^\circ\text{C}$, $G = 600$ kg/m²s, $\bar{x}_{hpot} = 40\%$, $\bar{q}''_{hpot} = 120$ kW/m², $\Delta q''_{hpot} = 40$ kW/m² and $f = 1$ Hz

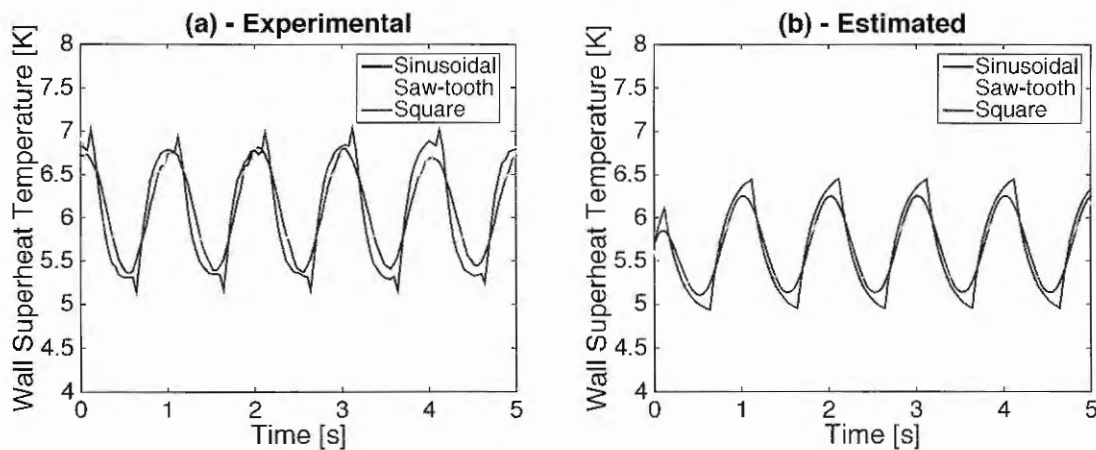


Figure 6.36 (a) and 6.36 (b) displays the variations in the experimental and estimated ΔT_w , respectively, when the mass velocity is increased from 400 to 600 kg/m²s. From this figure, it is observed that the estimated ΔT_w reproduces the reduction of the average ΔT_w but it underestimates its magnitude. Also, the amplitude of the estimated ΔT_w remained almost constant with the change of mass velocity, similarly to the experimental results of Fig. 6.36 (a). The amplitude of ΔT_w is practically insensitive to the variation of the mass velocity when this parameter is changed from 400 to 600 kg/m²s, as previously demonstrated in Fig. 6.26. For the conditions of Fig. 6.36, the errors associated to the ΔT_w amplitude and its mean value were found to be 0.01°C and 0.62°C , respectively.

Figure 6.37 (a) and 6.37 (b) shows the variations of the experimental and estimated ΔT_w , respectively, as the vapor quality is increased from 8 to 40% and then to 60%. It can be seen from this figure that the methodology proposed here is able to capture the increment of the amplitude of ΔT_w oscillations with increasing vapor quality. Moreover, the reduction of the average ΔT_w with increasing vapor quality is also reproduced in the estimated ΔT_w results.

Figure 6.36 – Experimental vs. estimated transient behaviors of the wall superheat temperature under saw tooth heating pulses for $\tau = 180$ ms, R134a, $D = 0.5$ mm, $T_{sat} = 31^\circ\text{C}$, $\bar{x}_{hpot} = 60\%$, $\bar{q}''_{hpot} = 120$ kW/m², $\Delta q''_{hpot} = 40$ kW/m² and $f = 1$ Hz

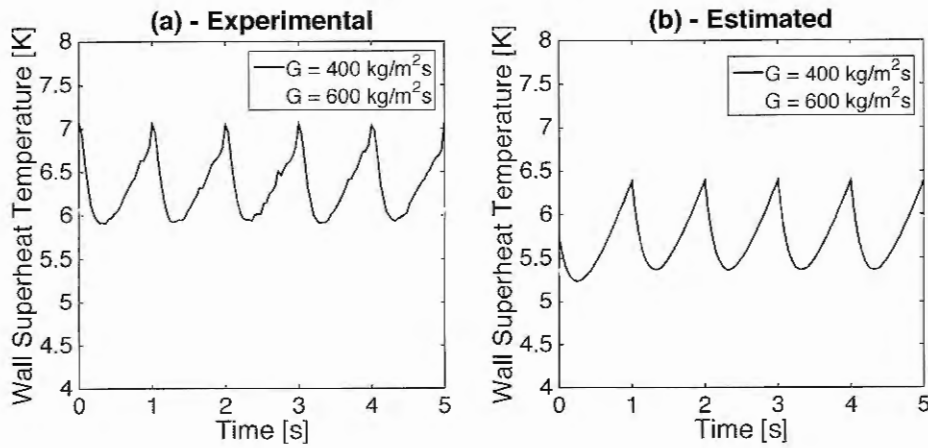
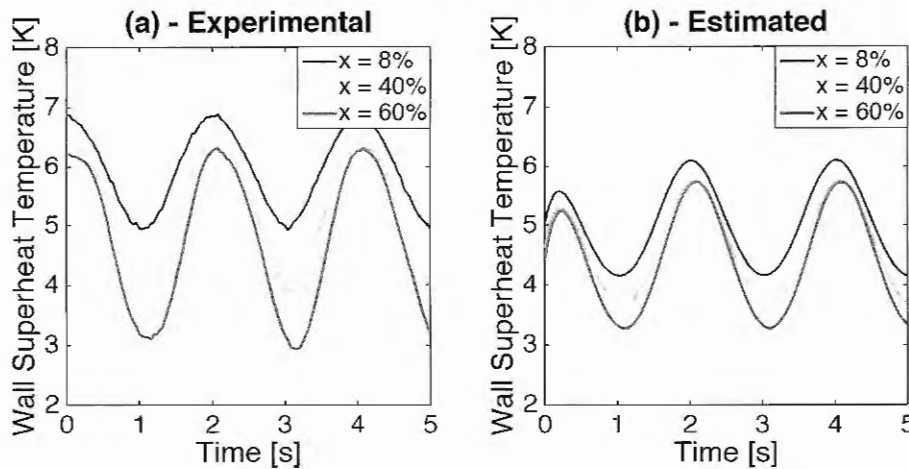


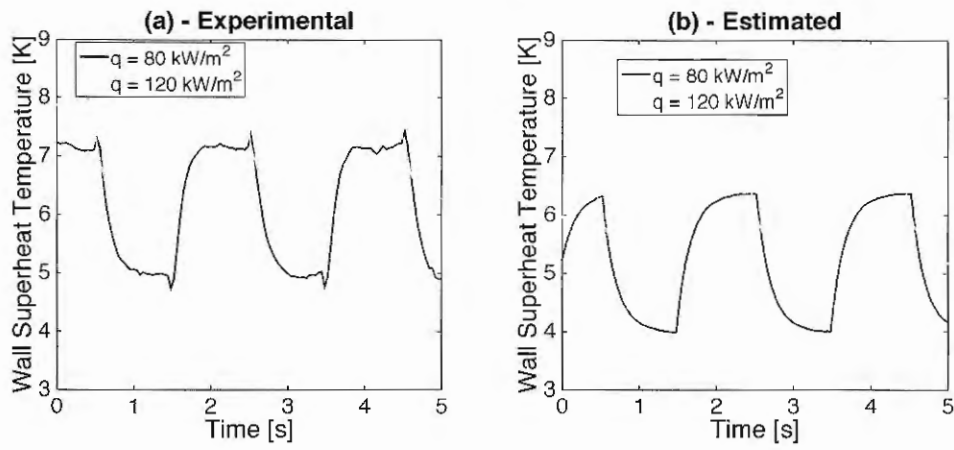
Figure 6.37 – Experimental vs. estimated transient behaviors of the wall superheat temperature under sinusoidal heating pulses for $\tau = 180$ ms, R134a, $D = 0.5$ mm, $T_{sat} = 31^\circ\text{C}$, $G = 600$ kg/m²s, $\bar{q}''_{hpot} = 80$ kW/m², $\Delta q''_{hpot} = 40$ kW/m² and $f = 0.5$ Hz.



Figures 6.38 (a) and 6.38 (b) shows the experimental and estimated ΔT_w , respectively, as the average heat flux is increased from 80 to 120 kW/m². From this figure, it can be seen that the estimated ΔT_w was able to capture the reduction of ΔT_w amplitude and the augmentation of the average ΔT_w with increasing heat flux.

The reasonable agreement of the estimated ΔT_w with the experimental data permits to conclude that the methodology presented in this section is able to capture the main trends of data when transient and cyclical heat loads are present during flow boiling inside small diameter channels.

Figure 6.38 – Experimental vs. estimated transient behaviors of the wall superheat temperature under square heating pulses for $\tau = 180$ ms, R134a, $D = 0.5$ mm, $T_{sat} = 31^\circ\text{C}$, $\bar{x}_{hpot} = 40\%$, $G = 400$ kg/m²s, $\Delta q''_{hpot} = 40$ kW/m² and $f = 0.5$ Hz.



7. CONCLUSIONS AND FUTURE WORK

In this chapter, the main conclusions drawn from the parametric analysis of Section 6.4 are presented and summarized. Also, the main findings from the assessment of flow boiling prediction methods to transient heating in Section 6.5 are indicated. At the end, a list of suggestions and ideas for future works is presented.

7.1. Conclusions

As general conclusion, the experimental results revealed that, under fixed fluid conditions (saturation temperature, mass velocity, tube diameter and vapor quality) and time-averaged heat flux, a first-order lag system transfer function accurately represents the relationship between the transient behavior of the heat flux (input) and the ΔT_w (output). The parametric analysis of the effects of heat flux waveform, frequency and half-amplitude on the behavior of the ΔT_w revealed that the conclusions drawn from the experimental results can be also captured by a first-order system time response.

The lack of interdependence between the average ΔT_w and the heat flux waveform, frequency and half-amplitude is correctly predicted by a first-order system analysis. Also, the ranking of greatest to lowest ΔT_w amplitude according to the waveform type and magnitude of the temperature oscillations damping due to thermal inertia are correctly captured by the first-order model. The linearity between the heat flux half-amplitude and the amplitude of ΔT_w is also reflected in the first-order system time response.

The boiling curves, based on the method of Kanizawa et al. (2016) for flow boiling in small diameter channels, showed to be a valuable tool to predict the experimental data trends. This method captured the effects of the time-averaged heat flux, vapor quality and mass velocity on the behavior of the ΔT_w amplitude. The reduction of ΔT_w oscillations with the increment of time-averaged heat flux and the improvement of ΔT_w oscillations with increasing the mass velocity and vapor quality are captured by the method of Kanizawa et al. (2016).

To sum up, the following specific conclusions were drawn based on the parametric analysis of the transient behavior of the ΔT_w :

- The heating pulses waveform did not affect significantly the average ΔT_w , independently of the tube diameter. The following ranking of waveforms from greatest to

lowest amplitude of ΔT_w was observed: square, sinusoidal and saw tooth waveforms. This ranking was found to be closely linked to the amplitude of the lowest heat flux signal harmonic;

- The heating pulses half-amplitude does not influence the average ΔT_w . Doubling the heat flux half-amplitude approximately doubled the amplitude of the ΔT_w , suggesting that a linear relationship between heat flux and ΔT_w amplitude might hold true for the tested conditions, independently of the tube diameter. Further tests are necessary to confirm this premise as only two half-amplitudes were covered in the present study;

- The average ΔT_w was found almost independent of the heating pulses frequency. Also, the amplitude of ΔT_w decreased as the heating pulses frequency was increased. The reduction of the magnitude of the temperature oscillations is attributed to the thermal inertia of the tube wall and thermocouple bead, as no evidence of significant variations of the flow boiling behavior was noted;

- The average ΔT_w increases and the amplitude of ΔT_w oscillations decreases with increasing time-average heat flux. These two behaviors are corroborated by an analysis of boiling curves based on the method of Kanizawa et al. (2016). The reduction of ΔT_w amplitude with increasing time-average heat flux was attributed to the enhancement of nucleate boiling effects. It is probable that the nucleate boiling effects are enhanced for higher heat fluxes because a larger number of nucleation sites are active;

- The vapor quality influences the average ΔT_w and seems to affect the amplitude of ΔT_w . The trends of the data for the average ΔT_w were correctly captured by the method of Kanizawa et al. (2016). Although most of the variations were within the uncertainties, the amplitude of ΔT_w oscillations seems to increase monotonically with increasing vapor quality, independently of the tube diameter. It is speculated that, because the increment of vapor quality raises the two-phase flow velocity, the suppression of nucleation effects is enhanced and the self-enhancing effect is diminished, explaining the improvement of ΔT_w level of fluctuations with increasing vapor quality. The increment of the level of ΔT_w was also corroborated by an analysis of the boiling curves based on the method of Kanizawa et al. (2016);

- The increment of the mass velocity reduces the average ΔT_w and increases the amplitude of ΔT_w . The reduction of average ΔT_w was attributed to the enhancement of convective effects with increasing mass velocity. Most of the results indicated marginal variations of ΔT_w amplitude with increasing mass velocity. Nevertheless, it seems that the ΔT_w amplitude increases with increasing mass velocity, as most of the data indicated larger ΔT_w for

the greatest mass velocity. It is speculated that the increment of the two-phase flow velocity enhances the suppression of the nucleation effects, diminishing the self-enhancing effect and improving marginally the level of fluctuations of ΔT_w . This behavior coincides with the boiling curves based on the method of Kanizawa et al. (2016).

Also, the comparison of the experimental database with the predictions through the methods of Tab. 2.1, all developed based on experimental data for steady heating, revealed that some methods lead to satisfactory estimative when extrapolated to transient heat loads conditions. Table 6.2 indicates that the methods of Lazarek and Black (1982), Kanizawa et al. (2016), Kim and Mudawar (2013) and Sun and Mishima (2009) are able to predict 100% of the average heat transfer coefficient data within an error range of $\pm 30\%$. These same four methods provided the most accurate results for the wall superheat temperature half-amplitude, predicting 84% of the database within an error band of $\pm 0.5^\circ\text{C}$, as demonstrated in Tab. 6.3. The reason why some methods perform better than others to predict the amplitude of temperature fluctuations seems to be linked to the heat transfer coefficient sensitivity to the heat flux. This observation suggests that the self-enhancing effect exhibited by the flow boiling mechanism inside mini and microchannels is associated to nucleate boiling mechanisms.

7.2. Future Work

The following recommendations are made to future studies pertinent to transient heating during flow boiling in microchannels:

- Perform transient heating experiments using different refrigerants such as R600a (high pressure) and R245fa (low pressure), as only R134a was contemplated in this study. The magnitude of nucleate boiling effects increases for increasing reduced pressure of the refrigerant. Therefore, it would be interesting to perform transient heating tests using two refrigerants exhibiting high and low reduced pressures as this would permit to verify the influence of the intensification of nucleate boiling effects at the self-enhancing cooling effect exhibited by flow boiling;
- Test a larger number of heating pulses half-amplitude ($\Delta q''_{hpot}$), as only two values of $\Delta q''_{hpot}$ (20 and 40 kW/m²) were covered in this work. An experimental database with a larger number of $\Delta q''_{hpot}$ conditions would permit to verify the validity of assuming a linear proportionality between the ΔT_w and heat flux oscillations over a wider range of conditions;

- Test a larger number of heating pulses frequency, as only values up to 2 Hz were contemplated in this study. To accomplish this, the thermal inertia effects of the test section needs to be minimized, e.g. use channels with thin walls and made out of materials exhibiting high thermal diffusivity (silicon, copper). The use of thermography for monitoring the wall temperature is recommended over thermocouples due to its faster time response and spatial resolution;

- Evaluate the self-enhancing cooling effect exhibited by flow boiling in microchannels with surface modification, as to provide the theoretical basis for designing enhanced surfaces for dissipating transient heat loads. A first idea is to compare the transient behavior of ΔT_w for similar tubes without any surface modification and with micro/nanostructured surfaces. It would be also interesting to evaluate the influence of surface roughness in the self-enhancing cooling effect;

- Evaluate the self-enhancing cooling effect exhibited by flow boiling for small diameter channels with non-circular cross-sectional geometries such as rectangular (low and high aspect ratios) and triangular, and compare the results to circular channels. Sharp corners are expected to favor bubble nucleation in the vertices due to the high degree of superheating of the fluid in this region. It would be also interesting to test circular channels with diameter smaller than 0.5 mm to evaluate the effects of more severe bubble confinement in the heat transfer coefficient during heating pulses;

- Compare the self-enhancing exhibited by flow boiling in microchannels with other cooling technologies such as spray cooling and microgaps to determine which cooling method is best for minimizing wall temperature oscillations under transient heat loads.

REFERENCES

- Abernethy, R. B. (1973). *JW Thompson, Jr., Handbook, Uncertainty in Gas Turbine Measurements*. Report AEDC-TR-73-5, Arnold Engineering Development Center, Arnold Air Force Station.
- Adams, T. M., Dowling, M. F., Abdel-Khalik, S. I., & Jeter, S. M. (1999). Applicability of traditional turbulent single-phase forced convection correlations to non-circular microchannels. *International Journal of Heat and Mass Transfer*, 42(23), 4411-4415.
- Agostini, B., Fabbri, M., Park, J. E., Wojtan, L., Thome, J. R., & Michel, B. (2007). State of the art of high heat flux cooling technologies. *Heat Transfer Engineering*, 28(4), 258-281.
- Alam, T., Lee, P. S., Yap, C. R., & Jin, L. (2012). Experimental investigation of local flow boiling heat transfer and pressure drop characteristics in microgap channel. *International Journal of Multiphase Flow*, 42, 164-174.
- Álvarez-Briceño, R., Kanizawa, F. T., Ribatski, G., & de Oliveira, L. P. (2017). Updated results on hydrodynamic mass and damping estimations in tube bundles under two-phase crossflow. *International Journal of Multiphase Flow*, 89, 150-162.
- Arcanjo, A. A., Tibiriçá, C. B., & Ribatski, G. (2010). Evaluation of flow patterns and elongated bubble characteristics during the flow boiling of halocarbon refrigerants in a micro-scale channel. *Experimental Thermal and Fluid Science*, 34(6), 766-775.
- Bahaidarah, H. M., Baloch, A. A., & Gandhidasan, P. (2016). Uniform cooling of photovoltaic panels: a review. *Renewable and Sustainable Energy Reviews*, 57, 1520-1544.
- Baig, H., Heasman, K. C., & Mallick, T. K. (2012). Non-uniform illumination in concentrating solar cells. *Renewable and Sustainable Energy Reviews*, 16(8), 5890-5909.
- Bell, I. H., Wronski, J., Quoilin, S., & Lemort, V. (2014). Pure and pseudo-pure fluid thermophysical property evaluation and the open-source thermophysical property library CoolProp. *Industrial & engineering chemistry research*, 53(6), 2498-2508.
- Benda, V., Gowar, J., & Grant, D. A. (1999). *Discrete and Integrated Power Semiconductor Devices: Theory and Applications*. John Wiley & Sons.
- Bogojevic, D., Sefiane, K., Walton, A. J., Lin, H., Cummins, G., Kenning, D. B. R., & Karayiannis, T. G. (2011). Experimental investigation of non-uniform heating effect on flow boiling instabilities in a microchannel-based heat sink. *International Journal of Thermal Sciences*, 50(3), 309-324.
- Bradley, D., & Matthews, K. J. (1968). Measurement of high gas temperatures with fine wire thermocouples. *Journal of Mechanical Engineering Science*, 10(4), 299-305.
- Brauner, N., & Maron, D. M. (1992). Flow pattern transitions in two-phase liquid-liquid flow in horizontal tubes. *International Journal of Multiphase Flow*, 18(1), 123-140.

- Brunschwiler, T., Rothuizen, H., Fabbri, M., Kloter, U., Michel, B., Bezama, R. J., & Natarajan, G. (2006, May). Direct liquid jet-impingement cooling with micron-sized nozzle array and distributed return architecture. In *Thermal and Thermomechanical Phenomena in Electronics Systems, 2006. IThERM'06. The Tenth Intersociety Conference on* (pp. 196-203). IEEE.
- Chen, G., & Cheng, P. (2009). Nucleate and film boiling on a microheater under pulse heating in a microchannel. *International Communications in Heat and Mass Transfer*, 36(5), 391-396.
- Chen, J. C. (1966). Correlation for boiling heat transfer to saturated fluids in convective flow. *Industrial & engineering chemistry process design and development*, 5(3), 322-329.
- Cheng, L., & Xia, G. (2017). Fundamental issues, mechanisms and models of flow boiling heat transfer in microscale channels. *International Journal of Heat and Mass Transfer*, 108, 97-127.
- Cheng, L., Ribatski, G., & Thome, J. R. (2008). Two-phase flow patterns and flow-pattern maps: fundamentals and applications. *Applied Mechanics Reviews*, 61(5), 050802.
- Chisholm, D. (1967). A theoretical basis for the Lockhart-Martinelli correlation for two-phase flow. *International Journal of Heat and Mass Transfer*, 10(12), 1767-1778.
- Cho, E. S., Choi, J. W., Yoon, J. S., & Kim, M. S. (2010). Experimental study on microchannel heat sinks considering mass flow distribution with non-uniform heat flux conditions. *International Journal of Heat and Mass Transfer*, 53(9), 2159-2168.
- Churchill, S. W. (1977). Friction-factor equation spans all fluid-flow regimes. *Chemical engineering*, 84(24), 91-92.
- Cicchitti, A., Lombardi, C., Silvestri, M., & Soldaini, G. (1960). Zavattarelli," Two-Phase Cooling Experiments-Pressure Drop, Heat Transfer, and Burnout Measurements," *Energia Nucleare*, 7(6).
- Cioncolini, A., & Thome, J. R. (2011). Algebraic turbulence modeling in adiabatic and evaporating annular two-phase flow. *International Journal of Heat and Fluid Flow*, 32(4), 805-817.
- Collier, J. G., & Thome, J. R. (1994). *Convective boiling and condensation*. Clarendon Press.
- Costa-Patry, E., & Thome, J. R. (2013). Flow pattern-based flow boiling heat transfer model for microchannels. *International Journal of Refrigeration*, 36(2), 414-420.
- Costa-Patry, E., Nebuloni, S., Olivier, J., & Thome, J. R. (2012). On-Chip Two-Phase Cooling with Refrigerant 85 μ m-Wide Multi-Microchannel Evaporator Under Hot-Spot Conditions. *IEEE Transactions on Components, Packaging and Manufacturing Technology*, 2(2), 311-320.

- Dittus, F. W., & Boelter, L. M. K. (1930). University of California publications on engineering. *University of California publications in Engineering*, 2, 371.
- Feng, S. S., Kuang, J. J., Lu, T. J., & Ichimiya, K. (2015). Heat transfer and pressure drop characteristics of finned metal foam heat sinks under uniform impinging flow. *Journal of Electronic Packaging*, 137(2), 021014.
- Friedel, L. (1979). Improved friction pressure drop correlations for horizontal and vertical two-phase pipe flow. In *European two-phase group meeting, Ispra, Italy*.
- Gnielinski, V. (1976). New equations for heat and mass transfer in turbulent pipe and channel flow. *Int. Chem. Eng.*, 16(2), 359-368.
- Grønnerud, R. (1972). Investigation of liquid hold-up, flow-resistance and heat transfer in circulation type evaporators, part IV: two-phase flow resistance in boiling refrigerants. *Bull. De l'Inst. Du Froid, Annexe, 1*.
- Hamann, H. F., Weger, A., Lacey, J. A., Hu, Z., Bose, P., Cohen, E., & Wakil, J. (2007). Hotspot-limited microprocessors: Direct temperature and power distribution measurements. *IEEE Journal of Solid-State Circuits*, 42(1), 56-65.
- Hetsroni, G., Gurevich, M., & Rozenblit, R. (2006). Sintered porous medium heat sink for cooling of high-power mini-devices. *International Journal of Heat and Fluid Flow*, 27(2), 259-266.
- Huang, H., Borhani, N., & Thome, J. R. (2016). Thermal Response of Multi-Microchannel Evaporators During Flow Boiling of Refrigerants Under Transient Heat Loads With Flow Visualization. *Journal of Electronic Packaging*, 138(3), 031004.
- Ishii, M., & Hibiki, T. (2010). *Thermo-fluid dynamics of two-phase flow*. Springer Science & Business Media.
- Jones Jr, O. C., & Zuber, N. (1974). Statistical methods for measurement and analysis in two-phase flow. In *Heat transfer, 1974. Vol. 4*.
- Kalani, A., & Kandlikar, S. G. (2016, July). Heat Dissipation Beyond 1 kW/cm² with Low Pressure Drop and High Heat Transfer Coefficient for Flow Boiling Using Open Microchannels With Tapered Manifold. In *ASME 2016 14th International Conference on Nanochannels, Microchannels, and Minichannels*.
- Kandlikar, S. G. (2005). High flux heat removal with microchannels—a roadmap of challenges and opportunities. *Heat Transfer Engineering*, 26(8), 5-14.
- Kandlikar, S. G., & Grande, W. J. (2003). Evolution of Microchannel Flow Passages--Thermohydraulic Performance and Fabrication Technology. *Heat transfer engineering*, 24(1), 3-17.
- Kanizawa, F. T., & Ribatski, G. (2016). Void fraction predictive method based on the minimum kinetic energy. *Journal of the Brazilian Society of Mechanical Sciences and Engineering*, 38(1), 209-225.

- Kanizawa, F. T., Tibiriçá, C. B., & Ribatski, G. (2016). Heat transfer during convective boiling inside microchannels. *International Journal of Heat and Mass Transfer*, *93*, 566-583.
- Kew, P. A., & Cornwell, K. (1997). Correlations for the prediction of boiling heat transfer in small-diameter channels. *Applied Thermal Engineering*, *17*(8), 705-715.
- Kim, S. M., & Mudawar, I. (2013). Universal approach to predicting saturated flow boiling heat transfer in mini/micro-channels—Part II. Two-phase heat transfer coefficient. *International Journal of Heat and Mass Transfer*, *64*, 1239-1256.
- Kim, Y. J., Joshi, Y. K., Fedorov, A. G., Lee, Y. J., & Lim, S. K. (2010). Thermal characterization of interlayer microfluidic cooling of three-dimensional integrated circuits with non-uniform heat flux. *Journal of Heat Transfer*, *132*(4), 041009.
- Koo, J. M., Jiang, L., Bari, A., Zhang, L., Wang, E., Kenny, T. W., Santiago, J. G., & Goodson, K. E. (2002). Convective boiling in microchannel heat sinks with spatially-varying heat generation. In *Thermal and Thermomechanical Phenomena in Electronic Systems, 2002. ITherm 2002. The Eighth Intersociety Conference on* (pp. 341-346). IEEE.
- Lazarek, G. M., & Black, S. H. (1982). Evaporative heat transfer, pressure drop and critical heat flux in a small vertical tube with R-113. *International Journal of Heat and Mass Transfer*, *25*(7), 945-960.
- Lee, Y. J., Lee, P. S., & Chou, S. K. (2013). Hotspot mitigating with obliquely finned microchannel heat sink—an experimental study. *IEEE Transactions on components, packaging and manufacturing technology*, *3*(8), 1332-1341.
- Li, W., & Wu, Z. (2010). A general correlation for evaporative heat transfer in micro/mini-channels. *International Journal of Heat and Mass Transfer*, *53*(9), 1778-1787.
- Marzoa, M. G., Ribatski, G., & Thome, J. R. (2016). Experimental flow boiling heat transfer in a small polyimide channel. *Applied Thermal Engineering*, *103*, 1324-1338.
- McAdams, W. H. (1949). Vaporization inside horizontal tubes-II Benzene-oil mixtures. *Trans. ASME*, *39*, 39-48.
- Mehendale, S. S., Jacobi, A. M., & Shah, R. K. (2000). Fluid flow and heat transfer at micro- and meso-scales with application to heat exchanger design. *Applied Mechanics Reviews*, *53*(7), 175-194.
- Miler, J. L., Flynn, R., Refai-Ahmed, G., Touzelbaev, M., David, M., Steinbrenner, J., & Goodson, K. E. (2009, January). Effects of transient heating on two-phase flow response in microchannel heat exchangers. In *Proceedings of the ASME 2009 InterPACK Conference, San Francisco, CA*.
- Moffat, R. J. (1988). Describing the uncertainties in experimental results. *Experimental thermal and fluid science*, *1*(1), 3-17.

- Mudawar, I. (2013). Recent advances in high-flux, two-phase thermal management. *Journal of Thermal Science and Engineering Applications*, 5(2), 021012.
- Müller-Steinhagen, H., & Heck, K. (1986). A simple friction pressure drop correlation for two-phase flow in pipes. *Chemical Engineering and Processing: Process Intensification*, 20(6), 297-308.
- Ong, C. L., & Thome, J. R. (2011). Macro-to-microchannel transition in two-phase flow: Part 2—Flow boiling heat transfer and critical heat flux. *Experimental thermal and fluid science*, 35(6), 873-886.
- Petukhov, B. S. (1970). Heat transfer and friction in turbulent pipe flow with variable physical properties. *Advances in heat transfer*, 6, 503-564.
- Pfahnl, A. C., Lienhard, J. H., & Slocum, A. H. (1999). *Thermal management and control in testing packaged integrated circuit (IC) devices* (No. 1999-01-2723). SAE Technical Paper.
- Revellin, R., Quibén, J. M., Bonjour, J., & Thome, J. R. (2008). Effect of local hot spots on the maximum dissipation rates during flow boiling in a microchannel. *IEEE Transactions on Components and Packaging Technologies*, 31(2), 407-416.
- Ritchey, S. N., Weibel, J. A., & Garimella, S. V. (2014). Local measurement of flow boiling heat transfer in an array of non-uniformly heated microchannels. *International Journal of Heat and Mass Transfer*, 71, 206-216.
- Royne, A., Dey, C. J., & Mills, D. R. (2005). Cooling of photovoltaic cells under concentrated illumination: a critical review. *Solar energy materials and solar cells*, 86(4), 451-483.
- Sempértegui-Tapia, D. F., & Ribatski, G. (2017). Two-phase frictional pressure drop in horizontal micro-scale channels: experimental data analysis and prediction method development. *International Journal of Refrigeration*, 79, 143-163.
- Sempertegui-Tapia, D., De Oliveira Alves, J., & Ribatski, G. (2013). Two-phase flow characteristics during convective boiling of halocarbon refrigerants inside horizontal small-diameter tubes. *Heat Transfer Engineering*, 34(13), 1073-1087.
- Sharma, C. S., Tiwari, M. K., Zimmermann, S., Brunschwiler, T., Schlottig, G., Michel, B., & Poulidakos, D. (2015). Energy efficient hotspot-targeted embedded liquid cooling of electronics. *Applied Energy*, 138, 414-422.
- Sieder, E. N., & Tate, G. E. (1936). Heat transfer and pressure drop of liquids in tubes. *Industrial & Engineering Chemistry*, 28(12), 1429-1435.
- Stephan, K., & Abdelsalam, M. (1980). Heat-transfer correlations for natural convection boiling. *International Journal of Heat and Mass Transfer*, 23(1), 73-87.
- Sun, L., & Mishima, K. (2009). An evaluation of prediction methods for saturated flow boiling heat transfer in mini-channels. *International Journal of Heat and Mass Transfer*, 52(23), 5323-5329.

- Sung, M. K., & Mudawar, I. (2006). Experimental and numerical investigation of single-phase heat transfer using a hybrid jet-impingement/micro-channel cooling scheme. *International journal of heat and mass transfer*, 49(3), 682-694.
- Thome, J. R. (2004). Engineering data book III. *Wolverine Tube Inc, 2010*.
- Thome, J. R., Dupont, V., & Jacobi, A. M. (2004). Heat transfer model for evaporation in microchannels. Part I: presentation of the model. *International Journal of Heat and Mass Transfer*, 47(14-16), 3375-3385.
- Tibirićá, C. B., & Ribatski, G. (2014). Flow patterns and bubble departure fundamental characteristics during flow boiling in microscale channels. *Experimental Thermal and Fluid Science*, 59, 152-165.
- Tibirićá, C. B., & Ribatski, G. (2015). Flow boiling phenomenological differences between micro-and macroscale channels. *Heat Transfer Engineering*, 36(11), 937-942.
- Tibirićá, C. B., Czelusniak, L. E., & Ribatski, G. (2015). Critical heat flux in a 0.38 mm microchannel and actions for suppression of flow boiling instabilities. *Experimental Thermal and Fluid Science*, 67, 48-56.
- Tien, N. X., & Shin, S. (2016). A Novel Concentrator Photovoltaic (CPV) System with the Improvement of Irradiance Uniformity and the Capturing of Diffuse Solar Radiation. *Applied Sciences*, 6(9), 251.
- Tran, T. N., Wambsganss, M. W., & France, D. M. (1996). Small circular-and rectangular-channel boiling with two refrigerants. *International Journal of Multiphase Flow*, 22(3), 485-498.
- Triplett, K. A., Ghiaasiaan, S. M., Abdel-Khalik, S. I., & Sadowski, D. L. (1999). Gas-liquid two-phase flow in microchannels Part I: two-phase flow patterns. *International Journal of Multiphase Flow*, 25(3), 377-394.
- Tuckerman, D. B., & Pease, R. F. W. (1981). High-performance heat sinking for VLSI. *IEEE Electron device letters*, 2(5), 126-129.
- Wu, P., & Little, W. A. (1984). Measurement of the heat transfer characteristics of gas flow in fine channel heat exchangers used for microminiature refrigerators. *Cryogenics*, 24(8), 415-420.
- Xu, Y., & Fang, X. (2012). A new correlation of two-phase frictional pressure drop for evaporating flow in pipes. *international journal of refrigeration*, 35(7), 2039-2050.
- Yu, D. (1995). An experimental and theoretical investigation of fluid flow and heat transfer in microtubes. In *ASME/JSME Thermal Engineering Conference* (Vol. 1).
- Zhang, H. Y., Pinjala, D., Wong, T. N., Toh, K. C., & Joshi, Y. K. (2005). Single-phase liquid cooled microchannel heat sink for electronic packages. *Applied Thermal Engineering*, 25(10), 1472-1487.

Zivi, S. M. (1964). Estimation of steady-state steam void-fraction by means of the principle of minimum entropy production. *Journal of heat transfer*, 86(2), 247-251.

Zuber, N., & Findlay, J. (1965). Average volumetric concentration in two-phase flow systems. *Journal of heat transfer*, 87(4), 453-468.

APPENDIX A: MEASUREMENT UNCERTAINTIES AND ERROR PROPAGATION

The errors associated to calculated parameters were evaluated based on the propagation of error according to the procedure suggested by Moffat (1988). Partial derivatives were used to calculate the sensitivity coefficient of a result R with respect to the measurement X . When the result R depends on several measurements X_i , i.e. $R = f(X_1, X_2, \dots, X_n)$, the uncertainty of δR is given as:

$$\delta R = \left\{ \sum_{i=1}^n \left(\frac{\partial R}{\partial X_i} \delta X_i \right)^2 \right\}^{\frac{1}{2}} \quad (\text{A.1})$$

The errors associated to mass velocity, heat flux, vapor quality and heat transfer coefficient measurements were derived through the procedure suggested by Moffat (1988). The error associated to the fluid saturation temperature was already determined in Section 5.5 as $\pm 0.22^\circ\text{C}$, based on the comparison of the experimental and estimated results for the pressure drop. The uncertainty related to the mass velocity (Eq. 5.2) was given by:

$$\delta G = \sqrt{\left(\frac{\partial G}{\partial \dot{m}} \delta \dot{m} \right)^2 + \left(\frac{\partial G}{\partial D_{int}} \delta D_{int} \right)^2} = \sqrt{\left(\frac{4}{\pi D_{int}^2} \delta \dot{m} \right)^2 + \left(\frac{-8\dot{m}}{\pi D_{int}^3} \delta D_{int} \right)^2} \quad (\text{A.2})$$

The results for the two tested mass velocities and tube diameters are summarized in Table A.1. From this table, it is seen that the error related to the experimental mass velocity varies from 3 to 8%, approximately. The greatest errors are encountered for the smallest diameter. Because the tube diameter uncertainty is 20 μm , the relative error of the diameter is greater for the smallest tube, which reflects in greater mass velocity errors, as verified in Table A.1.

Table A.1 – Experimental mass velocity uncertainties

Mass Velocity [kg/m ² s]	$D = 0.5 \text{ mm}$	$D = 1.1 \text{ mm}$
400	8.50%	3.75%
600	8.33%	3.67%

The local heat flux is given by $\frac{VI(1-\sigma)}{\pi D_{int}L}$ and its uncertainty was calculated as follows:

$$\delta q'' = \sqrt{\left(\frac{\partial q''}{\partial V} \delta V\right)^2 + \left(\frac{\partial q''}{\partial I} \delta I\right)^2 + \left(\frac{\partial q''}{\partial \sigma} \delta \sigma\right)^2 + \left(\frac{\partial q''}{\partial D_{int}} \delta D_{int}\right)^2 + \left(\frac{\partial q''}{\partial L} \delta L\right)^2} \quad (A.3)$$

After calculating the partial derivatives, the final expression for estimating the local heat flux uncertainty becomes:

$$\delta q'' = \sqrt{\left(\frac{I(1-\sigma)}{\pi D_{int}L} \delta V\right)^2 + \left(\frac{V(1-\sigma)}{\pi D_{int}L} \delta I\right)^2 + \left(\frac{-VI}{\pi D_{int}L} \delta \sigma\right)^2 + \left(\frac{-VI(1-\sigma)}{\pi D_{int}^2 L} \delta D_{int}\right)^2 + \left(\frac{-VI(1-\sigma)}{\pi D_{int}L^2} \delta L\right)^2} \quad (A.4)$$

The error associated to the heat flux was calculated for the hotspot region assuming fixed heat losses of 20% ($\sigma = 0.2$) with an absolute uncertainty of $\pm 3\%$ (see Section 5.2.2). The ratio of the voltage difference V and the electrical current I (or the tube resistivity at hotspot region) was taken from the experimental data for each tube diameter. Table A.2 summarizes the uncertainties according to the level of heat flux and tube diameter. From this table it is seen that the greatest errors occur for the smallest tube diameter. Also, the error reduces as the heat flux is increased. According to the Table A.2, the error associated to the heat flux is within the range of 3 to 6%.

Table A.2 – Experimental uncertainties for the local heat flux

q [kW/m ²]	$D = 0.5$ mm	$D = 1.1$ mm
20	6.47%	4.82%
40	5.40%	3.68%
80	4.78%	2.95%
120	4.56%	2.66%
160	4.44%	2.52%

The heat transfer coefficient was calculated directly through Newton's Law of Cooling (Eq. 5.19), thus its uncertainty was given by:

$$\delta\alpha_{2\phi} = \sqrt{\left(\frac{\partial\alpha_{2\phi}}{\partial q''}\delta q''\right)^2 + \left(\frac{\partial\alpha_{2\phi}}{\partial T_w}\delta T_w\right)^2 + \left(\frac{\partial\alpha_{2\phi}}{\partial T_f}\delta T_f\right)^2} \quad (\text{A.5})$$

Taking the partial derivatives, Eq. A.5 becomes:

$$\delta\alpha_{2\phi} = \sqrt{\left(\frac{\delta q''}{T_w - T_f}\right)^2 + \left(\frac{-q''}{(T_w - T_f)^2}\delta T_w\right)^2 + \left(\frac{q''}{(T_w - T_f)^2}\delta T_f\right)^2} \quad (\text{A.6})$$

The errors associated to the heat transfer coefficient measurements were estimated considering a heat flux uncertainty of $\pm 6\%$, fluid temperature uncertainty of $\pm 0.22^\circ\text{C}$ and wall temperature uncertainty of $\pm 0.14^\circ\text{C}$. In these calculations, the values for the heat flux, wall temperature and fluid temperature were taken from the experimental database presented in the Results section for the flow boiling transient heating tests and contemplates the range of the experimental average heat transfer coefficients evaluated in the present study. Table A.3 summarizes the results for the calculated uncertainties. From this table, it is seen that the error associated to the heat transfer coefficient can be assumed as almost constant and equal to 7%. The low variance of the uncertainty for different conditions is a consequence of the high dependence of the heat transfer coefficient uncertainty upon the heat flux error, as the uncertainty calculations indicated. It is worth to note that the uncertainties were calculated for average heat flux of 80 and 120 $\text{kW/m}^2\text{K}$. Larger errors are expected to occur under lower heat fluxes. For a heat flux of 40 $\text{kW/m}^2\text{K}$, the error was estimated as 10%. Based on the heat transfer coefficient analysis, the error of the heat transfer coefficient measurements was assumed as between 7 and 10%.

Table A.3 – Experimental uncertainties for the local heat transfer coefficient

$D = 0.5 \text{ mm}$		$D = 1.1 \text{ mm}$	
HTC [$\text{kW/m}^2\text{K}$]	Uncertainty	HTC [$\text{kW/m}^2\text{K}$]	Uncertainty
13	7.29%	10	6.99%
17	7.09%	15	6.79%
21	7.02%	17	6.44%

According to the data reduction procedure (see Section 2.5), the vapor quality is estimated based on the local pressure and enthalpy, which were evaluated through an upward finite difference scheme for solving the equations of energy and momentum conservation. The method of Moffat (1988) requires an explicit expression for determining the experimental errors, but the data reduction procedure of this work does not contemplate an analytical expression for estimating the vapor quality. To work-around this problem, an explicit expression for estimating the vapor quality at the tube exit was derived based on the conservation of energy of a control volume covering the pre-heater and the test section. The equation for the vapor quality at the tube outlet is given as follows:

$$x = \frac{\dot{P}_{DC\ sources} - \dot{m}c_p\Delta T_{sub}}{\dot{m} h_{lv}} \quad (A.7)$$

where $\dot{P}_{DC\ sources}$ is the power output of DC sources, ΔT_{sub} is the subcooling temperature of the fluid entering the tube, c_p is the fluid heat capacity at constant pressure and h_{lv} is the enthalpy of vaporization.

The uncertainty associated to $\dot{P}_{DC\ sources}$ was taken as ± 0.0244 W. This value was calculated based on the uncertainty of electrical and current measurements of the three DC sources. For ΔT_{sub} , the error was evaluated as the sum of the contributions of the fluid temperature and the fluid saturation pressure uncertainties. The fluid temperature uncertainty is assumed as the thermocouples measurement error of $\pm 0.14^\circ\text{C}$. The fluid saturation temperature uncertainty is calculated from the absolute pressure transducer error and the Clausius-Clapeyron equation. The absolute pressure transducer error of 4.5 kPa translates into temperature variations of $\pm 0.2^\circ\text{C}$ for R134a at 31°C saturation temperature. Therefore, the error associated to ΔT_{sub} was calculated as $\sqrt{0.14^2 + 0.2^2}$ or $\pm 0.24^\circ\text{C}$. Regarding the mass flow rate, the error was assumed as equal to the accuracy of the Coriollis mass flow meter. The final expression for calculating the error associated to vapor quality estimative is given by:

$$\delta x = \sqrt{\left(\frac{1}{\dot{m} h_{lv}} \delta \dot{P}_{DC\ sources}\right)^2 + \left(\frac{-c_p}{h_{lv}} \delta \Delta T_{sub}\right)^2 + \left(\frac{-\dot{P}_{DC\ sources}}{h_{lv} \dot{m}^2} \delta \dot{m}\right)^2} \quad (A.8)$$

Table A.4 summarizes the vapor quality uncertainties under three different conditions for the two tube diameters. From this table, it is seen that the uncertainty of the vapor quality

decreases as the vapor quality increases. Also, the uncertainty is greater for the smaller diameter tube. Based on the results, an average error of $\pm 4\%$ was adopted for the vapor quality.

Table A.4 – Experimental uncertainties for the vapor quality

x_{exit}	$D = 1.1 \text{ mm}$	$D = 0.5 \text{ mm}$
20%	5.08%	7.31%
50%	3.84%	6.09%
70%	1.73%	3.10%

